

Effect of Hydraulic Shear Stress on the Banks of the Red River

By

Masoud Goharrokhi

A thesis submitted to the Faculty of Graduate Studies of

The University of Manitoba

in partial fulfillment of the requirements for the degree of

Master of Science

Department of Civil Engineering

University of Manitoba

Winnipeg, Manitoba, Canada

Copyright © 2015 by Masoud Goharrokhi

Abstract

This study focuses on flow-induced bank erosion on the Red River. The study includes field measurements, experimental testing, and numerical simulation. Soil samples from the riverbank were collected at seven sites and their erodibility parameters were estimated through laboratory testing. The hydraulic shear stresses applied to the river reach were obtained by developing a 2D numerical model. Erosion rates for these sites were modeled using a linear excess shear stress equation.

A bank monitoring and total suspended sediment investigation were also conducted to assess the erosion and deposition rates and patterns. The locations susceptible to erosion were determined and the periods during which these processes are likely to occur were estimated.

The numerical modeling and soil testing results show that most of the time, the magnitude of flow shear stresses exerted on the bank are less than the soil sample critical shear stresses. Therefore, without considering other bank widening mechanisms as well as their interactions, the fluvial bank erosion (in isolation) should not be a significant process. However, bank monitoring shows significant bank erosion.

It is recommended that the effect of subaerial processes (especially freeze-thaw) be investigated further to determine their effects on flow-induced erosion. The monitoring

results convincingly show that climate-related phenomena influences cohesive soil structures and consequently, a soil's cohesive resistance forces are significantly reduced. Therefore it can be concluded that subaerial mechanisms play a significant role in widening the banks of the Red River.

Acknowledgements

I am very thankful for all of the support and assistance of my advisor, Dr. Shawn Clark, whose his guidance, expertise and direction were essential to the completion of this project.

I would also like to thanks several friends and colleagues at the University of Manitoba, which I would not have been able to complete this thesis without their help.

I would also like to thank Manitoba Hydro, the Natural Sciences and Engineering Research Council of Canada, for the funding opportunities. The research undertaken in this thesis would have not been possible without their support.

Lastly, I would like to thank my family, and in particular my wife for encouraging and supporting me throughout my program.

Table of Contents

Abstract.....	i
Acknowledgements.....	iii
Table of Contents.....	iv
List of Tables	vi
List of Figures	vii
CHAPTER 1 <i>Introduction</i>	1
1.1 Introduction.....	1
1.2 Overview of the Study Area	4
1.3 Goals and Objectives.....	6
CHAPTER 2 <i>Literature Review</i>	7
2.1 Cohesive Soil Characteristics.....	7
2.2 Riverbank Recession Processes.....	9
2.3 Fluvial Cohesive Riverbank Erosion Modeling	11
2.4 Critical Shear Stress Estimation from Soil Properties	12
2.5 Erodibility Parameters Measurement Techniques	16
2.6 Near Bank Shear Stress Estimation	17
CHAPTER 3 <i>Methodology</i>	21
3.1 Introduction.....	21
3.2 Field Activities	21
3.2.1 Water Level Measurement	22
3.2.2 Bathymetric Survey.....	23
3.2.3 Redoing Bathymetry	27
3.2.4 Flow Discharge and Velocity Measurements.....	29
3.2.5 Water Sampling Program.....	34
3.2.6 Soil Sampling Program	39
3.3 Laboratory Testing	43
3.3.1 TSS Testing	43
3.3.2 Water-Sediment Size Testing.....	43
3.3.3 Erosion Measurement Device (EMD) Testing.....	45

3.3.4	Geotechnical Laboratory Testing	50
3.4	Numerical Modeling	52
3.4.1	Mesh Generation	53
3.4.2	MIKE 21 Flow Model FM Setup	54
CHAPTER 4	<i>Data Processing and Results</i>	60
4.1	Introduction	60
4.2	Water Level Data Processing	61
4.3	Discharge Data Processing and Stage Curve Development	64
4.4	Velocity Distribution Analysis	67
4.5	Calculation of Manning's n	74
4.6	Averaged Applied Shear Stress	79
4.7	Local Shear Stress and Bed Roughness Estimation	81
4.8	Modeling Hydraulic Shear Stress Using Real Hydrometric Data	85
4.9	Numerical Modeling Results	90
4.10	EMD Results	99
4.11	Soil Part Results	105
4.12	Studying Red River Erosion and Deposition Mechanisms Using the Characterization of Particles in Suspension	108
4.12.1	TSS Distribution in the Red River	109
4.12.2	Grain Size Distribution (GSD)	115
4.13	River Geomorphic Change over Time	123
CHAPTER 5	<i>Conclusions</i>	128
5.1	Conclusions	128
References	131

List of Tables

Table 2.1: Different factors may affect cohesive soil erosion	8
Table 2.2: Equations for bank applied shear stress for wide channel and on trapezoid cross section.....	19
Table 3.1: Water-sediment sampling locations at SPB.....	36
Table 3.2: Soil and sediment sampling location	42
Table 4.1: Summary of discharge measurement and other flow properties of the Red during study period.....	65
Table 4.2: Supplemental discharge from Water Survey of Canada.....	66
Table 4.3: Average and maximum velocity under different discharge values during study period.....	68
Table 4.4: Summary of flow properties in the Red at different locations on July 23 rd , 2013	73
Table 4.5: Specific energy and Manning's n values at the SPB over time	76
Table 4.6: Specific energy and Manning's n values at different time and locations	78
Table 4.7: Specific energy and Manning's n values on July 23 rd , 2013 at different locations.....	78
Table 4.8: Local boundary shear stress and roughness height values over time	84
Table 4.9: Shear stress distribution values using measured velocity and depth of the Red River	88
Table 4.10: Shear stress distribution values on the SPB site using ADCP measurement data	89
Table 4.11: Comparison between measured and modeled water surface elevation at the SPB	91
Table 4.12: Comparisons between measured and modeled water level at SPB for validation	91
Table 4.13: Comparisons between measured and simulated Red River mean velocity ..	96
Table 4.14: Applied shear stress magnitude for each elevation of the Red under bank-full condition	97
Table 4.15: EMD test results for all sites	102
Table 4.16: Duration of discharge and average applied shear stress on the Red River bank.....	103
Table 4.17: Results of cumulative erosion rate for MN3 and MN4 locations	104
Table 4.18: Soil properties of the Red River bank	107
Table 4.19: Primary mode of sediment transport on the basis of Rouse number	120
Table 4.20: Maximum particle size potential in bed and suspended transport mode ..	122

List of Figures

Figure 1.1: Plan view of the study reach.....	5
Figure 3.1: SPB water level recording station.....	23
Figure 3.2: Photograph of the M9 device and hydroboard as close as possible to the bank.....	24
Figure 3.3: Bathymetric survey from June 18 th , 2013.....	26
Figure 3.4: Elevation of four cross sections	26
Figure 3.5: Redoing bathymetric points after high flow in 2013.....	28
Figure 3.6: Number of discharge measurements over time, weekly basis	30
Figure 3.7: Discharge and velocity measurement from top of the SPB	31
Figure 3.8: Plan view of 12 discharge and velocity measurements on July 23 rd , 2013.	33
Figure 3.9: Water sampling equipment.....	36
Figure 3.10: Water sampling locations at SPB (a) and FGB (b) looking downstream.....	37
Figure 3.11: Water sampling locations along 20 km of the Red River.....	39
Figure 3.12: Soil sampling procedure using Shelby Tube	41
Figure 3.13: Soil sample location site plan	42
Figure 3.14: Mastersizer 2000 device and computer system in the Smart Park.....	45
Figure 3.15: Erosion Measurement Device (EMD)	46
Figure 3.16: The electric jack device to put sample into the testing tube	47
Figure 3.17: Soil sample preparation for EMD test	48
Figure 3.18: Soil sample for geotechnical tests	50
Figure 3.19: Hydrometry test to determine the fines particle size distribution	52
Figure 3.20: Reach banks location site plan (a) and triangular mesh element along the reach (b).....	56
Figure 3.21: The complete river topography after interpolation	57
Figure 4.1: Daily water elevation for the Red River at the FGB Station (data from City of Winnipeg, 2012-2013)	61
Figure 4.2: Red River near the University of Manitoba on a) April 29 th (WSE = 228.7 m), b) October 12 th (WSE = 223.5), 2013	63
Figure 4.3: Water level histogram for the SPB during study period.....	63
Figure 4.4: Maximum, minimum, and mean water level at SPB looking downstream during study period.....	64
Figure 4.5: The Red River at SPB on November 12th when border ice formed on both sides of the river	66
Figure 4.6: Discharge rating curve for the Red River at SPB during study period	67
Figure 4.7: Two measured and entropy-based calculated velocity distribution profiles.	69
Figure 4.8: Plan view of 12 discharge measurement locations on July 23 rd , 2013.....	70

Figure 4.9: Velocity distributions of 12 cross sections along the study reach	71
Figure 4.10: Location of discharge measurements during the bathymetry measurements	77
Figure 4.11: Average shear stress at SPB and other locations and dates.....	80
Figure 4.12: Spatial averaging of long term velocity measurement at different times and spanwise locations	82
Figure 4.13: SPB Site- Location C- May 8 th , 2013- channel bottom log-law fit.....	83
Figure 4.14: Comparing modeled average shear stress and average shear stress using log law method at SPB	85
Figure 4.15: Subarea hydraulic shear stress distribution close to SPB using real measured data and a dense mesh	87
Figure 4.16: Cross sectional distribution of applied shear stress at SPB using three different methods.....	90
Figure 4.17: Measured and simulated velocity profiles on July 23 rd , 2013, a) RR1, b) RR2	93
Figure 4.18: Modeled applied shear stress distribution along the study reach at maximum flow	98
Figure 4.19: EMD test results for sample MN3.....	100
Figure 4.20: EMD test results for sample MN4.....	100
Figure 4.21: EMD test results for sample MN5.....	101
Figure 4.22: EMD test results for sample MN6.....	101
Figure 4.23: EMD test results for sample MN7.....	102
Figure 4.24: Grain size analysis of MN1	105
Figure 4.25: Grain size analysis of MN3	106
Figure 4.26: Grain size analysis of MN7	106
Figure 4.27: Number of different activities related to water-sediment study over time, monthly basis	109
Figure 4.28: Water sampling locations at (a) SPB and (b) FGB.....	110
Figure 4.29: Lateral total suspended sediment distribution at SPB	111
Figure 4.30: Total suspended sediment flux rating curve	113
Figure 4.31: Longitudinal variation of TSS versus distance ratio along 20 km of the Red	115
Figure 4.32: d_{10} , d_{50} , and d_{90} grain sizes for SPB water samples	116
Figure 4.33: Comparing d_{10} , d_{50} , and d_{90} grain sizes at SPB Vs. FGB.....	117
Figure 4.34: d_{10} , d_{50} , and d_{90} grain sizes for 20 km of water samples	118
Figure 4.35: Relationship between GSD and discharge measurements.....	118
Figure 4.36: Comparing GSD of water sample and freshly deposited sediments	119

Figure 4.37: Specific particle size class concentration distribution on the basis of its Rouse number value 120

Figure 4.38: Measured cumulative erosion and deposition rate between 2013 and 2014 as well as maximum simulated applied shear stress ($Q= 1200 \text{ m}^3/\text{s}$) for different elevations of the Red 127

1.1 Introduction

Erosion in general, is an important subject for many science and engineering fields and applications. Erosion has been recognized as an important process affecting water resources by producing sediment in rivers. The influence of erosion on water quality, contaminants transport, and aquatic systems has been documented (Rinaldi and Darby, 2008). Sediments act as vehicles that transport pollutants (like heavy metals and bacteria) and therefore may have significant health risks (Clark, 1985; USEPA, 2002). The financial cost associated with the physical, chemical and biological damage caused by soil erosion is reasonable motivation to devote much research to better understand and prevent this phenomenon.

Many studies indicate that channel erosion within river systems is a major source of sediment. In addition, the literature suggests that the major in-stream source of sediment is bank widening (Rinaldi and Darby, 2008). Hence, understanding the rates, locations, and patterns of bank recession is a pre-requisite for knowing river sediment transport processes as well as bank protection strategies. Some studies have shown that bank widening can contribute as much as 85% of the total sediment load (Walling and

Amos, 1999; Simon et al., 2000). There have also been studies which report bank recession rates between 1.5 to 1100 m per year (Trimble, 1997; Wallbrink et al., 1998; Prosser et al., 2000; Simon et al., 2000). Besides the direct role of bank recession in sediment production as well as economic-environmental impact, stream bank widening affects private property, valuable natural assets, bridges, and other stream-side structures (Lawler et al., 1997; ASCE, 1998; Winnipeg Free Press, 2005)

Riverbank widening can be induced, concurrently or sequentially, through three different processes: subaerial weakening (climate-related phenomena), fluvial erosion (caused by applied flow shear stress), and bank failure (due to slope instability) (Thorn, 1982; Lawler, 1995). This study mainly focuses on fluvial erosion which occurs when the applied shear stress (τ_a) of the river is greater than the soil critical shear stress (τ_c) at that location (Hanson, 1989; Hanson and Simon, 2001). Erosion is considered negligible when the local applied shear stress is less than the soil resistance.

Riverbank materials have been grouped into cohesive and non-cohesive soils; or may consist of a mixture of these two soil types. Cohesive soils consist primarily of clay which exhibit inter-particle resistance forces (Huang et al., 2006) that are not due to the gravitational force, and are influenced by climate, flow and soil conditions. Non-cohesive erosion and sediment transport theory and equations are therefore not applicable to cohesive materials. Cohesive bank erosion rates are most commonly approximated using the excess shear stress equation (Partheniades, 1965). This simple

equation has been widely accepted and includes three main components to estimate the erosion rate of cohesive riverbanks. Two of these components are soil dependent: soil erodibility (k_d) and soil critical shear stress, while the third component of this equation is the applied flow shear stress (τ_a).

The critical shear stress of a soil is defined as the magnitude of applied shear stress required to cause incipient motion. In order to accurately use many erosion and sediment transport models, including HEC-RAS and MIKE 21, quantification of soil dependent parameters is needed; although due to the complex structure and behavior of cohesive soils, these parameters are difficult to quantify (Grissinger, 1982). Considerable research has been attempted to develop empirical equations for estimating these parameters, yet they are not reliable for global application (Knapen et al., 2007; Kimiaghali et al., 2015a).

Many methods have been developed to measure cohesive soil parameters, including flume tests, submerged jet tests, and rotating cylinder tests. Flume flow tests with a soil sample located in the bed is a relatively simple, easy to use, and inexpensive laboratory method which has long been used for measuring k_d and τ_c . One example of this kind of instrument is called the Erosion Measurement Device (EMD), which was constructed by the geotechnical group of the University of Manitoba for studying erosion of cohesive soils. The device includes an acrylic rectangular conduit, a reservoir, and a pump. Recirculated closed-channel flow is used to calculate the rate of erosion due to different

applied shear stresses to the soil surface which is pushed through a hole in the bottom of the conduit.

Applied shear stress in a natural channel is influenced by geometric characteristics (depth and roughness) and flow properties (water velocity) and is a challenging variable to quantify. To quantify shear stress, numerical modeling has been widely accepted in the hydraulic engineering field. In order to estimate applied shear stress under different flow conditions, a calibrated hydrodynamic model is required and to properly develop a calibrated and validated hydrodynamic model, reliable field measurements are needed (Khodashenas et al. 2008). Hydrodynamic characteristics and the hydraulic shear stress of a river are strongly related.

1.2 Overview of the Study Area

The study was performed along approximately 10 km of the Red River extending between the South Perimeter Bridge (SPB) (634237 E - 5516381 N) and the Fort Garry Bridge (FGB) (633544 E - 5520423 N) near the University of Manitoba (Figure 1.1). The banks of the Red River are comprised of cohesive soils and vegetation. The Red River flows north from Minnesota in the United State and then meanders through North Dakota and enters Canada at Emerson, Manitoba. After flowing about 140 km, it reaches Winnipeg and becomes one of the two main rivers that flow through the city, and helps to comprise the nearly 200 km of shore line within Winnipeg. It then flows

further north before draining into Lake Winnipeg. The Red River is 885 km long, with approximately 630 km located in the United States and 255 km located in Canada.

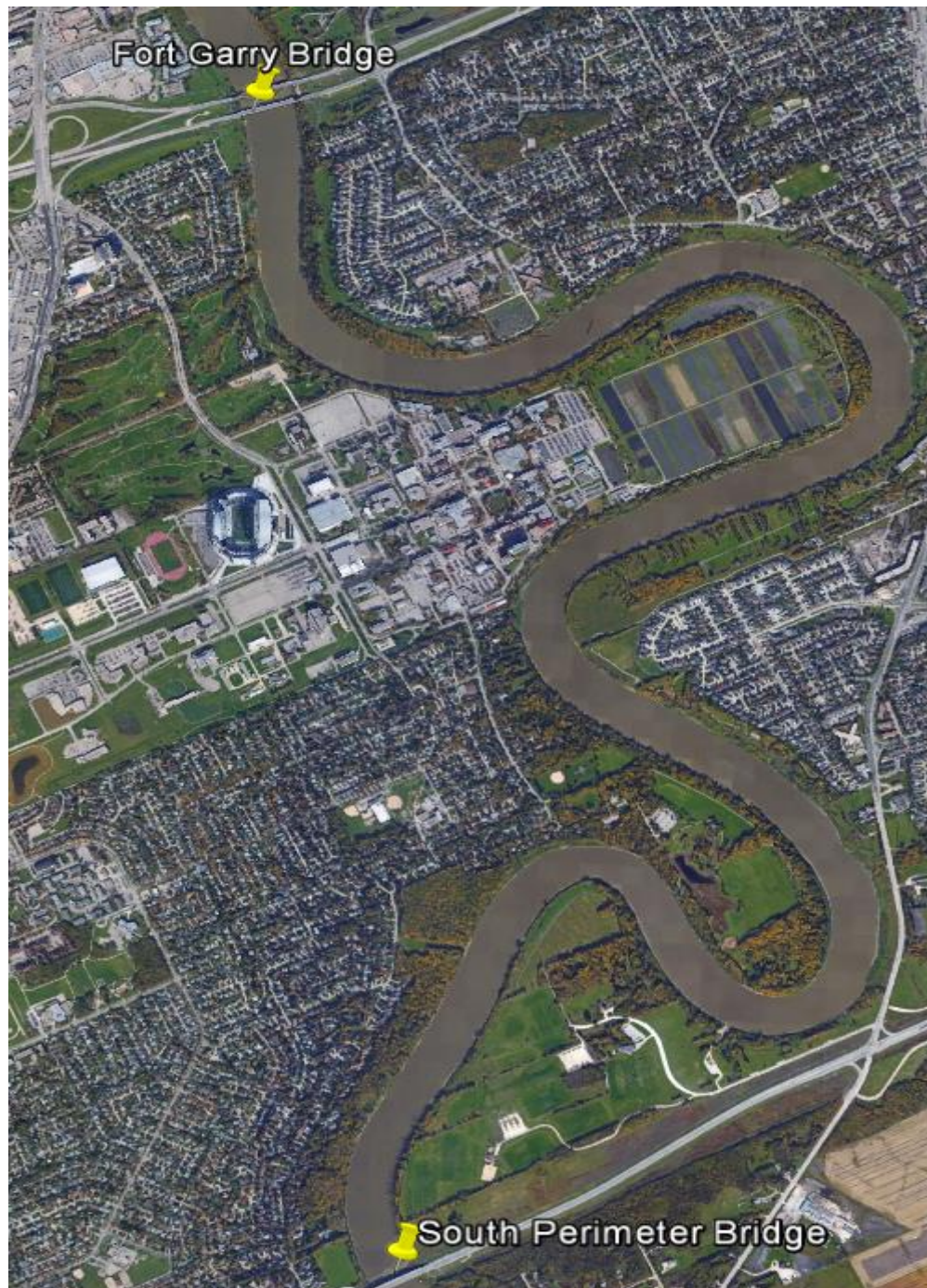


Figure 1.1: Plan view of the study reach

1.3 Goals and Objectives

The overall goal of this study was to develop a further understanding of bank erosion on the Red River caused by the applied shear stress resulting from the flow of water. Because of the broad scope of this topic, the research was focused on two specific objectives to meet the overall research goal:

- 1- Modeling the effect of applied shear stress on the local Red River soil bank
- 2- Monitoring rates and locations of bank erosion.

The research hypothesis that applied shear stress plays a significant role in riverbank erosion on the Red River, especially during the relatively frequent flooding events experienced in Manitoba. Later on, through the quantification of applied shear stress and critical shear stress, the study assumption was that weathering and freeze-thaw have a dominant impact on Red River bank erosion.

2.1 Cohesive Soil Characteristics

Soils have been mainly grouped into two categories based on their grain sizes: coarse-grained (non-cohesive) and fine-grained (cohesive) soils. Cohesive soils, primarily consist of clay (<2 μm), silt (2-75 μm), fine sand (75-200 μm) particles, organic materials, and water with more than 50 percent of the particles being able to pass through the No. 200 (0.075 mm) sieve with adequate amount of clay (10-20%) (Sturm, 2001). This type of soil behaves differently than non-cohesive soil, and their behaviour can therefore not be modelled using equations developed for non-cohesive soils.

The clay fraction is mainly responsible for a cohesive soil's resistance to erosion by creating inter-particle forces (Knighton, 1998). These forces bind soil particles together, give them additional erosion resistance compared to non-cohesive soils. The small size, flat shape, and high specific surface combined with the electrical charge distribution of clay make the cohesive soil behave more complexly than coarse-grained soils under varying spatial and temporal conditions (Debnath et al., 2007). In addition, these forces are influenced by climatic characteristics, fluid properties, soil conditions, and other factors. Table 2.1 presents different factors which may have a considerable influence on

the inter-particle forces in cohesive soil. (Smerdon and Beasley, 1961; Ariathuria and Arulanandan, 1978; Knighton, 1998; Lick and McNeill, 2001; Wynn and Mostaghimi, 2006; Knapen et al., 2007; Wynn et al., 2008; Kimiaghalam et al., 2015a).

Table 2.1: Different factors may affect cohesive soil erosion

Main Categories	Factors				
Physical Factors (Both soil and flow)	Aggregate size distribution	Specific gravity	Sand, silt, and clay content	Soil dispersion ratio	Atterberg limits
	Soil type	Soil structure	Plasticity index	Water content	Soil porosity
	Applied shear stress and its duration	Pore-water osmotic potential	Total suspended solid	Water viscosity and density	Complex secondary flows
	Soil stability	Water temperature	Fissures and cracks	Soil temperature	Grain size distribution
Chemical Factors (Soil, eroding fluid, and pore fluid chemistry)	Soil and water mineralogy	Soil gas content	Clay attraction capacity	Soil cation exchange capacity	Soil and water PH
	Soil dielectric dispersion and electrochemical forces	Soil and water organic content	Soil and water irons type and concentration	Soil and water electrical conductivity	Ion concentration in water
	Soil sodium adsorption ratio	Water salinity	Water redox potential	Water chlorinity	Water chemical composition
	Soil and water oxygen content	Ion type in water			
Mechanical and In-situ Factors	Soil bulk density	Soil shear strength	Soil cohesion	Soil friction angle	Soil consolidation
	Settling velocity	Critical shear stress	Soil saturation condition	River ice forces	Pore-water pressure
	Stress history of the soil	Bank material composition	Bank slope	Bank height	
Biological Factors	Vegetation (type and density)	Worms	Crabs	Animal burrows	Animal trampling
	Fish				
Environmental Factors	Freeze and thaw cycling	Wet-dry cycling	Water table changes	Air temperature	

2.2 Riverbank Recession Processes

Generally a combination of three processes causes riverbank recession over time: subaerial processes, fluvial erosion, and bank failure (Lawler, 1995). Subaerial processes such as wetting/drying cycles and freezing/thawing cycles influence the soil structure prior to fluvial erosion (Thorn, 1982). This phenomenon is a function of climate conditions which reduce cohesive soil resistance to future erosion (Wynn et al., 2008). Several studies have been undertaken resulting in the further understanding of this subject (Couper and Maddock, 2001; Lawler, 1993; Prosser et al., 2000). Lawler et al., (1997) grouped bank process into pre-wetting, desiccation, and freeze-thaw on the basis of soil moisture. Van Klaveren and McCool, (1998) found that freeze/thaw cycles can significantly increase bank erodibility. Lawler, (1993) found that the formation of needle ice during the winter season increased bank erosion by 32-43% on the River Liston in West Glamorgan, UK. As a summary, these preparatory processes cause riverbanks to become more susceptible to fluvial erosion or mass wasting directly or indirectly (Wolman, 1959) by increasing soil erodibility rather than causing erosional processes (Thorne, 1990; Lawler, 1993; Green et al., 1999).

Fluvial bank erosion is the removal and transport of soil from the riverbank surface by flow. As the water moves downstream, it exerts a force on the river boundary parallel to the flow direction. Once the force per unit area (shear stress) exerted on the soil exceeds the threshold value (critical shear stress), the soil starts to move and flow-induced erosion will occur (Owoputi and Stolte, 1995). Generally, resistance forces are

the particle submerged gravitational weight (in current non-cohesive theory) or the friction and inter-particle forces within the river material (in cohesive soils). In cohesive fluvial erosion, the resistance forces are controlled by many of the soil and water characteristics (Grissinger, 1982; Thorn, 1982; Knapen et al., 2007).

Fluvial erosion removes and transports soil particles from the bank surface. Also fluvial erosion influences bank failure by undercutting the lower bank or the river bed and consequently increasing the bank height or angle. When the shear strength of the upper bank is less than the gravitational forces, mass failure will occur (Osman and Thorn, 1988; Rinaldi and Darby, 2008). This phenomenon is controlled by the bank geometry, properties of bank materials, bank vegetation, and pore water pressure (Thorn, 1990; Abernethy and Rutherford, 1998). Casagli et al., (1999) reported that reduction in pore water pressure decreases bank strength, thereby mass wasting promoting.

It can be concluded that riverbank widening is a cyclical process and the dynamic interaction and feedback loops between these processes should be considered. Subaerial processes make the bank more susceptible to erosion. Flow-induced erosion causes deep and steep banks which leads to slope instability causing bank failure and subsequently mass wasting occurs. Therefore when the applied shear stress at the bank toe or bank surface is less than the bank materials critical shear stress, this cyclic phenomenon might be stopped, which may happen naturally by retreating of the river banks.

2.3 Fluvial Cohesive Riverbank Erosion Modeling

The process of cohesive soil erosion is not fully understood due to many factors that influence the behavior of this soil and sediment (Kimiaghdam et al., 2015a). There has been little research done for fluvial riverbank erosion modeling and its interaction with other cohesive bank retreat processes due to the paucity of reliable monitoring data. The estimation of river bank erosion is an important subject, and the development of a simple equation for this subject is required. The excess stress equation is frequently used in open channel flow to model flow-induced cohesive riverbank/bed erosion rates (Partheniades, 1965):

$$\varepsilon = k_d(\tau_a - \tau_c)^a \quad \text{Equation 2.1}$$

Where

ε = erosion rate (m/s);

k_d = soil erodibility coefficient;

τ_a = applied shear stress on the soil (N/m^2);

τ_c = soil critical shear stress (N/m^2); and

a = typically assumed to be 1.

On the basis of this equation, when applied stress is below the soil critical shear stress, the erosion rate is considered zero and when the applied shear stress exceeds the critical shear stress, the erosion rate is considered positive (Osman and Thorn, 1998).

The challenge here is determining the applied shear stress and the erodibility parameters (τ_c and k_d). The erodibility parameters are time- and space-dependent cohesive properties and the applied shear stress is a hydraulic property that also varies in time and space.

2.4 Critical Shear Stress Estimation from Soil Properties

Since cohesive soil characteristics differ from one location to another and are influenced by many factors, the relationships between mechanical, chemical, and biological soil properties and erosion rate are still not clear. There is no universal equation to estimate the material-dependent erodibility parameters (Roberts et al., 1998). Several studies have been undertaken in order to develop empirical equations between different soil properties and critical shear stress, but they are not accurate enough for engineering. Provided below is an overview of research done for the development of empirical relationships to estimate one of the main components of the cohesive fluvial erosion equation (τ_c).

Dunn (1959) obtained the following relationship between critical shear stress and sediment shear strength (τ_s) and plasticity index (I_w):

$$\tau_c = 0.01 (\tau_s + 180) \tan(30 + 1.73 I_w) \quad \text{Equation 2.2}$$

Smerdon and Beasley (1961) developed critical shear stress estimation equations based on soil properties including: the plasticity index, dispersion ratio, mean particle size, and clay percentage. Their equations (Eqs. 2.3 - 2.6) were obtained from a flume study on eleven cohesive sediment types in Missouri

$$\tau_c = 0.16 (I_w)^{0.84} \quad \text{Equation 2.3}$$

$$\tau_c = 10.2 (D_r)^{-0.63} \quad \text{Equation 2.4}$$

$$\tau_c = 3.54 * 10^{-28.1d_{50}} \quad \text{Equation 2.5}$$

$$\tau_c = 0.493 * 10^{0.0182P_c} \quad \text{Equation 2.6}$$

Where,

I_w = plasticity index (-);

D_r = dispersion ratio (-);

d_{50} = median particle size (mm); and,

P_c = percent clay by weight (%).

Julian and Torres (2006) suggested Equation 2.7 to estimate critical shear stress on the basis of the percentage of silt and clay as well as erodibility rate ϵ (cm/s). This equation was developed using results from Dunn (1959) study.

$$\tau_c = 0.1 + 0.1779(SC) + 0.0028 (SC)^2 - 2.34 \times 10^{-5}(SC)^3 \quad \text{Equation 2.7}$$

where SC is the silt and clay percentage.

Kimiaghalam et al. (2015a) found that the critical shear stress is highly correlated with cohesion. Their equation (Eq. 2.8) was obtained from a direct shear test.

$$\tau_c = 0.89C - 0.1 \quad \text{Equation 2.8}$$

where C is cohesion (kPa)

Much research has been conducted to find relation between soil critical shear stress and cohesive soil properties. However, there has been little research regarding the estimation of the soil erodibility coefficient on the basis of either soil properties or critical shear stress. Two empirical methods are available to approximate k_d as a function of known critical shear stress. Based on an experiment conducted by Arulanandan et al. (1980), Osman and Thorn (1988), established a method to estimate soil erodibility by using the initial soil erosion. In addition, the following empirical equation was presented by Hanson and Simon (2001) to estimate the soil erodibility coefficient on the basis of critical shear stress:

$$k_d = 0.2 * \tau_c^{-0.5} \quad \text{Equation 2.9}$$

Kimiaghalam et al. (2015a) study showed that SAR impacted the value of the soil erodibility coefficient. They suggested the following logarithmic equation to estimate k_d as a function of SAR for riverbanks in Manitoba, Canada.

$$k_d = -3.9 \ln(\text{SAR}) + 1.1 \quad \text{Equation 2.10}$$

SAR is calculated by measuring the concentrations of calcium, magnesium and sodium in the saturated paste extract using the following equations.

$$\text{SAR} = \frac{[\text{Na}^+]}{\sqrt{[\text{Ca}^{2+}] + [\text{Mg}^{2+}]}} \quad \text{Equation 2.11}$$

They express the relationship between SAR, C, and ε as following:

$$\varepsilon = [-3.9 \ln(\text{SAR}) + 1.1](\tau_a - 0.89C + 0.1) \quad \text{Equation 2.12}$$

The studies that have been undertaken to date have helped define the prominent cohesive soil variables with respect to cohesive critical shear stress. However, critical shear stress and soil variable relationships that resulted from these studies are largely empirical and thus only applicable to a particular river or reach. Therefore transferability of each empirical equation between rivers is questionable.

2.5 Erodibility Parameters Measurement Techniques

As previously mentioned, non-cohesive erosion equations are inapplicable to cohesive riverbanks, and cohesive riverbank properties can change with time and location. These complexities necessitate the direct quantification of cohesive soil erosion rate using field or laboratory (Hanson and Simon, 2001; Clark and Wynn, 2007). Erosion rate testing has generally been conducted using flumes (large and small; straight and circular; one through or recirculating flow mode; closed and opened; tap water or stream water sample; flat and sloped), benthic annular channels, ISIS (Instrument Shear in Situ), cohesive strength meters, submerged jets (single; multiangle; mini), rotating cylinders, annular channels, circular tanks and impellers, pipes, pin-holes, disks, and water tunnels. The main goal of using these different devices and methods is to determine τ_c and k_d for the excess shear stress equation to estimate riverbank erosion.

Laboratory flume experiments have been used for decades and erosion rate results are generally accepted. The literature indicates that in this method, undisturbed natural and remolded samples have been tested with different flume sizes (depth, width, and length), flow velocities, and sample surface areas (Smerdon, 1964; Heinzen, 1976; Arulanandan et al., 1980; Hanson, 1989, 1990; Briaud et al., 1999, 2001a, 2001b, 2004; Moody et al., 2005; Kimiaghali et al., 2015a).

The values of τ_c and k_d can be estimated using different approaches. Some researchers have relied on visual observation of the onset of erosion via the presence of cloudy

water, general movement within the soil sample, or steady erosion of the sample surface to estimate τ_c . Others have created plots of erosion rate versus applied shear stress to assist with estimating τ_c . Once several data points are plotted, a linear best-fit line has been inserted to accurately determine the value of τ_c . Visual inspection of a soil's critical shear stress is subjective method and hard to translate between operators, while the graphical technique is more objective and easy to follow for anybody.

Of all of these methods, the most relevant to the apparatus used in the current study was designed by Briaud (Briaud et al., 1999, 2001a, 2001b, 2004). An analytical method has been established to estimate applied shear stress in the flume and to quantify soil erodibility which is explained in Chapter 3.

2.6 Near Bank Shear Stress Estimation

One of the main physical parameters controlling the amount of fluvial erosion is the applied shear stress (Partheniades, 1965). Applied shear stress, itself, is influenced by the river geometry including: the shape, height, and width of the roughness, as well as their spatial and temporal distribution on the wetted perimeter of the channel. Flow properties such as average velocity, turbulence level and secondary flows also have an effect on the applied shear stress (Chang, 1988). To estimate applied shear stress, two main approaches have been documented in the hydraulic field: Momentum-based and turbulence-based methods (Khodashenas et al., 2008).

Momentum-based methods to estimate the applied shear stress usually use the channel cross section shape and water slope or longitudinal river bed slope. These methods are generally simplified methods. The following equation presents the average boundary shear stress over the wetted perimeter (Chow, 1959).

$$\tau_{avg} = \gamma * R * S \quad \text{Equation 2.13}$$

Where, τ_{avg} is the reach-averaged shear stress (Pa), S (-) is the water surface slope, γ is the specific weight of water (N/m^2), and R is cross sectional hydraulic radius (m). In this equation the specific weight of water was taken to be $\gamma = 9806 \text{ N/m}^2$.

The shear stress applied by the flowing water on the bank or bed is not necessarily equal to the averaged boundary shear stress over the wetted perimeter. There have been previous studies in this field that show shear stresses are maximum along the bed and minimum at the top of the bank (Chow, 1959). Therefore, the mean boundary shear stress must be transform into a more realistic value to estimate the side shear stress and its distribution over a cross section. Shear stress distribution on the basis of momentum principle is presented in Equation 2.14 (Gordon et al., 2004; Khodashenas, 2008).

$$\tau_a = \gamma * S * H \quad \text{Equation 2.14}$$

where, H is local water depth (m)

Also the shear stress distribution exerted on the riverbank face is not uniform due to riverbank slope. Therefore, valuable studies have been undertaken to update the average shear stress equation for the near bank boundary shear stress for specific cross section shapes such as a trapezoid channel with gentle bank slope (1:1.5) (Lane, 1955; Chow, 1959; Osman and Thorne, 1988). Equations to estimate the average bank shear stress as well as maximum shear stress on bank/bed are summarized in Table 2.2 where B is the bottom width (m) and H* is the channel depth (m).

Table 2.2: Equations for bank applied shear stress for wide channel and on trapezoid cross section

Researcher	Update Equation	Description
Chow (1959)	$\tau_{\text{bank}} = 0.750 * \tau_{\text{avg}}$	In a wide open channel
Lane (1955)	$\tau_{\text{max on bank}} = 0.735 * \gamma * S$	B=2H*
	$\tau_{\text{max on bank}} = 0.75 * \gamma * S$	B=4H*
	$\tau_{\text{max on bank}} = 0.76 * \gamma * S$	B=8H*
	$\tau_{\text{max on bed}} = 0.89 * \gamma * S$	B=2H*
	$\tau_{\text{max on bed}} = 0.97 * \gamma * S$	B=4H*
	$\tau_{\text{max on bed}} = 0.99 * \gamma * S$	B=8H*

The key problem related to rivers is that for any morphological evaluation, the accurate and local applied shear stress is required. Therefore, another approach which is made on the basis of the turbulent flows concept has been accepted among researchers and engineers. The turbulent flow concept uses both river geometry characteristics and flow properties. The magnitude and distribution of applied shear stress can be investigated using several methods including law of the wall, Preston tube, Reynolds stresses, and Turbulent Kinetic Energy (Chow, 1959; Ludweig and Tillman, 1950; Montes, 1998; Soulsby, 1983). The law of the wall approach is widely used in practical, experimental, and numerical open channel flow studies even for vegetated beds (Baptist et al., 2007). In this study, log law method was applied for estimation of applied shear stress and is explained in Chapter 4.

3.1 Introduction

A combination of field monitoring, lab experimentation, and numerical modeling was used in this project to provide a better understanding of the effect of applied shear stress on cohesive riverbank erosion along the Red River. The following sections describe the data collection, laboratory work, and model development to achieve the main goal of this project. The field activities section includes hydrometric data collection, water-sediment sampling, and soil sampling. The laboratory experiments section includes water-sediment tests and soil tests. In the numerical modeling section, the Danish Hydraulic Institute's (DHI) MIKE 21 Flow Model HD FM and MD (Mud Transport) software package is used to develop a depth-averaged two-dimensional flexible mesh hydrodynamic model and obtain applied shear stress (DHI, 2012).

3.2 Field Activities

Quantifying the bank erosion caused by flow-induced erosion required intensive field study and reliable data. Therefore, a comprehensive field monitoring program was carried out that included measurements of water levels, detailed bathymetric surveys

with sufficient resolution, as well as flow velocity and discharge measurements. Moreover, a soil sampling and extensive water sampling program were conducted to determine soil erodibility parameters and suspended sediment concentration as well as their grain size distribution to achieve the research objectives. Field data collection was performed beginning on July 11th, 2012 and ended on September 9th, 2014.

3.2.1 Water Level Measurement

The water level changes over a year on rivers have a considerable influence on the applied shear stress and soil erodibility. This data was essential for developing a hydrodynamic model of the Red River. Two local water level recorders were installed at the upstream and downstream ends of the reach (at the bridges) prior to the beginning of the project. Environment Canada operates a hydrometric station at the South Perimeter Bridge (SPB), (Figure 3.1) and the City of Winnipeg maintains a station at the Fort Garry Bridge (FGB). The SPB and FGB gauges measure water level every 15 and 10 minutes, respectively.

Using the water level data from these two gauges throughout the study period, the water surface slope was calculated by dividing the difference between these two water surface elevations (WSE) by the flow length between the two bridges. The average WSE at each cross section for a single day was used to provide water surface frequency analysis.



Figure 3.1: SPB water level recording station

3.2.2 Bathymetric Survey

Accurate numerical modeling, which can simulate hydrodynamic process in any river, requires high-resolution bathymetry data to represent the physical shape of the river. In July 2012, the field data collection program was initiated to collect detailed river bathymetry of the 10 km reach of the Red River between SPB and FGB. Several days were required to complete the surveys. Throughout the surveys, two-dimensional positioning was achieved using an Acoustic Doppler Current Profiler (ADCP); (the Sontek RiverSurveyor M9) with RTK GPS option. Positional accuracy of survey points for the bathymetry survey was approximately ± 3 cm in the horizontal direction (Sontek, 2009). The Sontek RiverSurveyor system was mounted on a boat with a rope (Figure 3.2).



Figure 3.2: Photograph of the M9 device and hydroboard as close as possible to the bank

As the boat and the ADCP moved during the collection, one vertical down-looking measurement was obtained at the boat's position each second. Boat speed was maintained under 1 m/s to collect data at a high spatial resolution. Maintaining this velocity ensured that adequate accuracy on the discrete river geometry points was achieved within the shortest measurement time possible.

The survey began at the upstream end and proceeded in the downstream direction. The bathymetric measurement method comprised of two parts: first the moving boat with the ADCP was driven parallel to the shoreline as close as possible to the banks, along both sides of the river. Then, three more paths in the upstream and downstream direction on the middle of the river and between the middle path and shorelines were conducted to collect more precise river geometry while the water level was high.

In the second part of collecting bathymetry data and after travelling the longitudinal paths, sufficient resolution was attained by moving the ADCP across transects along the Red. During this step and for each transect, two distinguishable reference points on both sides of the river were selected to keep the path straight and make sure that adjacent transects were within 12 meters of each other. All data was directly sent to a Toughbook computer with M9 survey software. RiverSurveyor provided real-time bathymetric data in tabular and graphical formats, with water velocity, water temperature, boat speed, positional tracking from the starting point of sampling, time duration, and depth plotted against horizontal distance. The recorded bathymetry from June 18th, 2013, is shown in Figure 3.3 as an example.

All bathymetric data was recorded in the UTM coordinate system (Zone 14N), with respect to the river bottom. For further use, the measured water depths were converted to elevations based on the water surface elevations at both bridges. This was accomplished using custom built MATLAB code. In this study, every point was referenced to the WGS84 vertical datum. Figure 3.4 shows 4 cross-sectional surveys which were converted to elevations.

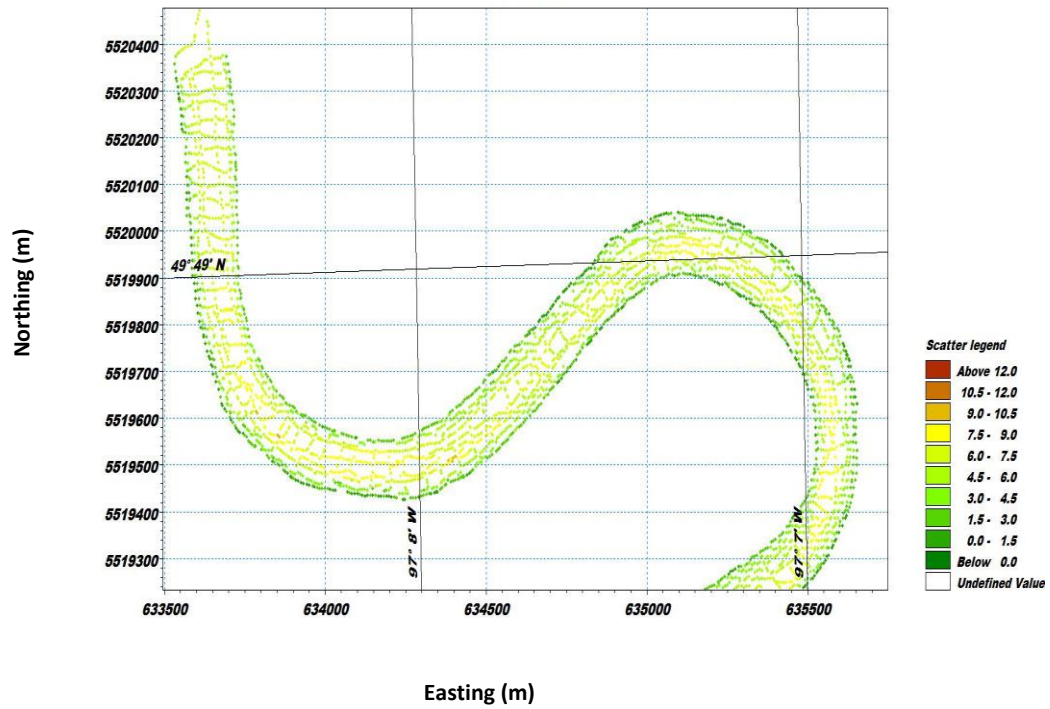


Figure 3.3: Bathymetric survey from June 18th, 2013

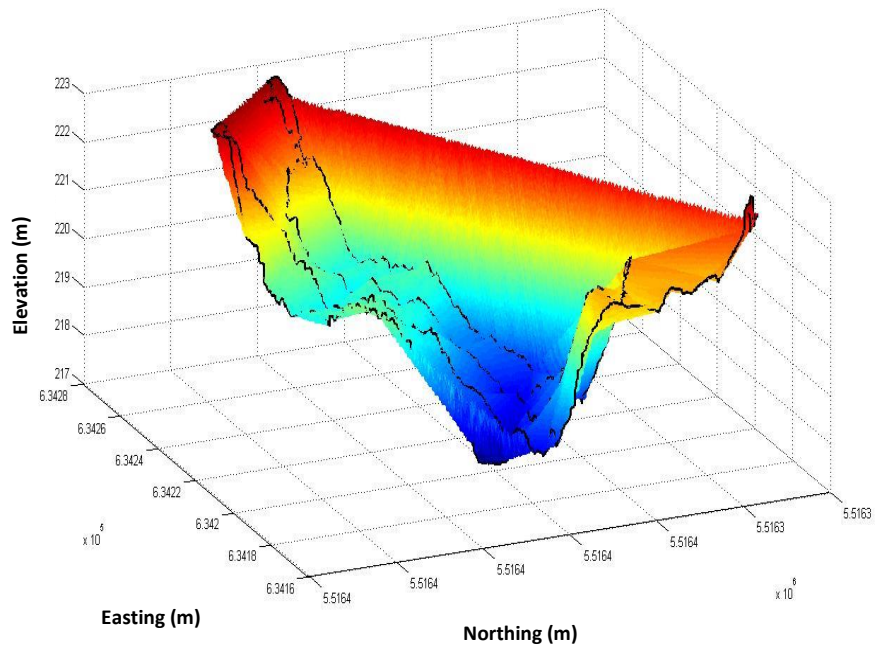


Figure 3.4: Elevation of four cross sections

The precise time associated with each water depth measurement was used to convert to elevation taking into consideration the changing water surface profile during the bathymetry measurement period. For example, on June 19th, the recorded water profile fell by 30 cm throughout the period of measurement.

More than 300,000 discrete river geometry points were collected along the reach while measuring bathymetry. The river bottom topography data were converted to a data file in XYZ format to import to MIKE 21 to produce a bathymetric configuration and develop the hydrodynamic model for the study site.

3.2.3 Redoing Bathymetry

The study objectives include measuring the overall impact of flow-induced erosion on the river bed over the entire study site, and monitoring rates and locations of riverbank widening processes. In order to understand if erosion or deposition could be monitored, additional field measurements were required. Therefore, bathymetric surveys were repeated to assess river geometry changes. On June 11th, 2013, after a high flow event, banks were resurveyed to quantify the erosion of the riverbanks, with respect to the 2012 bathymetry data. In addition, several predetermined cross sections along the reach were resurveyed as monitoring points to assess any bed elevation change after a high flow in early May 2013 (Figure 3.5).

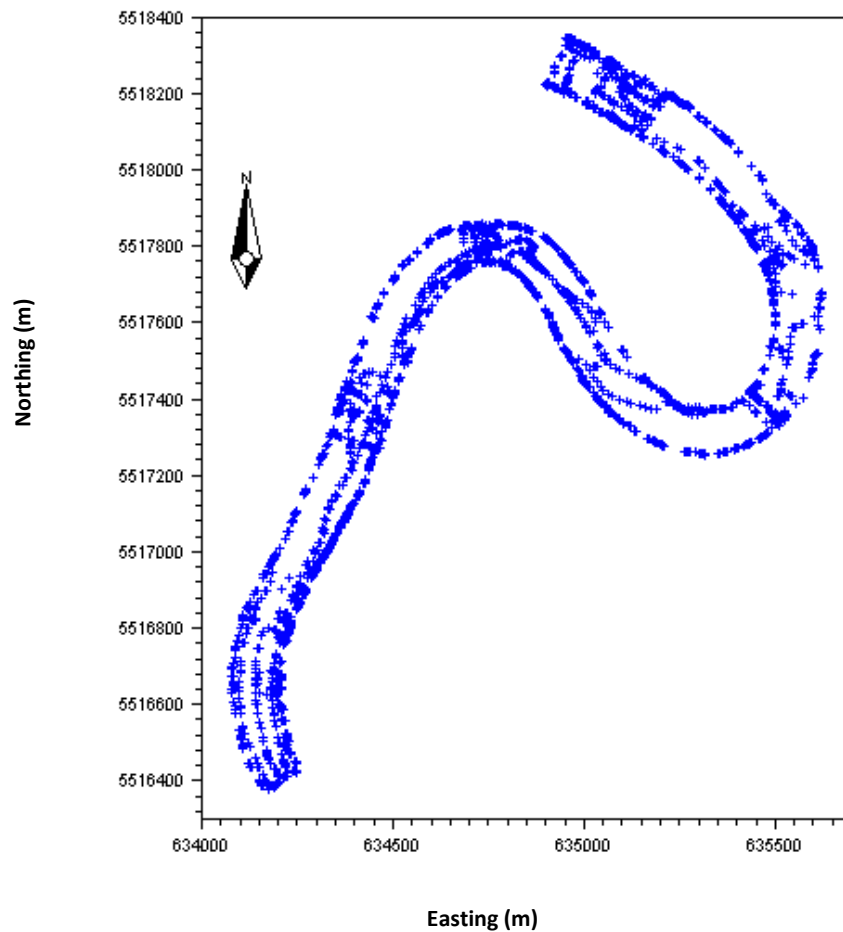


Figure 3.5: Redoing bathymetric points after high flow in 2013

Additional bathymetry investigations were taken on different portions of the 10 km reach of the Red River on September 4th, 2013, when the water level was low to calculate actual river elevation change (likely deposition due to low flow). Moreover, on August 14th, 27th, 28th and September 9th, 2014, a complete bathymetric survey was undertaken for the entire reach in order to assess river bathymetry changes over 2 years.

Throughout the surveys in 2014, two-dimensional positioning was achieved using the HydroSurveyor (a firmware upgrade to the M9) which was able to collect five water column depth profiles using five beams at every boat position each second. Positional accuracy of survey points for the bathymetric survey using HydroSurveyor was also approximately ± 3 cm in the horizontal direction (SonTek, 2013).

The values of depth, velocity, northing, and easting at each point were recorded to measure large-scale movements between surveys. Elevations for every single point compared easily between surveys (if that point was present in multiple surveys). When a point was taken at one of the data sets, the associated point was distinguished from other bathymetry data sets using a MATLAB program, achieving centimeter-level positional accuracy for this study. The results for all resurveying analysis will be presented in Chapter 4.

3.2.4 Flow Discharge and Velocity Measurements

Flow discharge and velocity measurements at sufficient temporal and spatial resolution were conducted along the reach mainly for numerical model development, calibration and validation by using the M9 (Figure 3.6). In this figure, the x-axis indicates open water season in 2013, from early April to the formation of border ice in the second week of November. The primary y-axis shows water surface elevation at SPB and secondary y-

axis indicates the number of discharge measurements that were undertaken during a particular week.

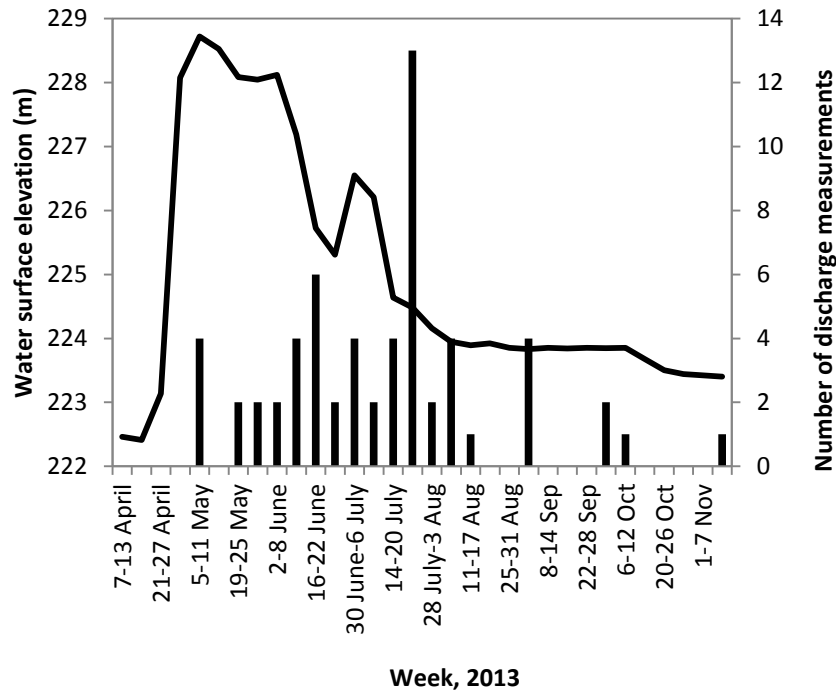


Figure 3.6: Number of discharge measurements over time, weekly basis

For discharge measurements the M9 was mounted on the boat or from the SPB using a rope and the M9 was moved from one bank of the river to the other. (Figure 3.7) Two restrictions were included with this task: 1) the M9 velocity should not exceed the water velocity, and 2) during discharge measurement, the cross sectional path of the M9 should be perpendicular to current flow.



Figure 3.7: Discharge and velocity measurement from top of the SPB

In a particular day and on one site, more than one cross sectional discharge measurement was conducted in order to obtain a more reliable discharge. In addition, this extensive field monitoring database with other data collection activities were combined to develop a site specific stage-discharge curve, suspended sediment rating curves and average applied shear stress as well as shear velocity estimation.

The velocity measurement method was comprised of two parts: moving and stationary M9 velocity measurements. The moving M9 velocity measurement procedure was undertaken mainly for the investigation of velocity distributions along the reach. As was mentioned earlier, during bathymetry data collection, the M9 was also able to measure mean water velocity and velocity components at each single point on the river. These data were used to present measured velocity distributions longitudinally on the reach and for various cross sections. After investigating the Red River roughness height, the measured velocity distribution data were used to demonstrate the applied shear stress distribution under different flow conditions.

Instantaneous vertical distribution of streamwise velocity was significantly scattered in the water column due to the turbulent behaviour of the river. Therefore, this data could not present two dimensional velocity pattern and other flow characteristics. In order to obtain important variables (such as shear velocity) and to explain river processes (such as sediment transport), a stabilized measurement of vertical streamwise velocity distribution was needed. Long term stationary velocity measurements have been widely accepted to obtain time-averaged and stabilized velocity profiles. In this study, point measurements were conducted while the boat was anchored, or rope was tied to specific points of the SPB. The data was collected for 10 minutes to record sufficiently accurate flow properties.

Discharge and velocity profiles across several sections along the reach were measured on July 23rd, 2013, (Figure 3.8). This was done to provide a check on the magnitude of the velocities simulated by the numerical model in order to calibrate it for prediction of hydrodynamic behaviour of the Red River. During this field activity, it was observed that there were sections where the M9 had difficulty measuring velocity and discharge. The M9 frequently lost GPS signal, especially close to University of Manitoba due to signal inference around the University.

Moreover, to calibrate the model for the conditions at the time of the field survey, it was necessary to parameterize the flow resistance coefficient. Therefore, the discharge measurement procedure was also focused on the accurate measurement of the

variables such as average hydraulic radius, average cross sectional area, and average velocity to calculate the Manning's coefficient (referred to as n in the rest of this thesis).

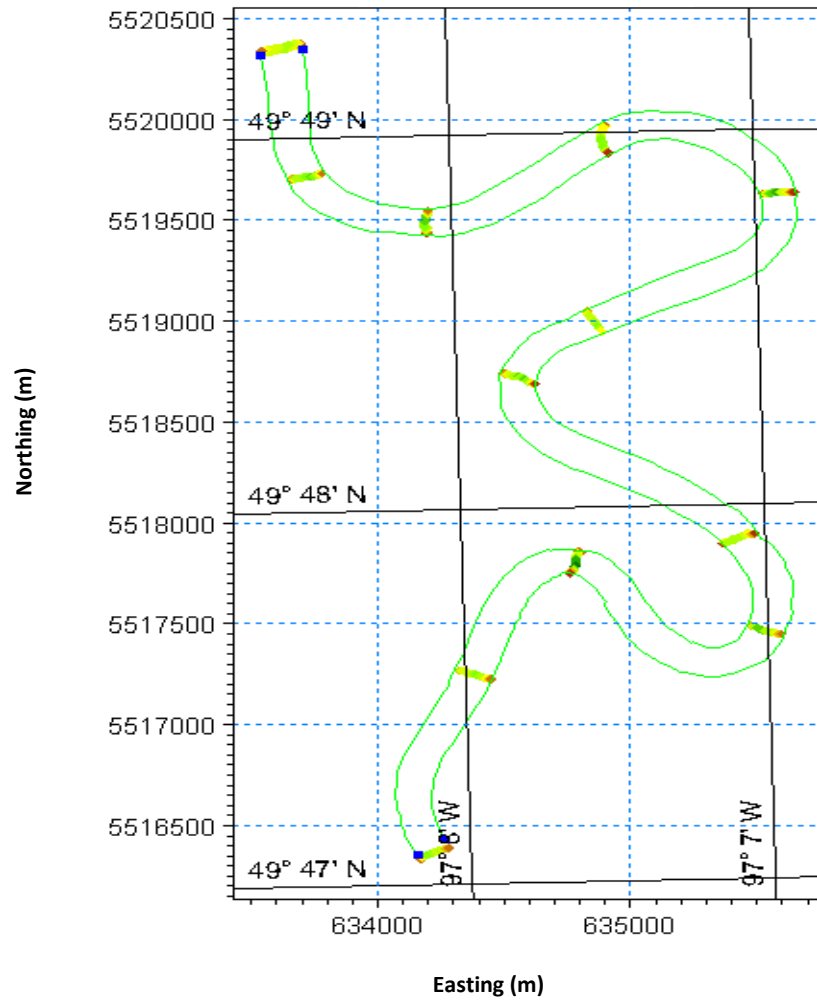


Figure 3.8: Plan view of 12 discharge and velocity measurements on July 23rd, 2013.

3.2.5 Water Sampling Program

As mentioned in the previous Chapter, bank erosion has significant contribution to sediment along rivers. Hence, one of the objectives of this study was to identify annual and seasonal erosion and deposition processes by performing total suspended solid (TSS) and suspended grain size distribution (GSD) tests. Therefore, extensive suspended sediment sampling was undertaken between May 5th and October 10th, 2013, in order to quantify the TSS and GSD along the river. Most of the field monitoring was undertaken at the upstream and downstream ends of the study site. In addition, multiple surveys were conducted along a 20 km reach of the Red River that extended 5 km upstream and 5 km downstream of the study reach boundaries.

Detailed field data was collected in an attempt to determine a wide overview of variation in vertical, cross-sectional and longitudinal suspended solids and their grain size distribution over time within the study reach and 10 km beyond. These spatial and temporal water-sediment sampling data collections were then applied to understand erosional and depositional patterns within the river by developing a relationship between the Red's flow properties and its TSS. Collected water-sediment samples were brought and tested in the University of Manitoba's laboratories to determine the total suspended solid (TSS) concentration and particle size distribution. Moreover, this intensive field activity sought to test the feasibility of using an ADCP for suspended sediment monitoring, instead of water sampling which is more time consuming.

3.2.5.1 Water Sampling Program at Bridges

Suspended sediment samples were taken along the SPB and FGB, as test cross sections, at different depths and locations throughout the water body over time to obtain sediment characteristic data. On each sampling day, an attempt was made to sample the same volume of water at both bridges by timing the measurements with respect to the river's flow velocity. This field work was also carried out in an attempt to observe and record the effect of the rising, peaking and falling of the 2013 hydrograph on suspended solid concentrations.

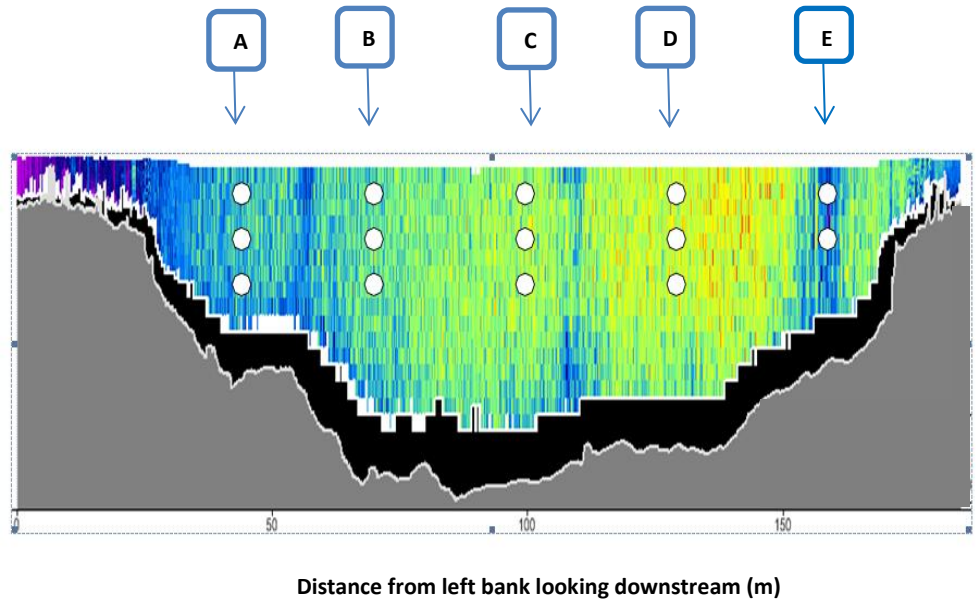
Collecting water samples was performed by conventional bottle sampling (Geo Scientific Ltd Van Dorn Sampling Bottle) using 500 ml and 250 ml water bottles to collect point water samples from the bridges using a marked rope (Figure 3.9). During high flow periods, to keep the marked rope as straight as possible from the bridges, 4.5 kg of extra weight was added to the water sampling device. Table 3.1 and Figure 3.10 show the sampling locations along typical cross sections looking downstream.



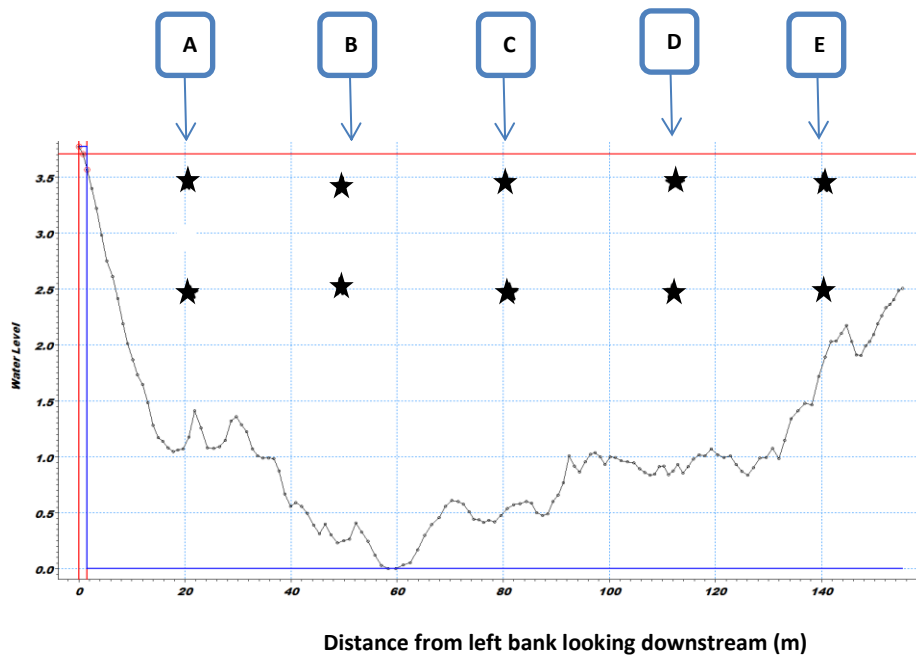
Figure 3.9: Water sampling equipment

Table 3.1: Water-sediment sampling locations at SPB

Profile	Easting	Northing
A	634174.8	5516329.9
B	634205.5	5516348.8
C	634238.5	5516368.7
D	634270.7	5516386.1
E	634282.3	5516398.9



(a)



(b)

Figure 3.10: Water sampling locations at SPB (a) and FGB (b) looking downstream

At each profile, only 2 or 3 points were sampled at 1 m, 2 m, and 3 m below the water surface. During low flow and at the SPB only 4 water columns were sampled (profile E was part of the bank). Often times at the SPB, water samples were collected while fixed M9 measurements were taken to obtain time-averaged point velocities to seek a relationship between signal to noise ratio (SNR) and total suspended solids.

3.2.5.2 Water Sampling Program along the Red River

Suspended sediment samples were taken along 20 km of the Red River in 21 evenly-spaced locations at the middle of the river using a boat (Figure 3.11). Furthermore, during this field work the stationary M9 was operated for about 10 minutes at each location to collect flow velocity data and to test the ability of the M9 to monitor suspended sediment along the Red River. This sampling method was carried out on June 12th, August 15th, and October 10th, 2013, and produced enough samples to provide spatial TSS and particle grain size distribution information. These water-sediment point samples were collected from 2 different depths: 1 meter below the surface water, and as close as possible to the bed based on ADCP depth measurements.

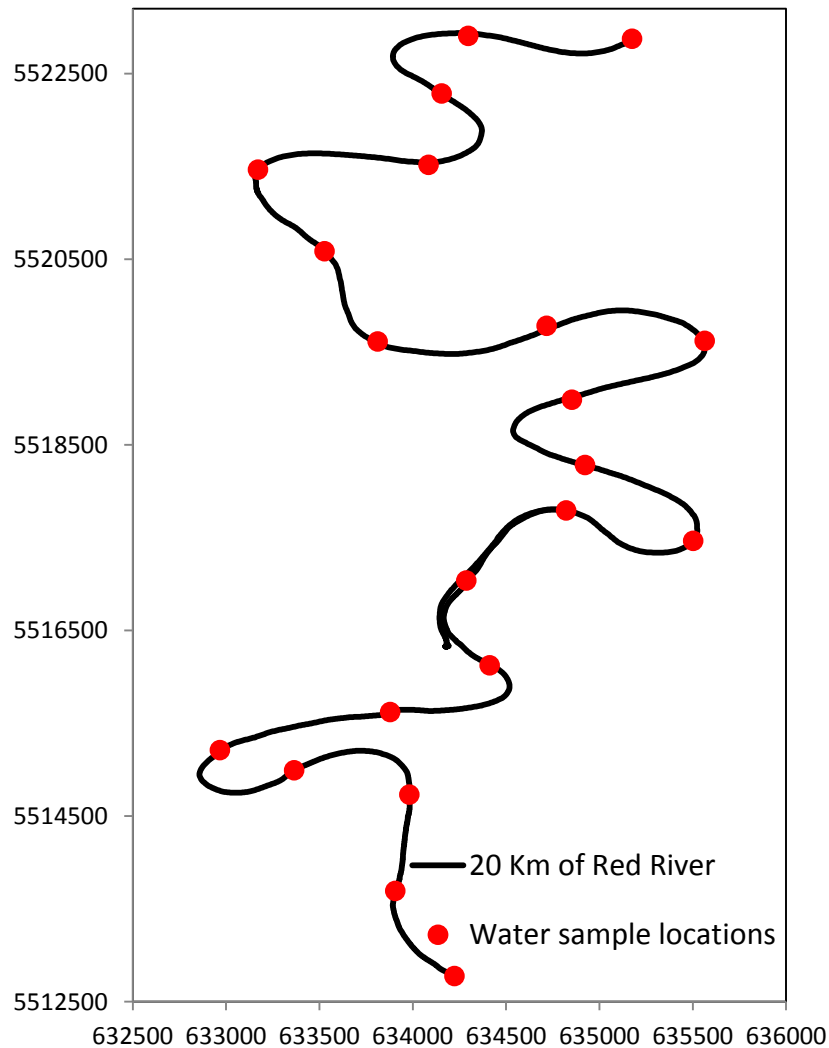


Figure 3.11: Water sampling locations along 20 km of the Red River

3.2.6 Soil Sampling Program

Six soil sampling sites were selected to determine soil characteristics and the erodibility parameters (τ_c and k_d). The soil sampling program was focused on cohesive soils without vegetation all along the study reach study in order to represent the variety of different cohesive soils present in the Red River banks. In addition, from the Maple Grove Park boat launch, one sample of deposited material was collected in order to

determine the basic geotechnical characteristics and erodibility parameters of recent deposits.

Using undisturbed samples is an important factor when studying cohesive sediment since it is very dependent on natural soil structure. To understand the effect of applied shear stress on soil samples without any effects from weathering, the samples were collected at least 0.5 m below the soil surface at locations near the water surface that had just recently been exposed to the atmosphere. Samples were obtained using an ASTM Shelby tube with a 76.2 mm outside diameter in order to take undisturbed samples (Figure 3.12).

The first site, MN1 is at the west bank near the SPB and the second site, MN2, is at the east bank near Maple Grove Park. The third and fourth sites, MN3 and MN4, are located at the outside and inside bends near the University of Manitoba, respectively. The last two sites, MN5 and MN6, are located at the west and east Red River banks respectively, close to St. Mary's Road and Normand Avenue (Figure 3.13).

Soil samples from MN1 and MN2 were collected on October 24th, 2012 and October 10th, 2013 respectively. Samples from MN3, MN4, MN5 and MN6 were obtained on June 21st, 2013, and the Shelby tube sample of deposited material was collected on June 25th, 2013. The study sites are summarized in Table 3.2.

One additional Shelby tube sample from each soil location was collected for testing and analyzing the effect of winter conditions (freezing and thawing) on cohesive riverbank erosion along the Red River. Soil samples were also tested in order to obtain basic geotechnical properties such as: identification of soil type, d_{10} , d_{50} , d_{90} , Atterberg Limits (Plasticity Index, Plastic Limit, Liquid Limit), and the content of sand, silt and clay. To maintain soil samples in their original quality, the samples were sealed and kept in a refrigerator at the University of Manitoba until testing.



Figure 3.12: Soil sampling procedure using Shelby Tube

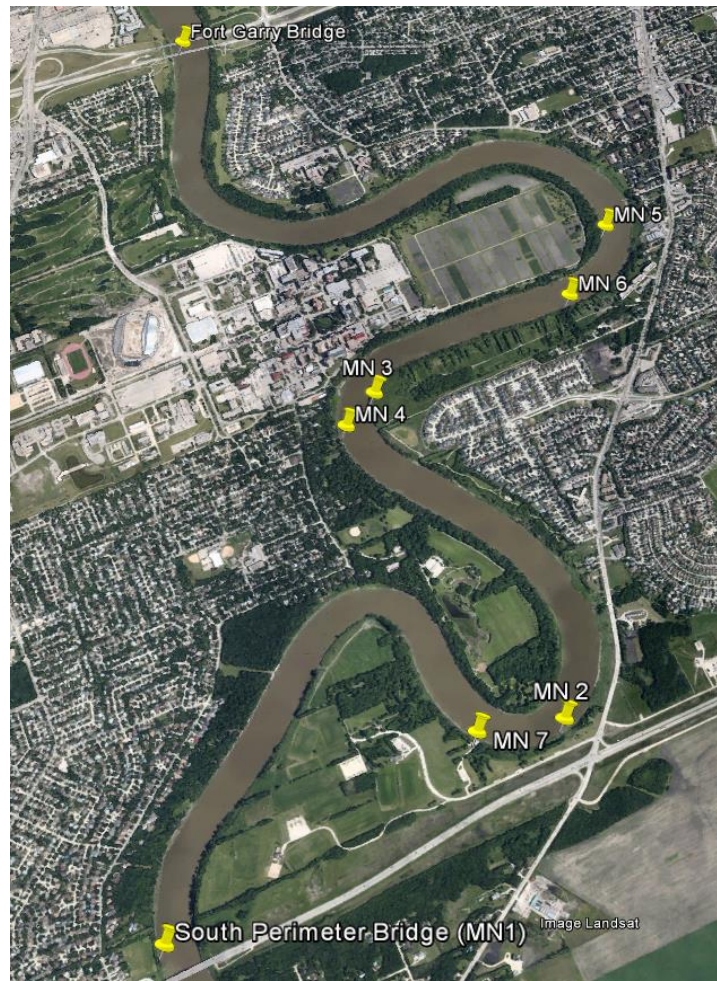


Figure 3.13: Soil sample location site plan

Table 3.2: Soil and sediment sampling location

Soil Sample Name	Easting	Northing
MN1	634132	5516387
MN2	635497	5517311
MN3	634623	5518661
MN4	634526	5518502
MN5	635527	5519540
MN6	635395	5519181
MN7	635173	5517240

3.3 Laboratory Testing

After data collection in the field, water and soil samples were transferred to the University of Manitoba for further processing. The following sections document the processes and methods used in testing the samples obtained from the field activities. The laboratory analyses used to quantify sample properties and the majority of the experiments were carried out in the geotechnical and environmental laboratory in the Department of Civil Engineering.

3.3.1 TSS Testing

Field samples were brought to the University of Manitoba to process. TSS for each sample was measured according to ASTM D3977. Therefore a filter and a vacuum were used to conduct the traditional filter method. After pouring the water sample in a dish, the vacuum separated the water from the suspended sediment. By dividing the net sediment mass by the volume of the original sample, TSS was calculated in units of mg/l.

3.3.2 Water-Sediment Size Testing

Since river water is affected by the size and characteristics of the sediments it carries, measuring the size of sediments in a series of water samples can present a brief overview of the morphological processes along the Red River. Water samples were transferred to the Richardson Centre for Functional Foods and Nutraceuticals (RCFFN) at

the University of Manitoba in order to obtain the grain size distribution of the sediment using a Mastersizer 2000.

The Mastersizer 2000 is a particle size analyzer capable of testing a variety of wet and dry samples (Figure 3.14). This apparatus uses a laser diffraction technique and has two main parts: the sample dispersion accessory (the sampler unit) and the optical unit (instrument) to establish the particle size distribution and other particle size statistics (Mastersizer 2000, 1999).

The sampler unit contains a tank, a pump, a stirrer, and an ultrasonic probe and the purpose of this unit is to stabilize the sample before/during the measurement process and then deliver the sample to the optical unit for measurement. The sample must be mixed well to represent the whole original sample concentration. For the water-sediment test, “the samples dispersed in a liquid” handling accessory was used to avoid flock formation in the samples.

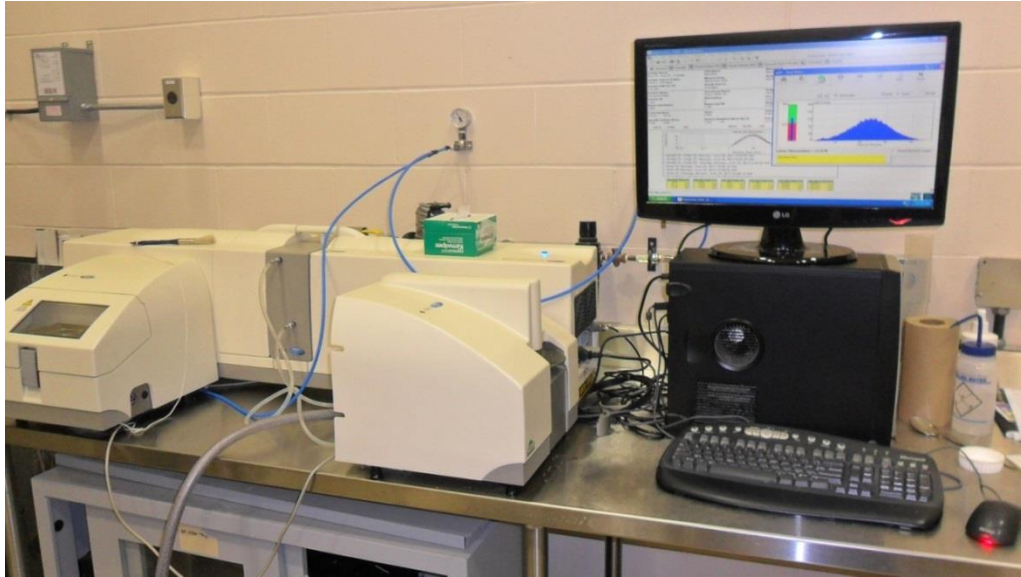


Figure 3.14: Mastersizer 2000 device and computer system in the Smart Park

The optical unit uses a solid-state light source or LED and a helium neon laser light for the smaller and larger particle measurements, respectively. The Malvern software controls all the functions during a measurement and produces the results.

3.3.3 Erosion Measurement Device (EMD) Testing

One of the main objectives of this study was to determine τ_c and k_d for each soil sample using the EMD. This device can determine the erosive behavior of soils under tightly controlled laboratory conditions. The device is a 2.80 m long rectangular conduit with a width of 10 cm and a depth of 5 cm. It has a hole at the bottom which is located 2.5 m downstream from the inlet. The conduit is able to pass 0.2 – 3 m/sec flow velocities. The EMD contains two chambers which are separated by a short wall, testing tube, pump, ultrasonic velocity measurement device and 4 inches of short pipe. The

ultrasonic device measures the flow velocity in the pipe. Figure 3.15 shows the EMD and the location of the hole used to extrude a sample through the bottom of the conduit.

An electric jack is used in the geotechnical laboratory to remove a sample from a Shelby tube into the test tube with minimal disturbance (Figure 3.16). The testing tube with the prepared sample is installed vertically over the piston at the bottom of the conduit. After the testing tube is fastened in its place, the soil sample is brought into the conduit by pushing the piston with the screw jack. Once this is performed the soil is trimmed flush with the bottom of conduit and the top lid of the conduit is clamped (Figure 3.17).



Figure 3.15: Erosion Measurement Device (EMD)



Figure 3.16: The electric jack device to put sample into the testing tube

To begin an EMD test, the sump is filled with water. Water is pumped from one of the containers to the conduit using a variable speed pump. Water passes through the pump into the conduit and then enters another container to reduce turbulence.

The pump is turned on at a low frequency and slow water velocity (0.1 m/sec), and the air valve is opened until all air bubbles have escaped from the conduit. The flow velocity in the pipe is converted to the average velocity in the conduit using the continuity equation.



Figure 3.17: Soil sample preparation for EMD test

After the velocity is set, the soil is pushed 1 mm into the conduit with the screw jack. The operator monitors the erosion visually until 1 mm of soil is eroded or after 1 hour, whichever comes first. The pump is then turned off and the water is drained from the conduit. The top lid of the conduit is opened and the soil surface is smoothed as shown in Figure 3.17. This process is repeated a number of times with increasing flow velocities. The soil is again pushed 1 mm into the flow until measurable erosion begins to occur, and the amount of time to erode the 1 mm is recorded by the operator. Since shear stress is directly proportional to the fluid velocity at the soil-water interface, the erosion rate can be determined for several different shear stresses by changing the flow velocity.

If a relatively significant amount of erosion occurred at the start of the test (first 5-10 minutes) but not for the remainder, the rate was interpreted as 0 mm/hr and τ_c had yet to be reached. The initial erosion was attributed to soil disturbance caused by the

surface preparation procedure. The results from the EMD tests (after repeating for between 3 and 5 velocities) were used to developed charts of erosion rate versus shear stress in the flume.

As previously mentioned, a method was established to estimate shear stress in the EMD. The following equation was used to calculate applied shear stresses in the conduit:

$$\tau_a = \frac{1}{8} f \rho V_{avg}^2 \quad \text{Equation 3.1}$$

Where, ρ is the mass density of water (kg/m^3), which is assumed to be 1000 kg/m^3 , V_{avg} (m/s) is the measured mean velocity, and f (-) is the friction factor that is calculated from Colebrook's equation (Munson et al., 2012):

$$\frac{1}{\sqrt{f}} = -2 \log\left(\frac{\zeta/D}{3.7} + \frac{2.51}{\text{Re}\sqrt{f}}\right) \quad \text{Equation 3.2}$$

Where ζ (m) is the sample surface roughness which was estimated as $0.5d_{50}$, D (m) is the hydraulic diameter, and Re (-) is the Reynolds number in the conduit and was calculated as:

$$Re = \frac{\rho V_{avg} R}{\mu}$$

Equation 3.3

where μ (kg/(m-s)) is the dynamic viscosity and R (m) is the hydraulic radius .

3.3.4 Geotechnical Laboratory Testing

Undisturbed cohesive soil samples (Figure 3.18) were tested to determine several physical and electrochemical properties such as: particle size distribution, specific gravity of fine soils, water content, electric conductivity (EC), cation exchange capacity (CEC), Atterberg Limits (AL), sodium adsorption ratio (SAR), and organic matter (content) (OM). Many of these parameters have been related to the erosional properties of cohesive soils in the literature.



Figure 3.18: Soil sample for geotechnical tests

Grain size distribution tests for coarse and fine soils were performed to determine the relative percentage of soils in the samples using the ASTM D422 standard method (Figure 3.19). In the water content determination test, all samples were tested in accordance with the ASTM D2216 standard method. Since all soil samples were fine-grained soils, Liquid Limit, Plastic Limit, and Plasticity Index were determined in accordance with ASTM D4318-0. Taylor and Francis group LLC, chapters 15 and 18, were used to perform EC and CEC, respectively; in addition ASTM D854 and D2974 were followed in order to measure the specific gravity and organic content, respectively. These geotechnical properties of the site soils are presented in Chapter 4.

Once these tests had been completed, attempts were made to correlate the erosion rate with commonly measured soil properties. In other words, the EMD test results were compared with the soil geotechnical properties to determine if a correlation between these properties and the erosion rate (or τ_c and k_d) could be established.



Figure 3.19: Hydrometry test to determine the fines particle size distribution

3.4 Numerical Modeling

Water in shallow depths (rivers) flows in three dimensions; nevertheless two-dimensional equations can often sufficiently describe this process by using depth-averaged values in the continuity and momentum equations. The MIKE software package was used in this study to simulate flow properties in two-dimensions within our study reach on the Red River.

The MIKE software provides valuable tools for mesh generation, data interpolation, and graphical visualization. Two products of the MIKE software (MIKE Zero, MIKE 21 Flow Model FM) were used in this study. MIKE Zero is a platform or Graphical User Interface (GUI) which was used to create the mesh of the study area, and MIKE 21 simulated hydrodynamic conditions and computed applied shear stresses within the reach.

The MIKE 21 Flow Model FM program is a two dimensional depth-averaged finite volume flexible mesh commercial model. Two modules (Hydrodynamic and Mud Transport) of the MIKE 21 Flow Model FM were used. Mud Transport is a program capable of replicating the boundary shear stresses on cohesive rivers and can be applied on the Red.

3.4.1 Mesh Generation

In order to numerically solve the hydrodynamic shallow water equations, the physical study domain should be represented as discrete cells or grids in such a way that river bed elevations will be assigned to each node. The river elevations were acquired from field measurement and imported to the software in XYZ format.

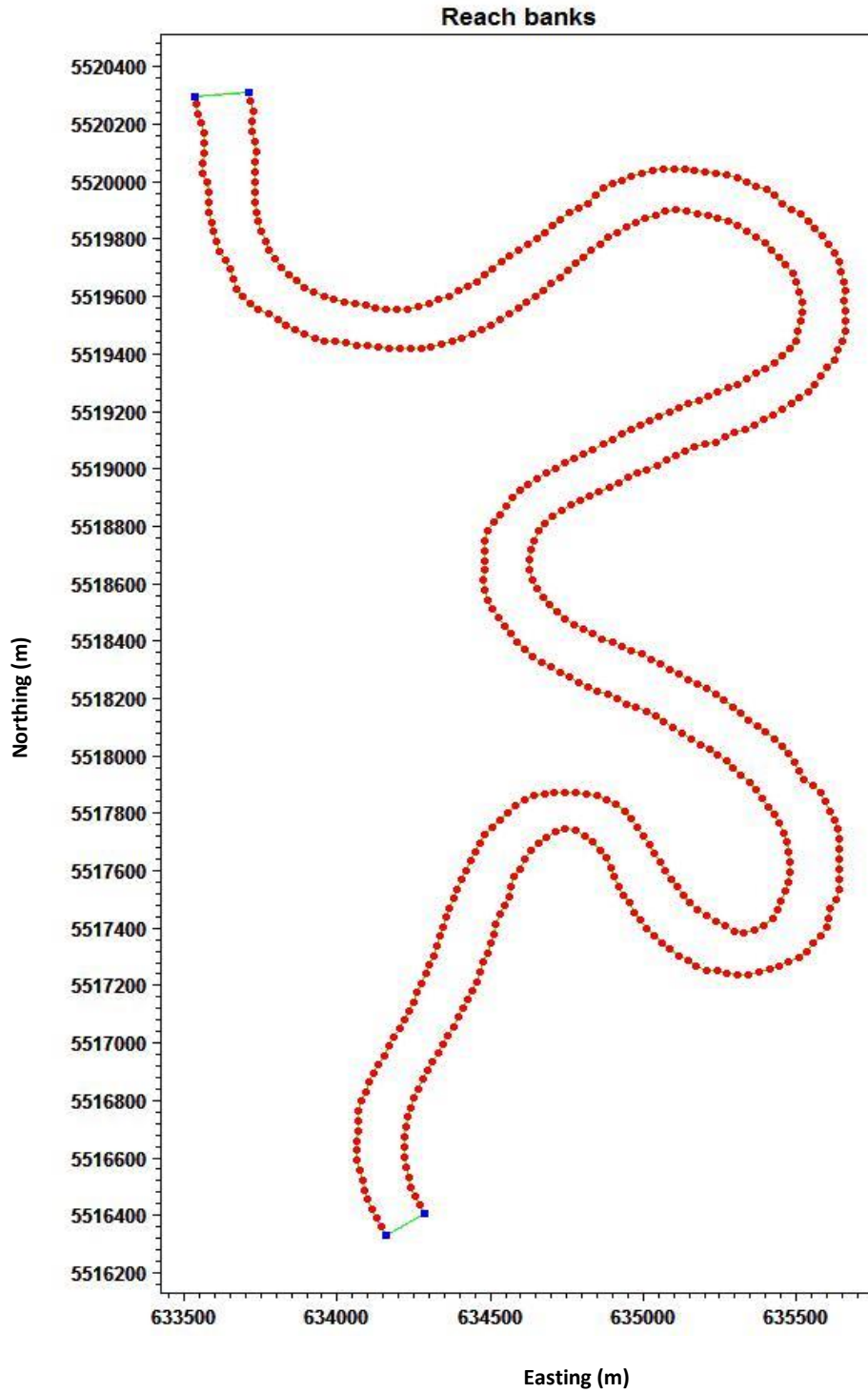
A mesh is defined as a network of triangular elements constructed from nodes, and is delimited by the bathymetry and water surface at the bottom and the top, respectively. In other words, each triangular mesh element defines a three-dimensional element. In this research a preliminary discrete domain was developed using the MIKE Mesh Generator. Mesh Generator defines the computational domain which can map out the physical domain of the Red and also provides an environment for creating, editing and presenting detailed bathymetry data. It accomplishes this by importing, or using the building drawing tools to assign a depth for each individual mesh for numerical calculation. The creation of a mesh requires the user to provide bathymetric data and to define the bank boundaries of the reach. An outer boundary condition was created

based on the extents of the survey data as permanent land and declares that no flow will occur in or out of the boundary along the river. Figure 3.20 displays these lines added to the model (a) as well as the triangular mesh (b).

After the mesh generation has been completed and smoothed, it is possible that a few elements may not have had elevation values specified. Therefore, interpolation is performed to fill in the blank meshes and create the bathymetric surface. Figure 3.21 shows the model domain, and the complete bathymetry used for hydrodynamic simulations over the flexible mesh. Once the river topography file has been prepared, the file can be exported for further use in MIKE 21.

3.4.2 MIKE 21 Flow Model FM Setup

The first step to use MIKE 21 FM is setting up the model. The site-specific setup was performed by using the data collected during the field survey. Creating a hydrodynamic river model using MIKE 21 FM involves several steps, including: selecting the model domain, discretizing data in time and space, defining the initial/boundary conditions, and calibration.



(a)

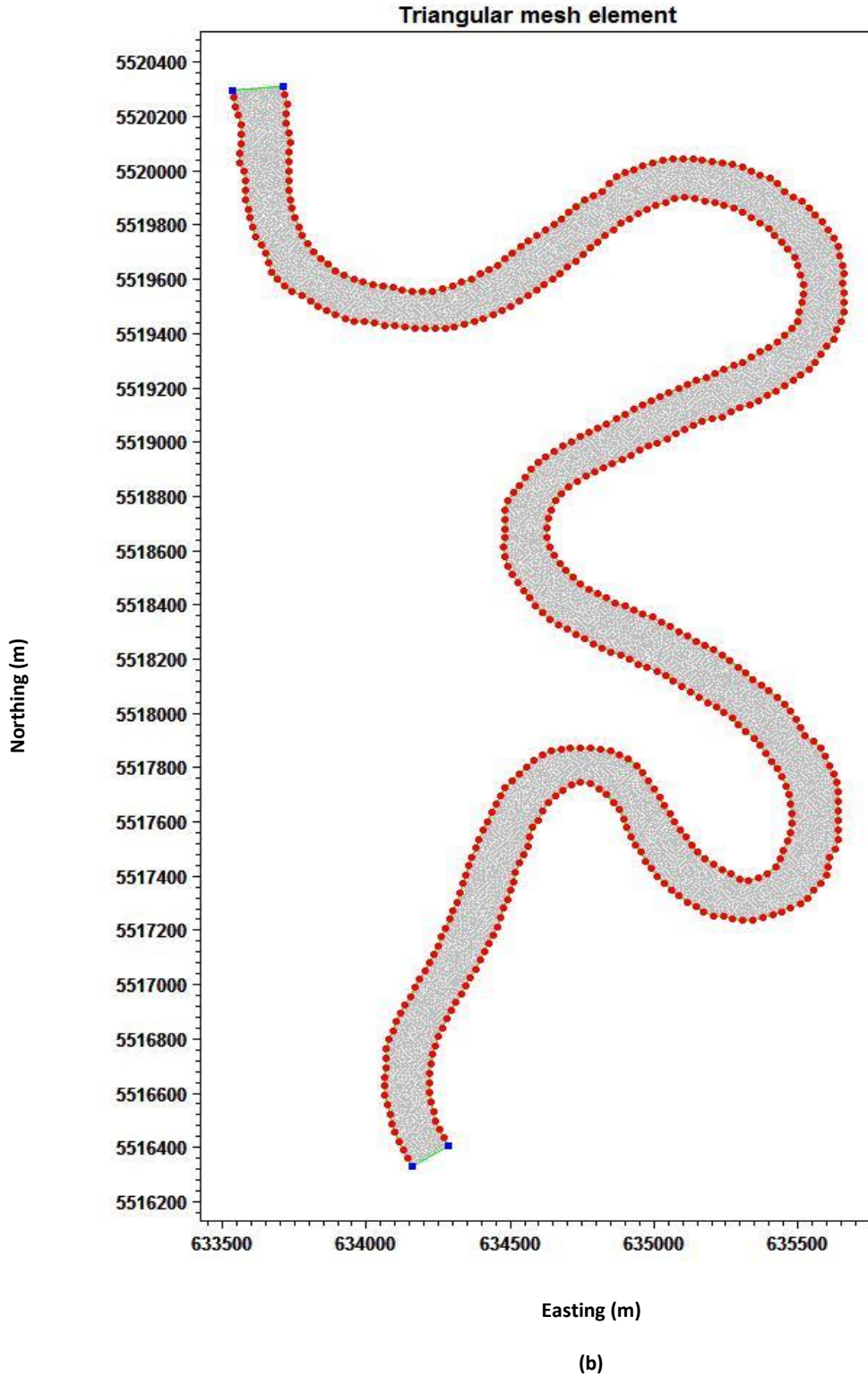


Figure 3.20: Reach banks location site plan (a) and triangular mesh element along the reach (b)

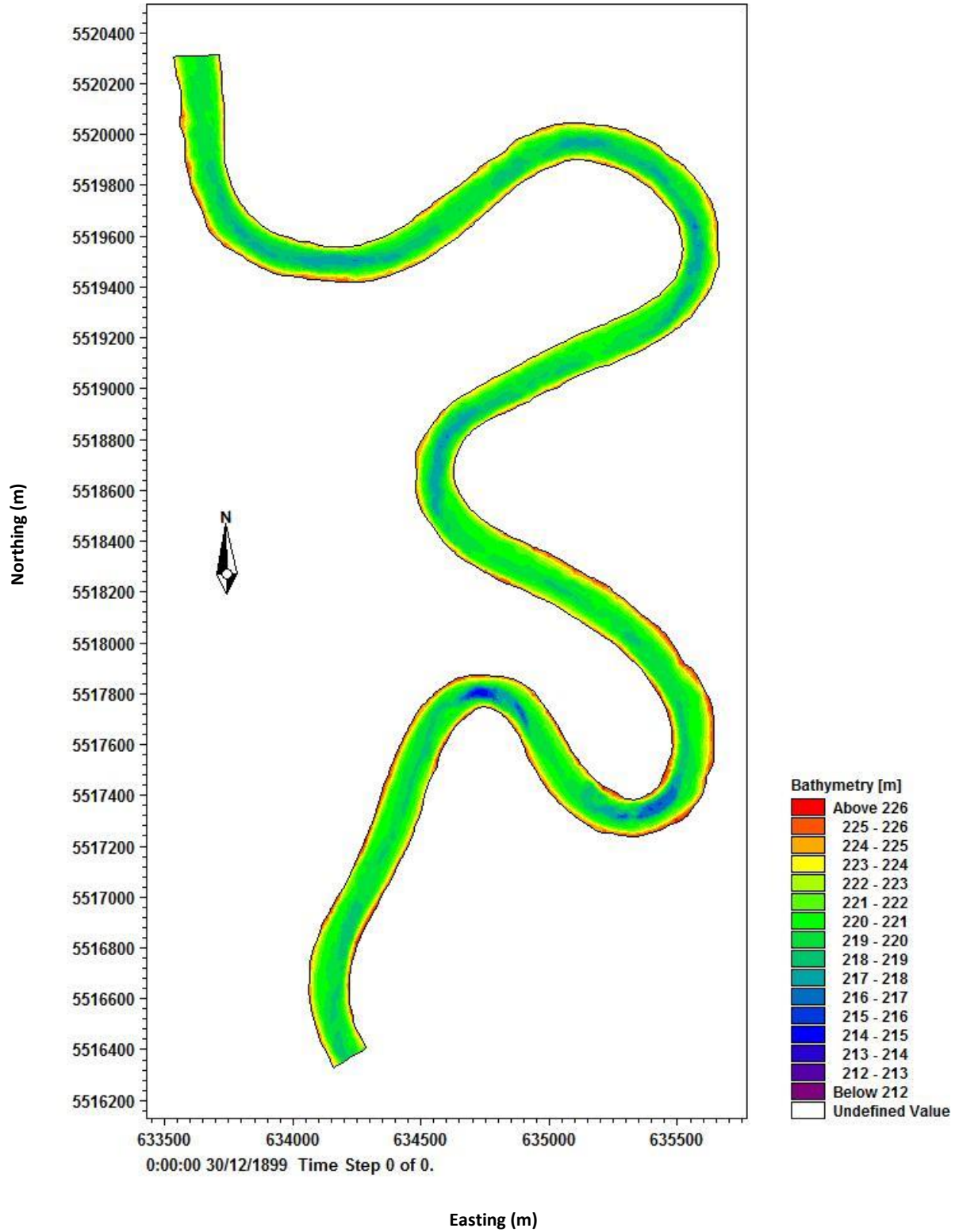


Figure 3.21: The complete river topography after interpolation

MIKE 21 Flow model FM requires boundary conditions at all open boundary points to begin computation. The inflow boundary condition was a discharge, and the water level was specified at the outflow boundary. These boundary conditions were determined based on the results of field measurements. Since significant applied shear stress occurs during peak flows, high discharge was used as the upstream boundary condition.

The water surface elevation was specified as the initial condition throughout the domain. The initial condition indicates the water elevation for each model element at time zero. Hydrodynamic modeling in the reach was carried out with a typical maximum discharge of 1100 m³/s and a simulation period of two weeks was selected to capture typical high flow conditions. Other basic input data used in the MIKE 21 Flow model FM development was based on software default values.

Any mathematical or numerical method must be calibrated, verified, and validated to make sure it represents its corresponding natural phenomena accurately. In this study the model was calibrated using the water level, velocity, and discharge. The model was calibrated by matching the observed water-surface elevations at the upstream site to moderate flow conditions (400 m³/s - 600 m³/s). Also, field observations of the depth-averaged velocity and water surface elevations were effective means to verify the assumptions (such as hydraulic roughness) and the simulated results. Therefore, the velocity calibration process was verified during 230 m³/s by comparing simulations

against velocity profile measurements produced by the M9 at 12 cross sections throughout the study reach.

4.1 Introduction

This chapter presents data processing for field activities and the results from experiments which focused on modeling and monitoring the effect of hydraulic shear stress on Red River bank erosion. The first part will show the flow properties and the estimation of boundary shear stresses for a wide range of discharges in the reach. Three different methods were used to determine hydraulic shear stress, including: averaged applied shear stress, log law, and numerical modeling. Also the law of the wall formula in turbulent open channel flows was used with measured velocity and depth data to model hydraulic shear stress accurately. Cohesive soil erosion was then estimated using three methods: 1) using the excess shear stress modeling method, 2) characterizing the particles in suspension along the study reach and 10 km beyond, and 3) resurveying the Red River over 3 years. These shear stress and erosion quantifications have been used to examine the research question on better understanding the effect of hydraulic shear on cohesive soils on the Red.

4.2 Water Level Data Processing

Water surface elevation data were collected at the upstream (by Water Survey of Canada) and downstream (by the City of Winnipeg) ends of the study area from June 2012 to November 2013, at 15 and 10 minute intervals, respectively. The average water surface elevations at each cross section for a single day during the data collection period were used to provide water surface frequency analysis. The process showed that a high water level on the Red River occurred during the spring month of May 2013; however, during the same period in 2012 the Red River water surface elevation was relatively low. Moreover, in 2013, a second high level was observed in early July (Figure 4.1). In 2013, the water level rose fast in less than one week and fell slowly over a period of 6 weeks. Quick rising of the water level was in response to the winter snowmelt runoff and the gradual falling was a result of the low gradient of the Red.

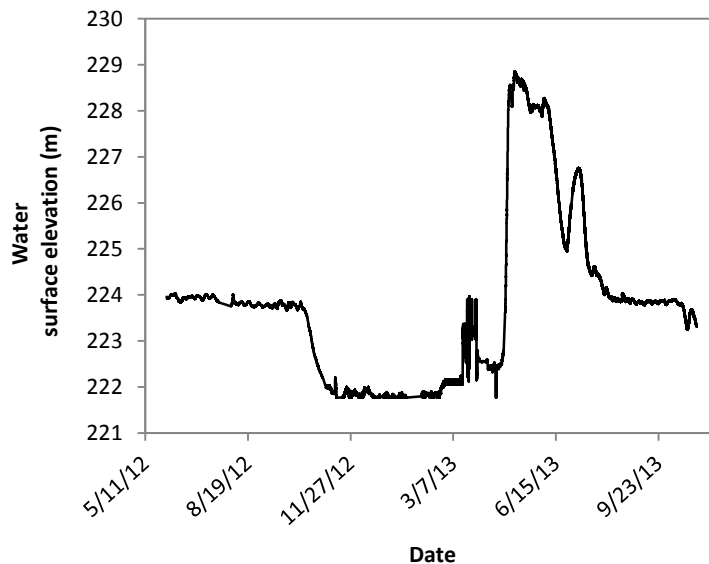


Figure 4.1: Daily water elevation for the Red River at the FGB Station (data from City of Winnipeg, 2012-2013)

These continuous records have been processed to explain the behaviour of water slope variation of the study reach (Equation 4.1). The maximum and minimum differences between measured water levels at the two boundaries were 0.47 m and close to zero, respectively. The Red River generally has an average gradient of 1: 23800 (Weiss, 2012) and the average channel gradient of the Red within the city of Winnipeg is approximately 1: 26000 (Kimiagharam et al., 2015b). The average gradient of the entire river and the river reach in the City of Winnipeg are close to our study reach gradient; therefore, the general flow property results obtained from this study can be applied to other reaches of the Red River. Since the water surface profile becomes extremely flat in low flow condition, this equation is only valid when the water level at the SPB is greater than 222.5 m.

$$(FGB)_E = (SPB)_E - \{0.0801[(SPB)_E] - 17.838\} \quad \text{Equation 4.1}$$

Water surface elevation between bank-full and low flow conditions typically vary by up to seven meters, generally between 222 and 229 m. For example, Figure 4.2.a shows the Red River close to the University of Manitoba on April 29th, 2013 when the water level was at a maximum value of 228.7 m, and Figure 4.2.b shows the same location on October 12th, 2013 at 223.5 m. The parts of river located below the minimum water level were considered as the bed of the river, assuming that, the erodibility of this part is proportional to the excess shear stress and is not mainly a function of other erosional processes.

The water surface elevation frequency information during the study period is presented in Figure 4.3. Based on 14 months of data collection, this histogram shows that approximately 14% of the time, water levels were in the range of 228-229 m (bank-full condition) where more flow-induced erosion was expected. The average water surface elevation of the Red is between 223 and 224 m. Figure 4.4 shows the SPB cross section with the minimum, average, and maximum water surface elevation.



Figure 4.2: Red River near the University of Manitoba on a) April 29th (WSE = 228.7 m), b) October 12th (WSE = 223.5), 2013

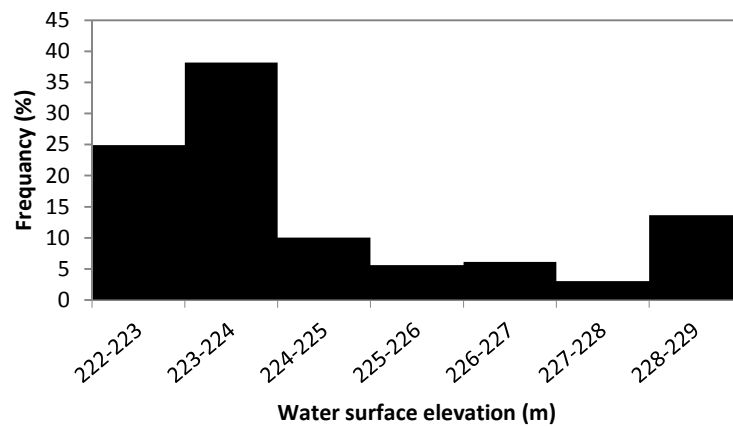


Figure 4.3: Water level histogram for the SPB during study period

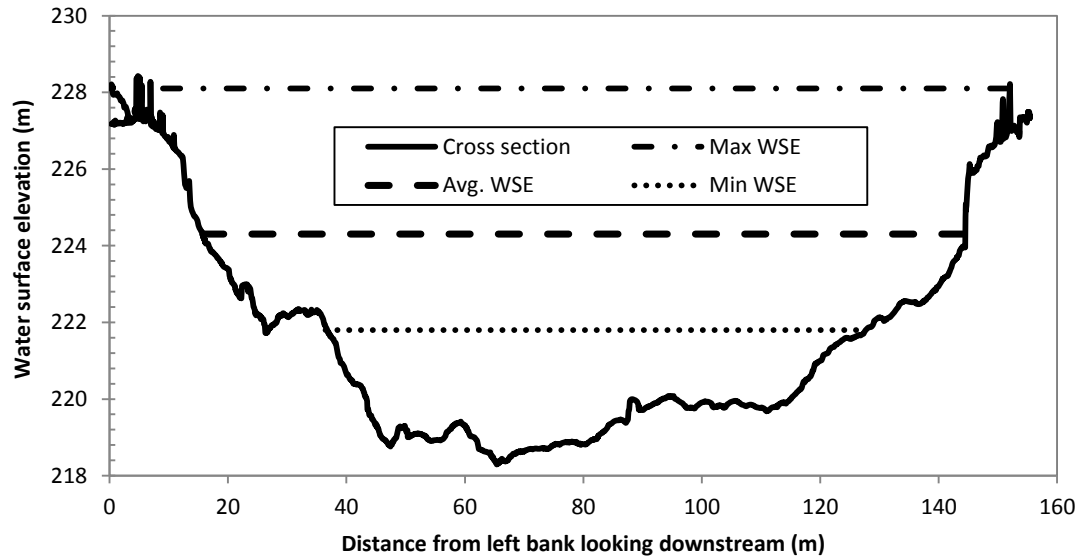


Figure 4.4: Maximum, minimum, and mean water level during the study period at SPB looking downstream

4.3 Discharge Data Processing and Stage Curve Development

During the study period, more frequent discharge measurements were performed at the upstream boundary and along the Red River to investigate the discharge variation. ADCP discharge measurements were carried out frequently during high flow and less frequently during the recession period. The results of all discharge measurement activities are presented in Table 4.1. Discharges varied between 50 and 1200 m³/s over the study period. The data reported in Table 4.1 suggest that the Red River is a wide, turbulent, slow moving river (subcritical flow) with relatively strong inertial, weak gravitational and viscous forces.

On November 12th, 2013, border ice formed along both sides of the Red and only the open water portion could be measured (Figure 4.5). Therefore the differences in the

mean velocity between Oct 10th and November 12th (although the discharge was the same) can be explained by differences in flow development along the reach in the freezing period.

Table 4.1: Summary of discharge measurement and other flow properties of the Red during the study period

Date (2013)	Discharge (m ³ /s)	Top water surface width (m)	Hydraulic mean depth (m)	Mean velocity (m/s)	Froude number	Reynolds number *10 ⁶
May 7	1208	165	6.75	1.083	0.13	7.6
May 8	1148	165	6.6	1.06	0.14	7.4
May 23	1031	165	6	1.044	0.14	7.1
May 30	997	164	5.9	1.002	0.13	6.8
June 6	1035	167	6	1.03	0.13	7.1
June 11	780	156	6.5	0.74	0.1	5.1
June 12	749	160	6.1	0.76	0.1	5.1
June 13	660	143	6.7	0.68	0.08	4.6
June 14	591	148	5.7	0.7	0.09	4.3
June 17	518	139	4.9	0.76	0.11	4
June 18	458	146	5	0.63	0.09	3.5
June 19	417	137	5.3	0.57	0.08	3.1
June 20	367	136	5.3	0.51	0.07	2.8
June 21	366	138	5.7	0.48	0.07	2.8
June 25	294	133	4	0.56	0.09	2.5
July 3	600	138	5.3	0.83	0.11	4.6
July 5	641	143	5.3	0.84	0.12	4.8
July 8	640	142	5.4	0.84	0.12	4.8
July 15	259	131	3.9	0.5	0.08	2.15
July 19	204	130	3.6	0.44	0.07	1.8
July 23	231	137	3.6	0.46	0.08	1.9
July 30	164	125	3.4	0.39	0.07	1.5
Aug 7	120	124	3.2	0.3	0.05	1.1
Sep 4	50	113	1.9	0.13	0.03	0.33
Oct 10	52	121	1.8	0.14	0.03	0.33
Nov 12	49	52*	3	0.31	0.06	0.93

*Border ice present



Figure 4.5: The Red River at SPB on November 12th when border ice formed on both sides of the river

The Water Survey of Canada provided several supplementary measured discharge and water level data sets for 2013 (Table 4.2). All discharge measurement data were analyzed and then used to develop the rating curve based on a simple curve fitting method. Discharge measurements versus their corresponding water surface elevations at the SPB can be viewed in Figure 4.6. This curve can be used with the water level frequency information (Figure 4.3) to describe flow durations which have a large role in the river erosion phenomena.

Table 4.2: Supplemental discharge from Water Survey of Canada

Date (2013)	Discharge (m^3/s)	Water surface elevation at SPB (m)
Feb-21	17.8	221.86
May-01	1230	228.93
May-14	1190	228.56
June-25	298	224.94

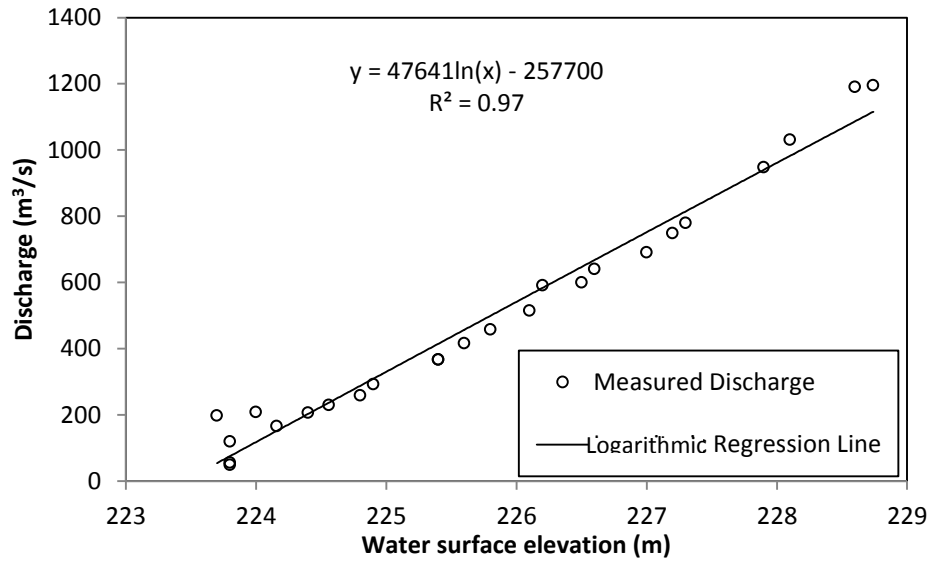


Figure 4.6: Discharge rating curve for the Red River at SPB during the study period

4.4 Velocity Distribution Analysis

Many fundamental variables and complicated processes such as hydraulic shear stress and sediment transport have been recognized to be a function of the flow velocity in rivers. The measured water velocities at each cross section were used to provide velocity frequency analysis on the basis of water level and discharge. A summary of the velocity frequency information for some measurements at the SPB is presented in Table 4.3. In this table, V_{\max} and V_{avg} are the measured maximum velocity and the mean velocity (m/s), respectively. The ratio of $\frac{V_{\max}}{V_{\text{avg}}}$ remained almost constant for different flow conditions. This dimensionless parameter can be used with Equation 4.2 to calculate the entropy parameter (M) (Chiu 1991).

$$\frac{V_{avg}}{V_{Max}} = \frac{e^M}{e^M - 1} - \frac{1}{M} \quad \text{Equation 4.2}$$

Where M is a parameter and can be determined based on a probabilistic approach and the entropy theory. Numerous authors have shown that the entropy parameter is a constant for each channel section and is not a function of the discharge or flow depth (Chiu 1991). Considerable research has resulted in established techniques to determine discharge, velocity profile and average shear stress in natural streams from the entropy parameters (Chiu and Said 1995; Moramarco et al., 2004; Ardiclioglu et al., 2007). The velocity distribution in each vertical section of a river can be simulated by Equation 4.3 (Chiu and Said 1995).

$$V = \frac{V_{max}}{M} \ln\left[1 + \left\{(e^M - 1) \frac{z}{H - h} \exp\left(1 - \frac{z}{H - h}\right)\right\}\right] \quad \text{Equation 4.3}$$

Where V_{max} is the maximum velocity in that vertical water sample, H is the water depth, z is the distance from the channel bed, and h is the distance from the water surface to the point where maximum velocity occurs. Figure 4.7 presents two measured and entropy-based calculated velocity distribution profiles at SPB for $Q = 1100 \text{ m}^3/\text{s}$ in locations A and C which were presented in Chapter 3.

Table 4.3: Average and maximum velocity under different discharge values during the study period

	Q = 1200 (m^3/s)	Q = 950 (m^3/s)	Q = 750 (m^3/s)	Q = 600 (m^3/s)	Q = 518 (m^3/s)	Q = 294 (m^3/s)	Q = 231 (m^3/s)
V_{avg} (m/s)	1.075	1.03	0.94	0.86	0.77	0.61	0.64
V_{max} (m/s)	1.36	1.32	1.2	1.1	1	0.8	0.8
$\frac{V_{max}}{V_{avg}}$	1.26	1.28	1.27	1.28	1.29	1.31	1.28

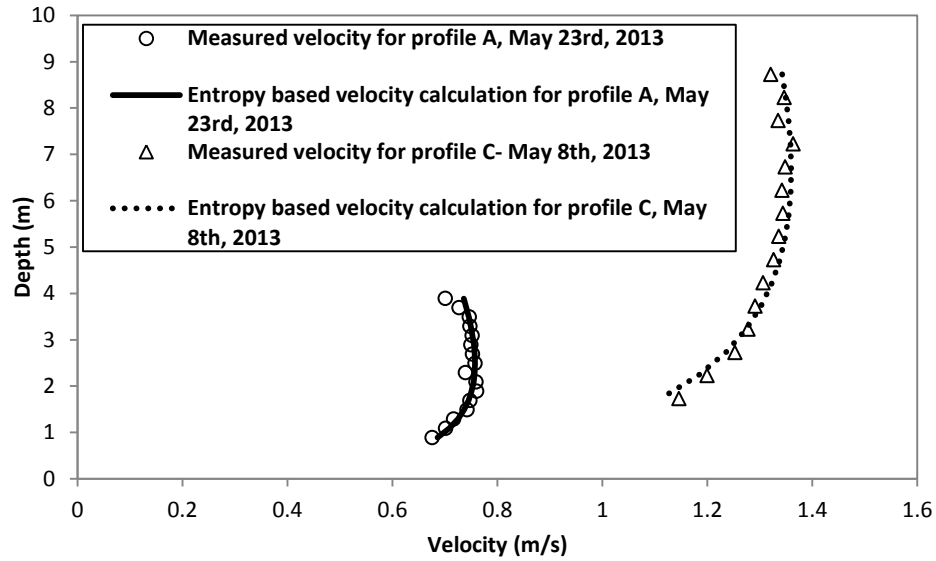


Figure 4.7: Two measured and entropy-based calculated velocity distribution profiles

The discharge and the spatial distribution of velocity were measured at 12 cross-stream transects in different locations along the reach at approximately 0.75 to 1 km intervals on July 23rd, 2013. Figure 4.8 provides an overview of the study area, including the locations of discharge measurements, and Figure 4.9 illustrates the profile of velocity magnitudes at these 12 cross sections. The ADCP velocity data were processed in Excel and MATLAB to provide cross-sectional maps of velocity distribution across the Red.

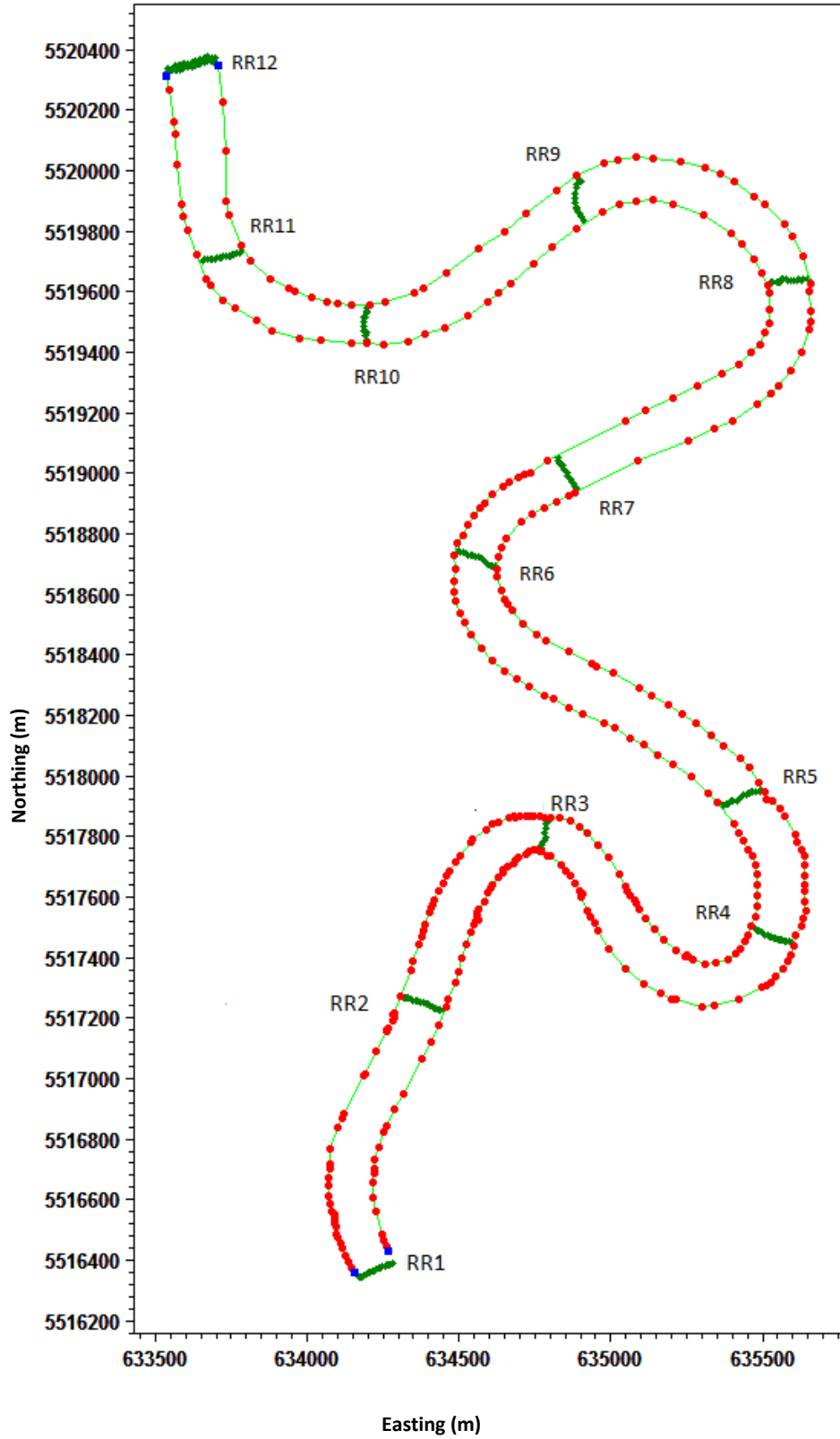
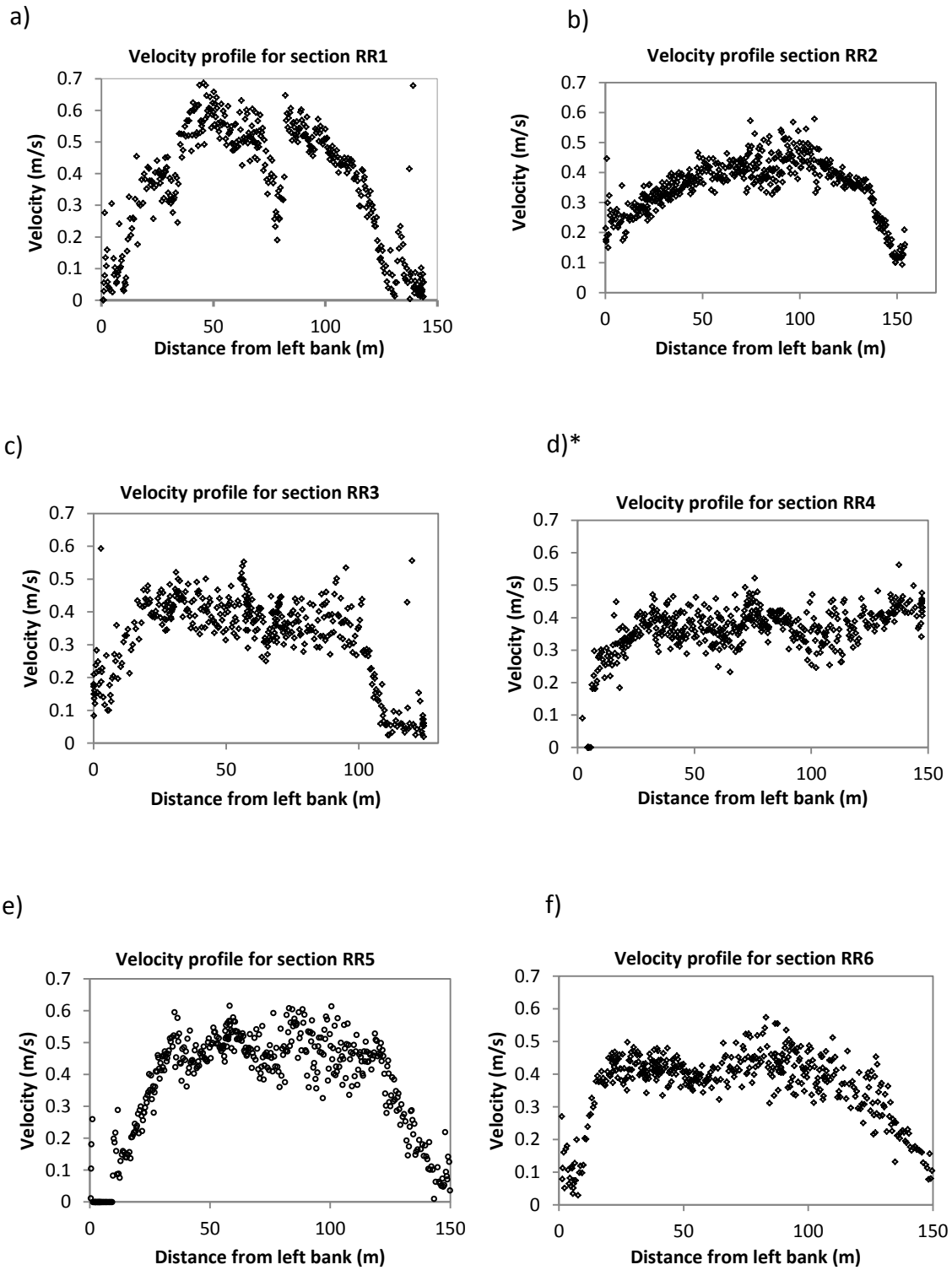


Figure 4.8: Plan view of 12 discharge measurement locations on July 23rd, 2013



* There is riprap on the right bank of this cross section; therefore, the M9 could not measure velocity near this bank.

Figure 4.9: Velocity distributions of 12 cross sections along the study reach

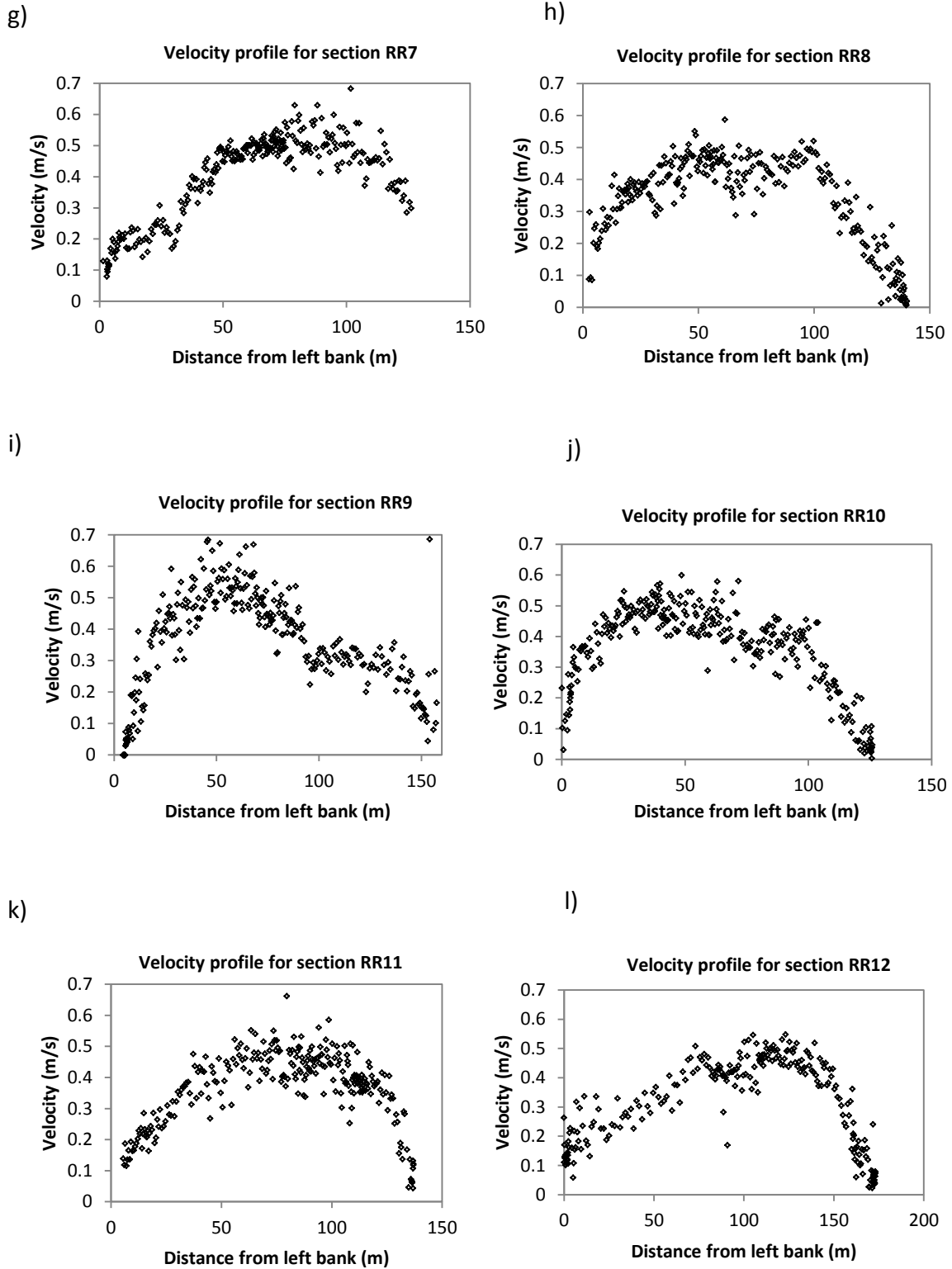


Figure 4.9 (continued): Velocity distributions of 12 cross sections along the study reach

Table 4.4 shows velocity, discharge, and some of hydraulic parameters at measured cross sections for this particular day. The Froude number ($F_r = \frac{V_{avg}}{\sqrt{g \cdot D_d}}$) is a non-dimensional number which is used to describe flow regime in open channel flow. Where g is the acceleration of gravity (m/s^2) and $D_d = \frac{A}{T}$ is hydraulic depth which T is cross sectional top width (m). During the field activity, it could be seen that there were sections where the M9 had difficulty measuring velocity and discharge. The M9 frequently lost GPS signal, especially close to University of Manitoba due to signal inference around the University (RR6 and RR7) and the discharge measurement was not reliable. The variation of hydraulic parameters (such as cross-sectional area, wetted perimeter, and hydraulic radius) along the reach enable for the estimation of boundary roughness and average shear stress at these cross sections.

Table 4.4: Summary of flow properties in the Red at different locations on July 23rd, 2013

Location	Discharge (m^3/s)	Mean velocity (m/s)	Width (m)	Hydraulic mean Depth (m)	Froude number	Reynolds number* 10^6
RR1	230	0.462	137	3.65	0.08	1.9
RR2	220	0.38	141	4.1	0.06	1.4
RR3	221	0.37	110	5	0.05	1.3
RR4	226	0.37	138	4.4	0.06	1.5
RR5	227	0.411	137	4	0.07	1.7
RR6	175	0.381	110	4.2	0.06	1.5
RR7	195	0.445	103	4.2	0.07	1.7
RR8	233	0.38	139	4.4	0.06	1.7
RR9	223	0.434	145	3.5	0.07	1.9
RR10	200	0.39	110	4.6	0.06	1.7
RR11	211	0.385	124	4.4	0.06	1.7
RR12	230	0.39	130	4.3	0.06	1.7

4.5 Calculation of Manning's n

Channel roughness and its variation have a significant impact on the river discharge capacity, the applied shear stress, and the probability of flow-induced erosion. The estimation of river roughness has been developed by many researchers and this coefficient has been presented based on different factors such as water surface slope, the median size of the bed material, and top width of stream. The analytical approach, obtained field data, and observations were used to determine global open channel resistance coefficients in terms of Manning's n, as a basis for 2D hydrodynamic modeling calibration.

In order to obtain the most reliable value for the Manning's n ($n = \frac{A \cdot S^{\frac{1}{2}} \cdot R^{\frac{2}{3}}}{Q}$), the water surface slope (S), cross sectional area (A), wetted perimeter (P) and hydraulic radius ($R = \frac{A}{P}$) over time were computed at the SPB cross section. The calculations of Manning's n and specific energy (E) for a wide range of discharges were undertaken (Table 4.5). The following equation was used to calculate specific energy.

$$E = D_d + \frac{V_{avg}^2}{2g} \quad \text{Equation 4.4}$$

A few ADCP measurements were also taken to calculate "n" at sections other than the SPB along the reach on June 11th (AO1), 12th (AO2), 13th (AO3), 14th (AO4), 18th

(AO5), 19th (AO6), 20th (AO7), and 21th (AO8), 2013, to examine the accuracy of the representative of Manning's value (Figure 4.10). Tables 4.6 and 4.7 indicate the variation of hydraulic parameters with discharge at different cross sections than the SPB. The hydraulic performance at various cross sections in the full reach showed that the average n value was 0.025 (from Manning's equation). The calculated values of " n " at the SPB and other locations indicate that Manning's n varies with space and time. Also, this coefficient can change as a result of other parameters such as river cross section shape variation, type and density of vegetation.

Table 4.5: Specific energy and Manning's n values at the SPB over time

Date (2013)	E (m)	$V_{avg}^2/2g$ (m)	n
07-May	7.065	0.060	0.025
07-May	6.825	0.056	0.025
08-May	5.789	0.057	0.026
23-May	5.893	0.056	0.024
23-May	5.974	0.055	0.024
30-May	6.110	0.051	0.025
30-May	6.110	0.046	0.026
06-Jun	6.240	0.053	0.025
06-Jun	6.049	0.054	0.025
17-Jun	4.956	0.029	0.024
17-Jun	5.044	0.028	0.025
25-Jun	4.047	0.016	0.024
25-Jun	4.023	0.015	0.026
03-Jul	5.286	0.035	0.027
03-Jul	5.267	0.034	0.025
05-Jul	5.726	0.038	0.025
05-Jul	5.328	0.036	0.026
08-Jul	5.259	0.035	0.023
08-Jul	5.402	0.036	0.023
15-Jul	3.961	0.013	0.023
15-Jul	3.941	0.013	0.023
19-Jul	3.758	0.010	0.025
19-Jul	3.602	0.010	0.023
23-Jul	3.661	0.011	0.025
30-Jul	3.362	0.008	0.024
30-Jul	3.351	0.008	0.024
07-Aug	3.148	0.005	0.026
07-Aug	3.181	0.005	0.026
07-Aug	3.369	0.004	0.027
07-Aug	3.145	0.005	0.026
04-Sep	1.881	0.003	0.025
10-Oct	1.747	0.003	0.025
12-Nov	2.986	0.005	0.023
Avg. n			0.025

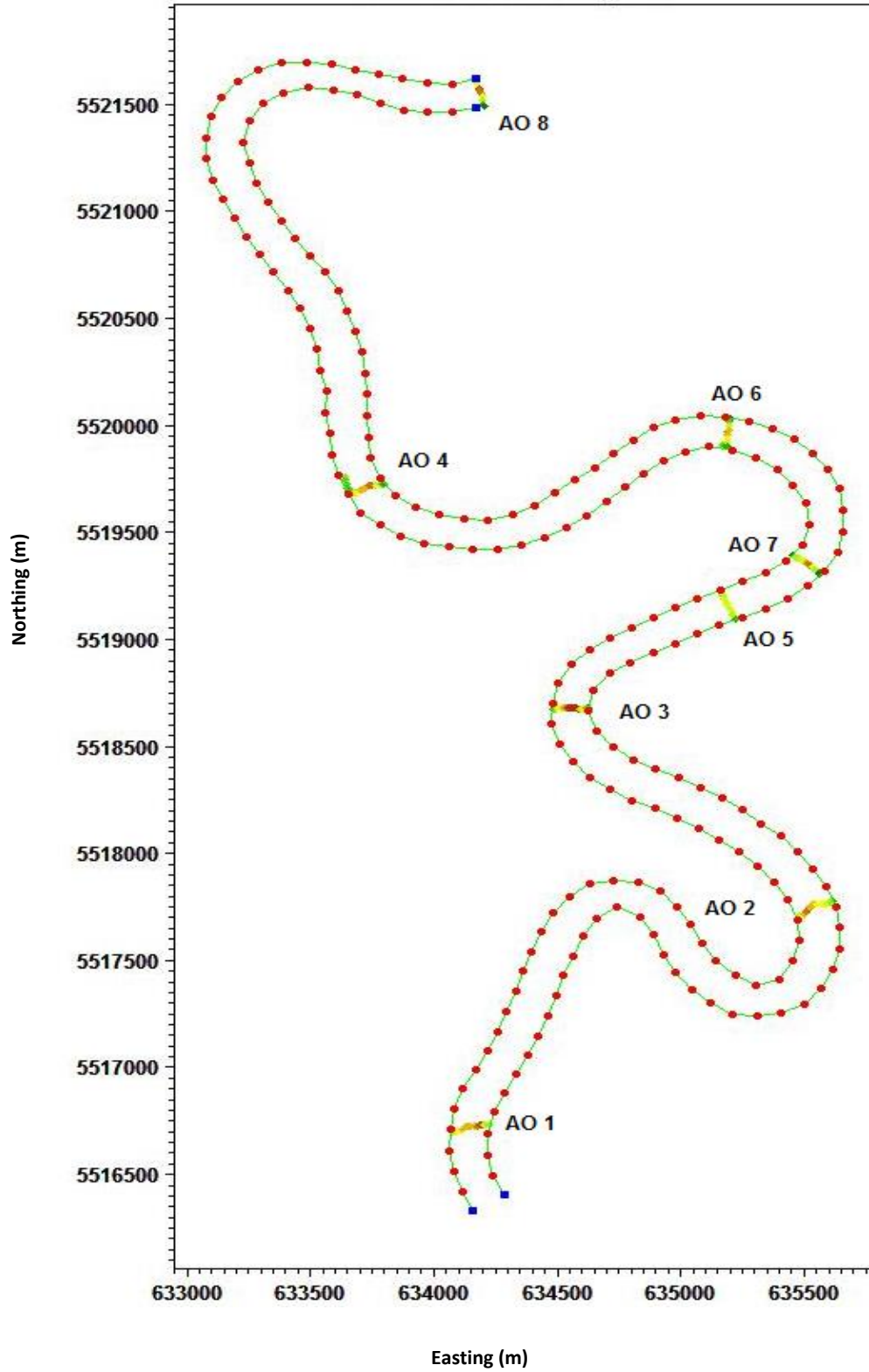


Figure 4.10: Location of discharge measurements during the bathymetry measurements

Table 4.6: Specific energy and Manning's n values at different time and locations

Date (2013)	Location	Discharge	E (m)	$V_{avg}^2/2g$ (m)	n
11-Jun	AO1	780	6.505	0.030	0.030
12-Jun	AO2	749	6.149	0.030	0.030
13-Jun	AO3	660	6.772	0.024	0.023
14-Jun	AO4	591	5.728	0.025	0.028
18-Jun	AO5	458	4.986	0.020	0.026
19-Jun	AO6	417	5.367	0.016	0.027
20-Jul	AO7	367	5.285	0.013	0.025
21-Jul	AO8	366	5.577	0.012	0.023
Avg. n					0.026

Table 4.7: Specific energy and Manning's n values on July 23rd, 2013 at different locations

Location	E (m)	$V_{avg}^2/2g$ (m)	n
RR1	3.661	0.011	0.023
RR2	4.107	0.007	0.024
RR3	5.007	0.007	0.025
RR4	4.407	0.007	0.028
RR5	4.009	0.009	0.027
RR6	4.207	0.007	0.025
RR7	4.210	0.010	0.023
RR8	4.407	0.007	0.030
RR9	3.510	0.010	0.024
RR10	4.608	0.008	0.026
RR11	4.408	0.008	0.027
RR12	4.308	0.008	0.026
Avg. n			0.025

A global open channel resistance coefficient is not only presented based on Manning's equation. Other roughness coefficients such as Darcy-Weisbach friction factor (f), and Chezy's (C_z) value can also be used. The Manning's n values can be converted to the Darcy-Weisbach friction factor (f) and Chezy's value by using equations 4.5 and 4.6, respectively.

$$f = 8g \left(\frac{n}{R^{1/6}} \right)^2 \quad \text{Equation 4.5}$$

$$C_z = \frac{R^{1/6}}{n} \quad \text{Equation 4.6}$$

4.6 Averaged Applied Shear Stress

A reach-averaged shear stress approximation was calculated assuming one-dimensional, steady flow using Equation 2.13, which is based on the consideration of momentum. In this equation the water surface slope (S) was calculated by dividing the difference between the daily averaged measured upstream and downstream water surface elevations by the flow length between the two bridges, (8670 m).

The reach-averaged shear stress was first estimated on the basis of cross section data analysis at the SPB since enough flow and geomorphology information was available. In order to facilitate the calculation of R and S for use in Equation 2.13, hydraulic radius was obtained as a function of water level using curve fitting methods. The relationship between average shear stress and water surface elevation at the SPB is shown in Figure 4.11. Estimated shear stress ranged from 0.2 to almost 4 Pa. Equation 4.7 indicates the relationship between reach-averaged shear stress and water level at SPB.

$$\tau_{\text{avg}} = 0.0714 (\text{SPB}_{\text{WSE}})^2 - 31.604 (\text{SPB}_{\text{WSE}}) + 3497.2 \quad \text{Equation 4.7}$$

The average applied shear stress along the reach was presumed equivalent to the average shear stress at the upstream (SPB cross section). In order to examine this assumption, cross-sectional geometry properties (A , P , R) along the reach were extracted from various ADCP discharge measurements during bathymetry measurements on June 11th - 14th and 18th - 21st, 2013. The average shear stresses for these cross sections were compared to the upstream average applied shear stress model seen in Figure 4.11. Moreover, 12 computed average shear stresses from different locations along the reach on July 23rd, 2013, can also be seen on the same figure. These 12 measurements indicated that the variation of average shear stress along the study reach is not significant and agree closely with the SPB reach-averaged shear stress.

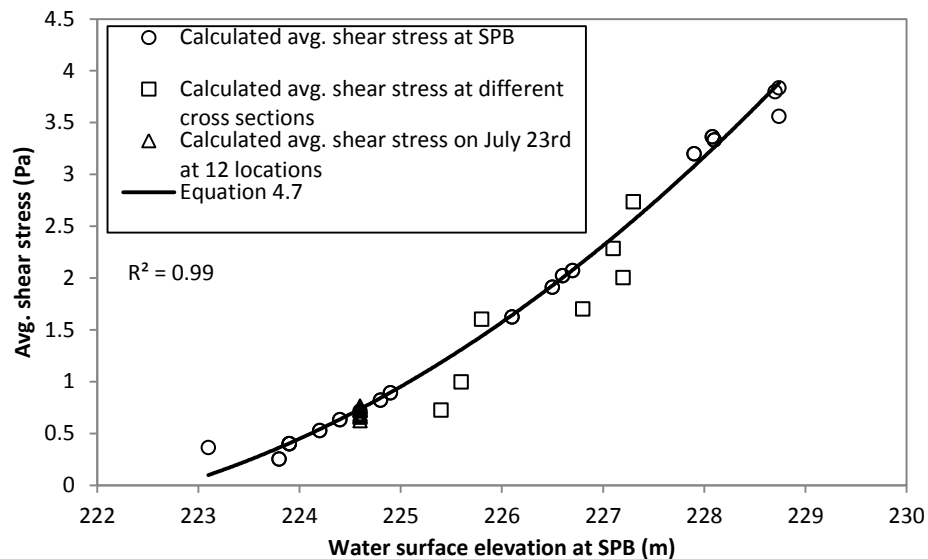


Figure 4.11: Average shear stress at SPB and other locations and dates

4.7 Local Shear Stress and Bed Roughness Estimation

In a river, erosion occurs when the applied shear stress exceeds a certain critical value. This critical shear stress is a function of river materials. Accurate estimation of near boundary shear stress is not always easy. In this part of the research, the well-known “logarithmic law” technique based on appropriate field measurement data was used to determine the local shear stress.

In order to apply the log law method to obtain shear stresses for each point of a river, stationary velocity measurements for each location were required. In this study, this was accomplished with long term fixed location velocity measurements using the Sontek M9 ADCP. These velocity profiles were collected either at the SPB site or along the study reach.

Water velocities at each location were measured for a duration of 10 minutes. In total more than 70 sets of long term velocity measurements were analysed, and most of the average turbulent velocity profiles follow a logarithmic distribution. Figure 4.12 shows five different velocity profiles at different times and at spanwise locations from the SPB.

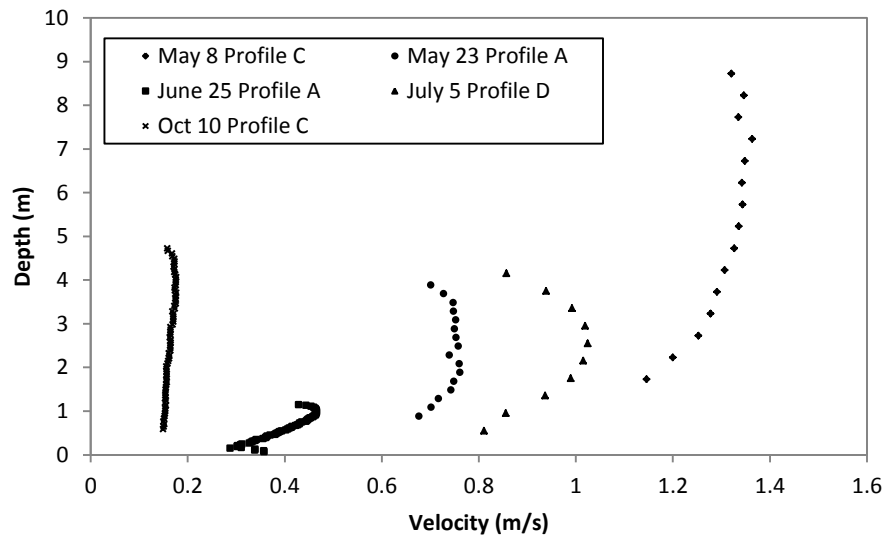


Figure 4.12: Spatial averaging of long term velocity measurement at different times and spanwise locations

The theoretical velocity was estimated from the relationship between shear velocity and flow velocity according to the following equation (Keulegan, 1938) for a fully turbulent flow and a rough bed.

$$\frac{V}{u_*} = \frac{1}{K} \ln\left(\frac{30z}{k_s}\right) \quad \text{Equation 4.8}$$

Where V is velocity in different location in each vertical water sample (m/s), u_* is shear velocity (m/s), K is von Karman constant (0.41), z is distance from the bed (m), and k_s is the local roughness height (m).

A custom built MATLAB program was used to obtain a best fit curve for each set of measured data. Since in this procedure both roughness height and shear velocity were

unknown, a trial and error approach was used to find the best fit. The slope of a least-squares line fitted to each mean velocity profile provided a measure of the shear velocity at that particular location. As an example, a logarithmic curve and the measured data from May 8th, 2013, is presented in Figure 4.13.

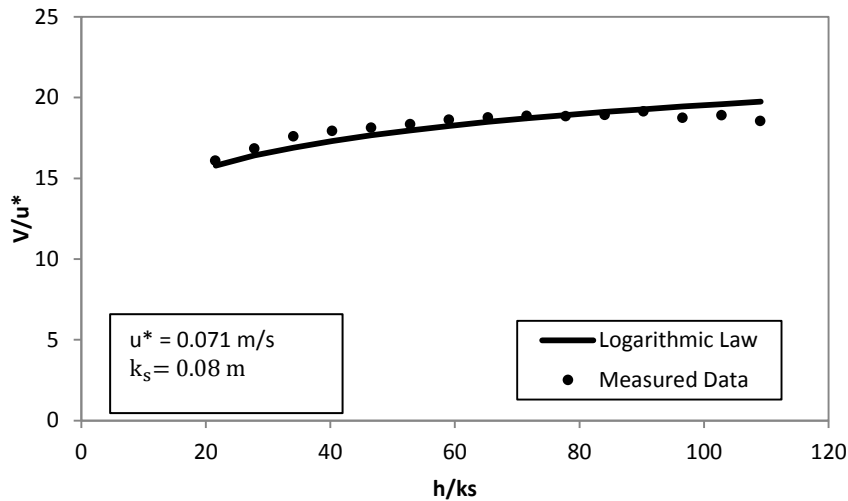


Figure 4.13: SPB Site- Location C- May 8th, 2013- channel bottom log-law fit

Equation 4.9 expresses the relationship between shear velocity and local shear stress.

$$\tau = \rho u_*^2 \quad \text{Equation 4.9}$$

Equations 4.8 and 4.9 were used to estimate bed roughness, shear velocity, and shear stress at specific locations on the river. Table 4.8 shows the local hydraulic shear stress and the average roughness height at the SPB on different dates.

Table 4.8: Local boundary shear stress and roughness height values over time

Date (2013)	Stationary measurement for shear stress estimation using log law (Pa)					Avg. roughness height (cm)
	Profile A	Profile B	Profile C	Profile D	Profile E	
08-May	---	---	5.1	---	---	---
23-May	1.8	3.2	4.4	5.8		8.4
30-May	1.8	2.2	5.1	4.4		8.1
06-Jun	1.8	2.7	3.8	5.1	4.4	6.2
17-Jun	1.4	2.2	---	---	---	---
25-Jun	1.1	1.8	1.8	1.8	*---	16.5
03-Jul	1.4	2.2	3.2	1.1	2.7	5.5
05-Jul	1.1	2.7	2.7	3.2	2.7	5.6
08-Jul	1.1	2.2	3.2	2.2	2.2	4.2
15-Jul	1.1	1.1	1.4	0.8	0.55	11.5
19-Jul	---	---	1.40	---	*---	---
30-Jul	0.81	---	1.18	---	*---	---
07-Aug	---	---	0.81	---	*---	---
04-Sep	0.08	0.09	0.20	0.1	---	13.2
10-Oct	---	---	0.23	---	---	---

*Part of the bank

Figure 4.14 compares the computed average shear stresses based on the momentum principle and the average local shear stresses at the SPB based on Equation 4.8 and 4.9 using profiles A-E. While the reach-averaged method and the local shear stress strongly agree, the local shear stresses tend to be slightly greater. This makes sense, since most local measurements were taken at locations within the cross section where the local shear stresses are expected to be greater than average.

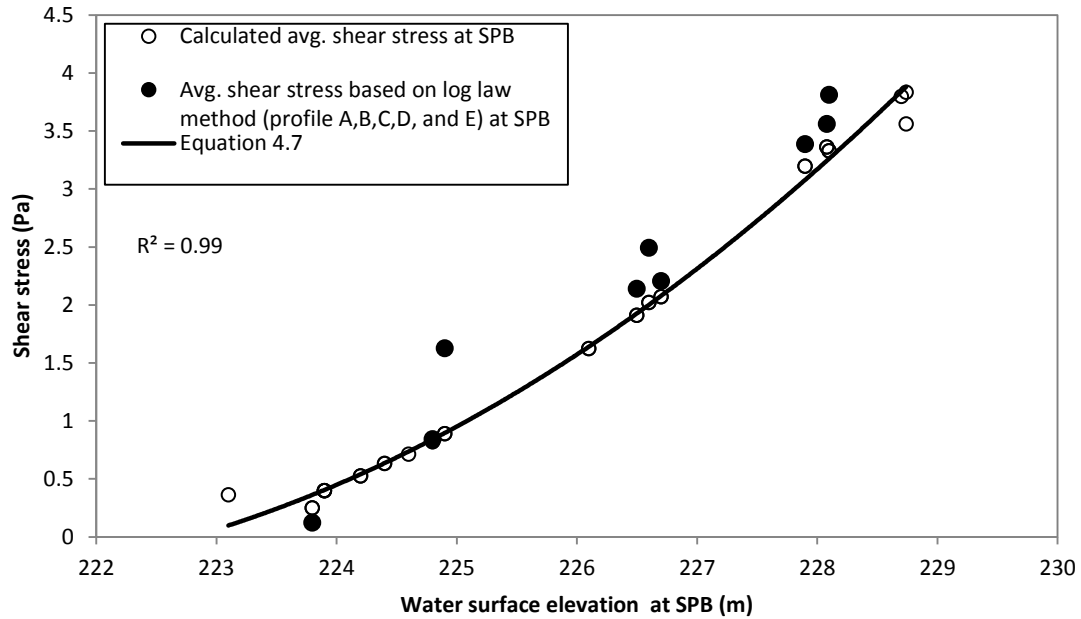


Figure 4.14: Comparing modeled average shear stress and average shear stress using log law method at SPB

4.8 Modeling Hydraulic Shear Stress Using Real Hydrometric Data

In order to further examine the accuracy of the average shear stress model, the depth and velocity data collected during the bathymetric survey was used to model the shear stress distribution. The Reynolds number and aspect ratio ($\frac{A}{T}$), indicated that the flow regime in the Red River can be considered as a turbulent flow in a wide rough open channel. This type of regime can be described by turbulent flows concept (Equation 4.10). This equation is commonly applied in 2D numerical modeling software such as MIKE 21.

$$\tau_a = \frac{1}{2} \rho f_c V_{av}^2 \quad \text{Equation 4.10}$$

V_{av} is average velocity in each profile (m/s), and f_c is current friction factor which can be obtained using Equation 4.11

$$f_c = 2 \left\{ 2.5 \left\{ \ln \left[\frac{30H}{k_{s-avg}} \right] - 1 \right\} \right\}^{-2} \quad \text{Equation 4.11}$$

where k_{s-avg} is average bed roughness height for the study reach (m). The average bed roughness height for the study reach can be estimated from the Manning's coefficient ($n = 0.025$) using the following equation (Chen 1991):

$$k_{s-avg} = \left(\frac{n}{0.038} \right)^{\frac{1}{6}} \quad \text{Equation 4.12}$$

To compute the shear stress distribution using Equations 4.10 and 4.11, depth (H), velocity (V_{av}), and bed roughness height (k_{s-avg}) are required. In conjunction with bathymetry measurement, ADCP measured mean velocity and depth at each point. Therefore shear stress was determined for each point based on real data on June 11th, June 13th, 14th, 18th, 19th, and 20th, 2013. Figure 4.15 shows the applied shear stress distribution during bathymetric measurement on June 11th, 2013, when the discharge was 780 m³/s. Average shear stresses for each were calculated and these averages had a

good agreement with the values of applied shear stress on the basis of momentum principles at the SPB (Table 4.9).

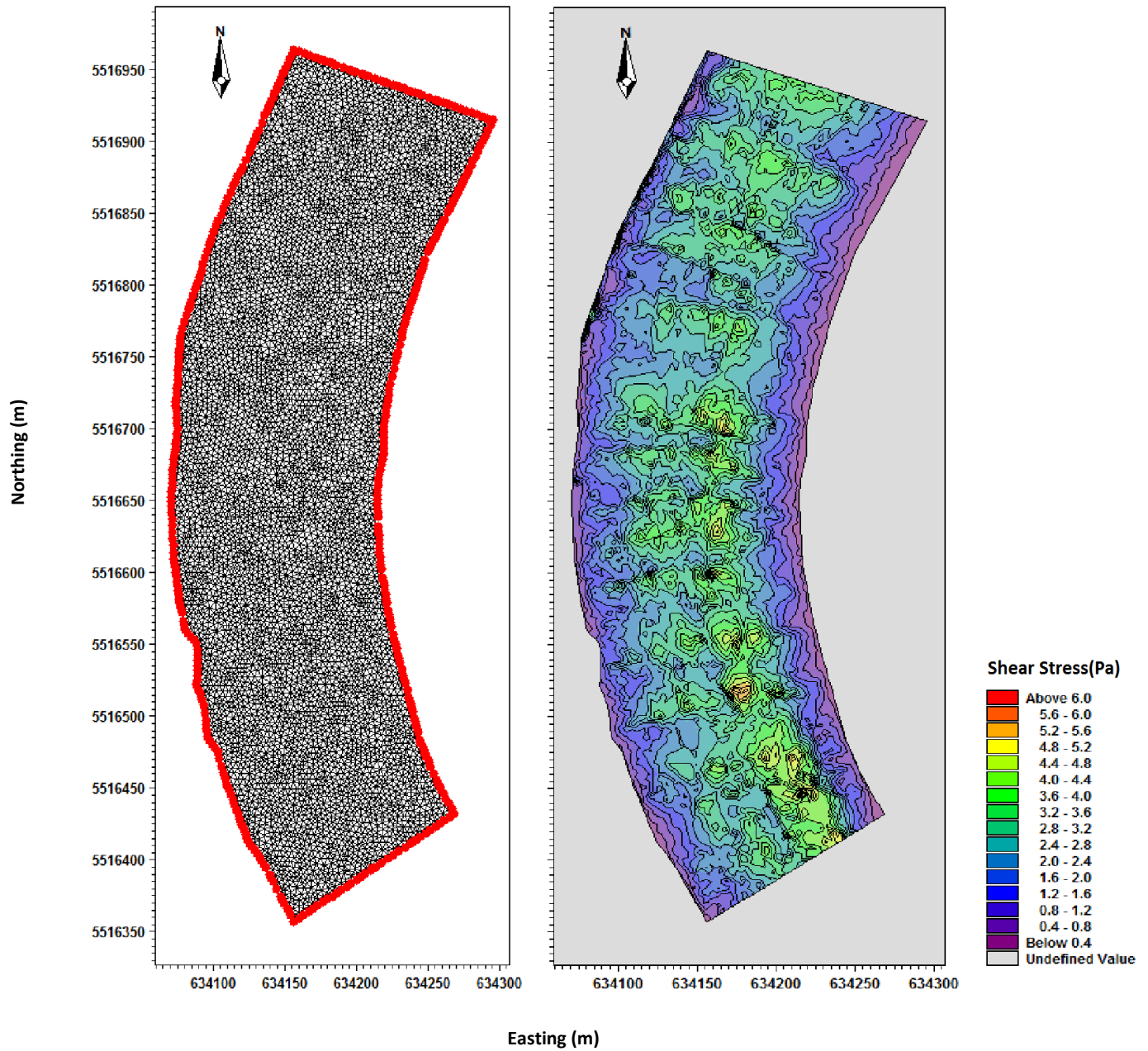


Figure 4.15: Subarea hydraulic shear stress distribution close to SPB using real measured data and a dense mesh

Table 4.9: Shear stress distribution values using measured velocity and depth of the Red River

Shear stress bin (Pa)	Frequency			
	June 11 780 (m ³ /s)	June 13 660 (m ³ /s)	June 14 591 (m ³ /s)	June 19 419 (m ³ /s)
0-1	932 (13.3%)	4782 (17.7%)	2201 (19.9%)	23171 (49.6%)
1-2	1434 (20.4%)	9662 (35.7%)	3909 (35.4%)	23043 (49.3%)
2-3	2929 (41.7%)	11478 (42.4%)	4716 (42.7%)	489 (1%)
3-4	1432 (20.4%)	1146 (4.2%)	224 (2%)	4 (0%)
4-5	271 (3.9%)	16 (0.1%)	0	0
5-6	23 (0.3%)	0	0	0
6-7	6 (0.1%)	0	0	0
Total	7027	27084	11050	46707
Avg. shear stress using turbulent flows concept	2.8	2.33	2.6	1.5
Measured Avg. shear at SPB cross section	2.9	2.34	2.3	1.32

In addition, the discharge measurement data at the SPB (mainly depth and velocity) were applied to calculate shear stress distribution across the location of the SPB using Equations 4.10 and 4.11. Average shear stress from cross sectional shear stress distribution was calculated for each day. Table 4.10 shows a comparison between average shear stress calculated by two methods: the turbulent flows concept and the momentum principle at the SPB.

Table 4.10: Shear stress distribution values on the SPB site using ADCP measurement data

Shear stress bin (Pa)	Frequency			
	May 7 1116 (m ³ /s)	May 8 1148 (m ³ /s)	May 23 1031 (m ³ /s)	May 30 969 (m ³ /s)
0-1	298 (16.5%)	251 (17.9%)	260 (25.9%)	276 (11.9%)
1-2	117 (6.5%)	116 (8.3%)	59 (5.9%)	193 (8.3%)
2-3	380 (21.1%)	300 (21.4%)	157 (15.6%)	502 (21.7%)
3-4	343 (19%)	275 (19.6%)	211 (21%)	706 (30.5%)
4-5	357 (19.8%)	237 (16.9%)	167 (16.6%)	471 (20.4%)
5-6	219 (12.1%)	165 (11.6%)	95 (9.5%)	160 (6.9%)
6-7	86 (4.8%)	58 (4.1%)	45 (4.5%)	5 (0.2%)
7-8	5 (0.3%)	3 (0.2%)	10 (1%)	0
Total Sample	1805	1405	1004	2312
Avg. shear stress (based on turbulent flows concept)	3.76	3.6	2.89	2.9
Measured Avg. shear (momentum concept)	3.6	3.8	3.33	3.19

Moreover, the shear stress distribution along the SPB cross section was calculated by using Equation 2.14.

Figure 4.16 illustrates the average applied shear stress (Equation 2.13), the shear stress distribution based on Equation 4.10, and Equation 2.14 at the SPB when the discharge was 1200 m³/s. Since the shear stress distribution calculated using the turbulent concept is a function of the water depth and velocity, the distribution using this method is more realistic than the vertical depth method (especially close to the piers as are circled in Figure 4.16).

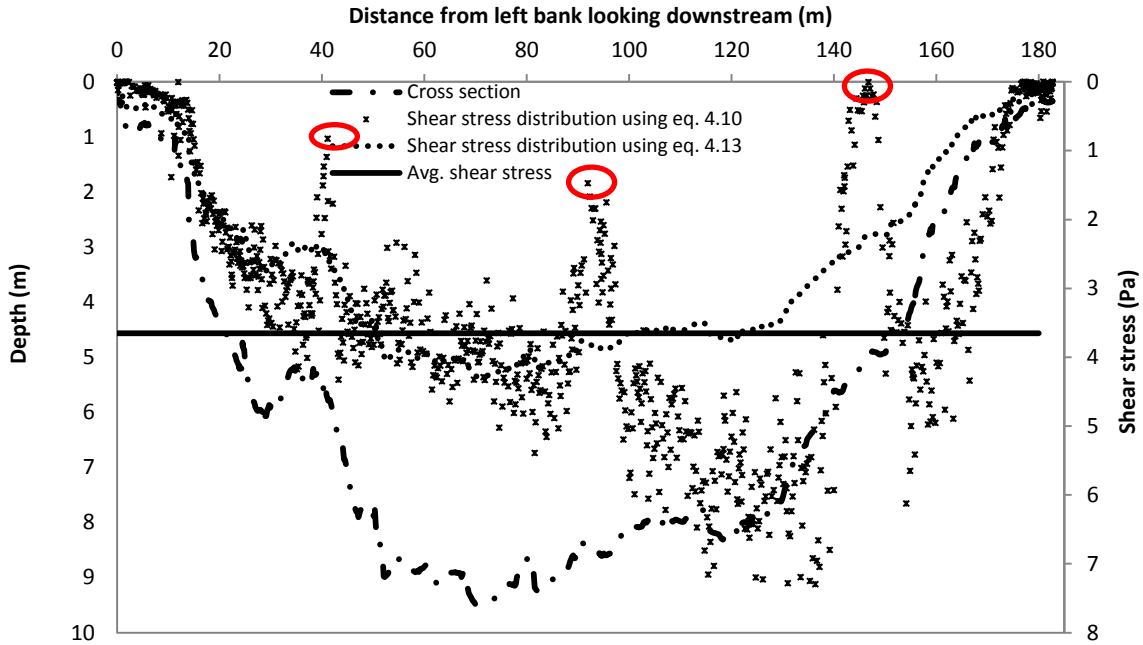


Figure 4.16: Cross sectional distribution of applied shear stress at SPB using three different methods

4.9 Numerical Modeling Results

Numerical hydraulic modeling was performed in order to predict water surface elevation changes and applied shear stresses. In this study, field data collection showed that the minimum and maximum observed discharge during the period of open water was $50 \text{ m}^3/\text{s}$ and $1200 \text{ m}^3/\text{s}$, respectively. The model was run at different flows by defining the measured discharge at the upstream end and a measured water surface elevation at the outflow. Data from the moderate flow conditions ($400 \text{ m}^3/\text{s}$ - $600 \text{ m}^3/\text{s}$) were used for model calibration. The calibration process was undertaken in order to determine whether the model results accurately reproduced the measured data during the simulation period.

Manning's roughness coefficient (n) is the most important calibration parameter in the hydrodynamic model. Therefore, this coefficient was assigned and adjusted by comparing measured water surface elevation data from upstream gauge to the simulated results and the calibrated Manning's n was determined to be 0.025, which is equal to the Manning's n obtained previously. Table 4.11 shows a comparison between the modeled and measured upstream water surface elevation for the calibration run.

Table 4.11: Comparison between measured and modeled water surface elevation at the SPB

Discharge (m^3/s)	Measured WSE (m)	Modeled WSE (m)	Difference (cm)
417	225.6	225.6	0
458	225.9	225.9	0
518	226.1	226.1	0
591	226.8	226.8	0

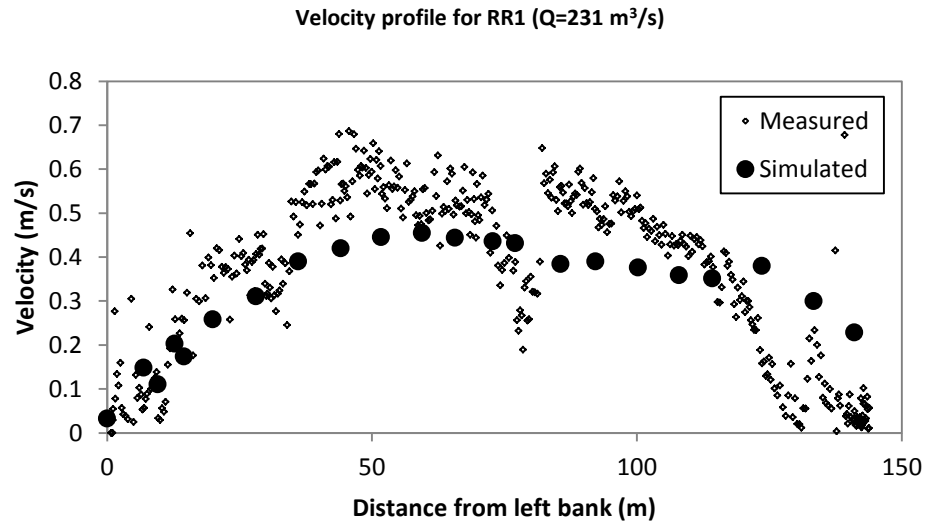
In addition, validation was carried out by comparing measured upstream water surface elevation to the modeled data through low and high flow conditions using the calibrated model (Table 4.12). The model represented the water levels accurately and this suggests that the calibrated Manning's n can be used for all flow conditions.

Table 4.12: Comparisons between measured and modeled water level at SPB for validation

Discharge (m^3/s)	Measured WSE (m)	Modeled WSE (m)	Difference (cm)
1208	228.74	228.85	11
1148	228.75	228.80	5
997	228.10	228.10	0
164	224.20	224.15	5
50	223.70	223.65	5

Furthermore, the simulated velocity profiles at different locations along the reach were extracted and compared with measured cross sectional velocity distributions to provide a check of the model accuracy. Typically, testing of the hydrodynamic model was performed for the periods that the best observed data was available within the reach. Since 12 cross section discharge and velocity measurements were obtained along the reach on July 23rd, 2013, this day was selected. Measured and modeled velocity profiles for some of these 12 cross sections are presented in Figure 4.17.a. The model underestimates the average velocity and its distribution in the RR1 cross section since in reality, water flows between the piers of the bridge and therefore the bridge affects the magnitude and shape of the velocity profile. However, in this study the bridge was not modeled.

a)



b)

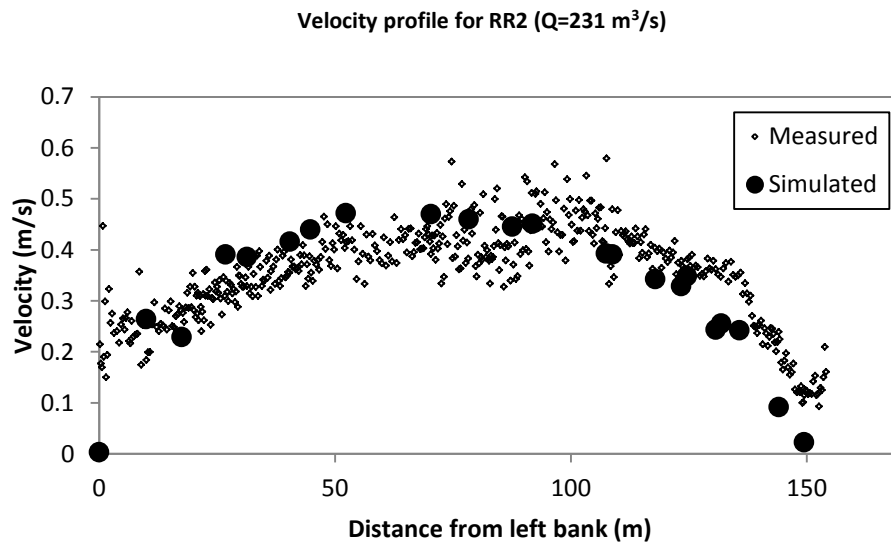
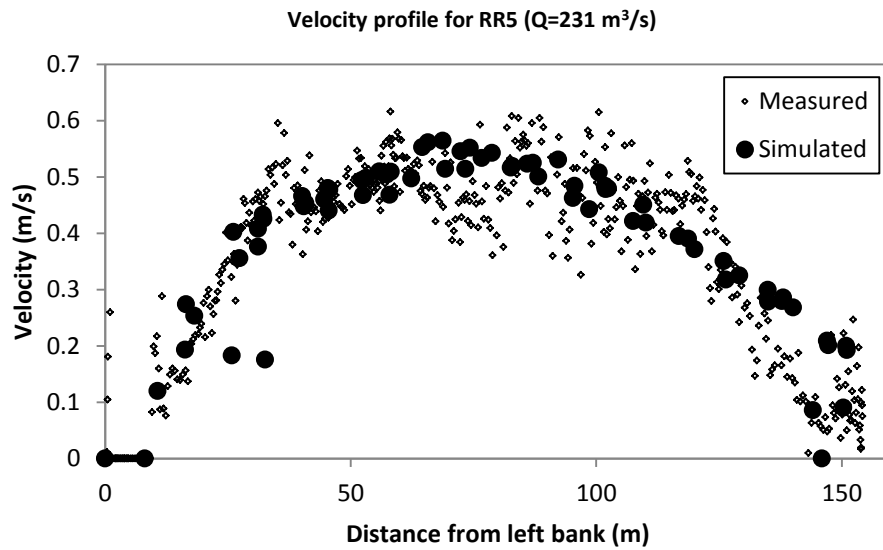


Figure 4.17: Measured and simulated velocity profiles on July 23rd, 2013, a) RR1, b) RR2

c)



d)

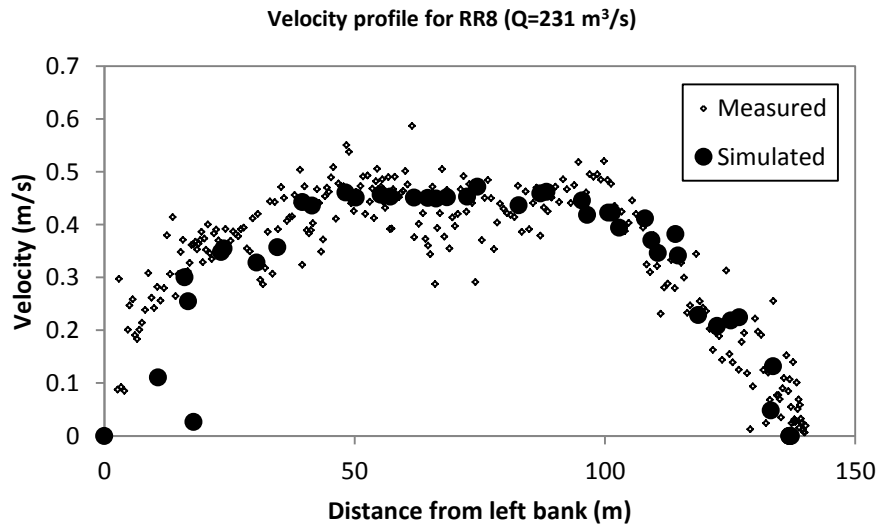
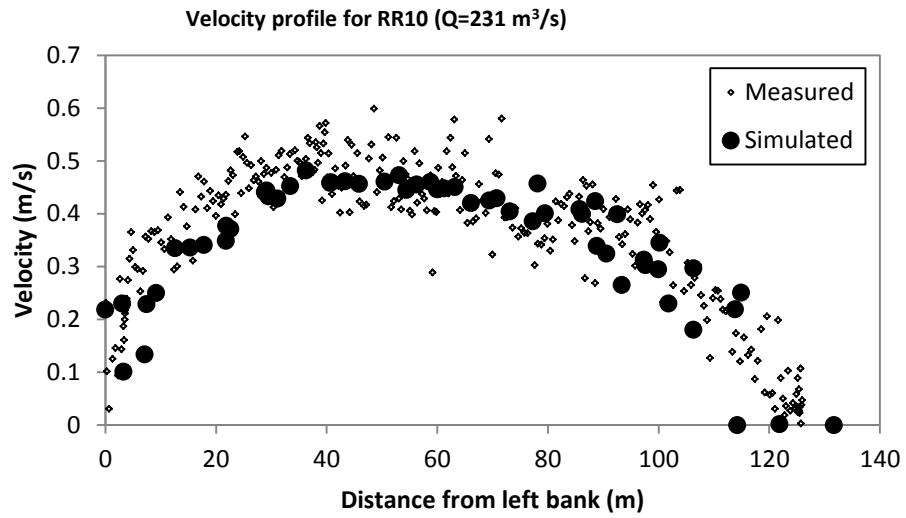


Figure 4.17 (continued): Measured and simulated velocity profiles on July 23rd, 2013, c) RR5, d) RR8

e)



f)

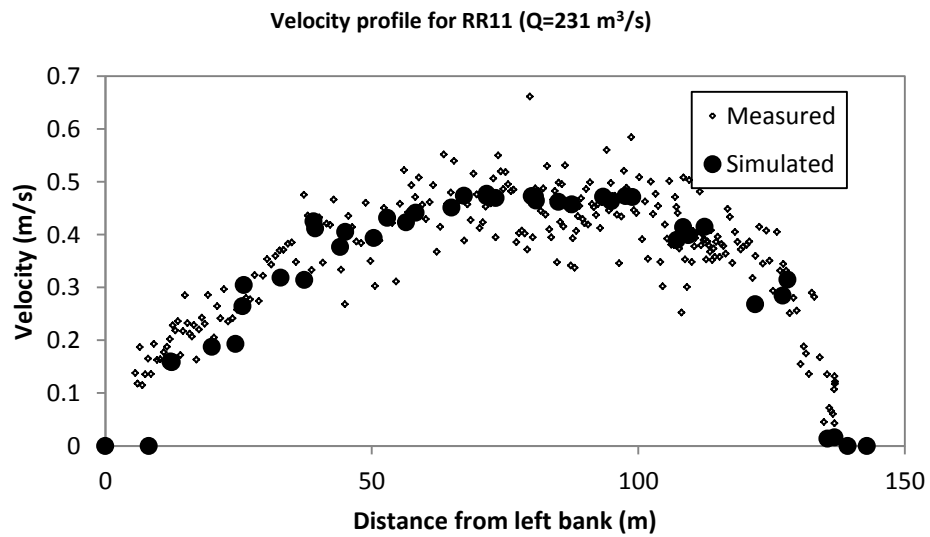


Figure 4.17 (continued): Measured and simulated velocity profiles on July 23rd, 2013, e) RR10, f) RR11

Overall, the variation in velocity is simulated well by the 2D numerical approach. It appears that even though the accuracy of a 3D numerical modeling approach may have been greater than for a 2D model, the 2D numerical model was found to predict the flow conditions on the Red River with a sufficient level of accuracy.

Moreover, simulated and measured velocities during the bathymetry measurement period were compared. The results of the comparison are presented in Table 4.13. The differences in average velocities are within 10% in all days and so it can be concluded that the model accurately simulated the average field velocities.

Table 4.13: Comparisons between measured and simulated Red River mean velocity

Discharge (m ³ /s)	Mean observed velocity (m/s)	Mean simulated velocity (m/s)	Number of observed samples	Differences (%)
780	0.78	0.74	12956	5
660	0.67	0.65	13336	3
591	0.66	0.6	19621	9
458	0.51	0.54	18337	6
417	0.58	0.52	14340	10
367	0.55	0.49	9584	11

The main objective of using the numerical model in this study was to represent the effect of moving flow on the solid boundaries under varying flow conditions. Simulated velocities and water depth from the hydrodynamic simulation, and information on roughness height were used with the Mud Transport module of MIKE 21 Flow Model FM to simulate applied shear stress in the study reach.

Since significant flow-induced erosion was assumed occurred under bank-full conditions, shear stress distribution for high flow ($1200 \text{ m}^3/\text{s}$) shown in Figure 4.18. Also, the magnitude of the simulated shear stress on the basis of high flow for each elevation is presented in Table 4.14.

Table 4.14: Applied shear stress magnitude for each elevation of the Red under bank-full condition

Red River elevation (m)	Applied shear stress (Pa)
213-214	4
214-215	4.4
215-216	4.5
216-217	4.5
217-218	4.8
218-219	4.8
219-220	4.8
220-221	4.4
221-222	3.6
222-223	2.6
223-224	1.7
224-225	1
225-226	0.7
226-227	0.8

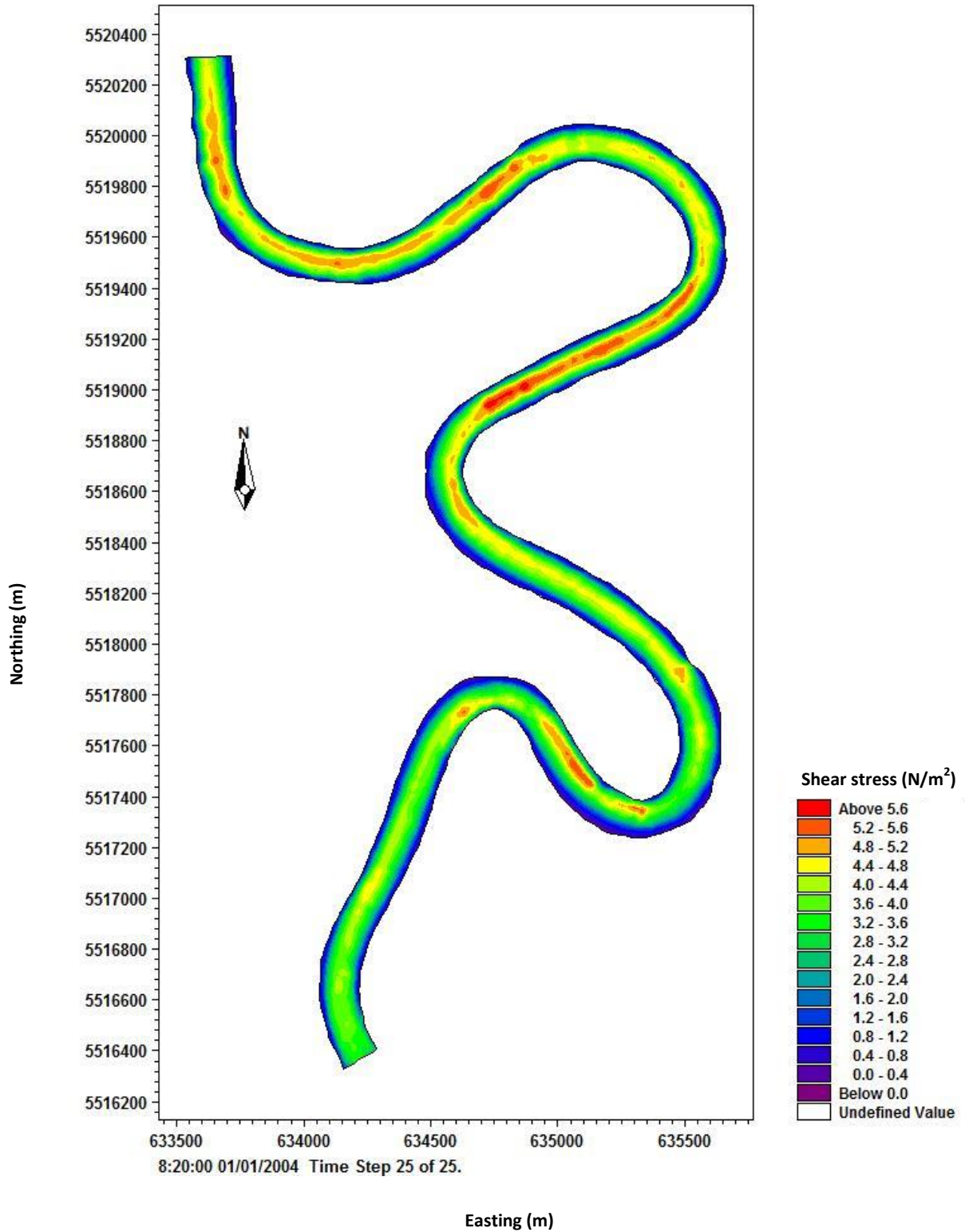


Figure 4.18: Modeled applied shear stress distribution along the study reach at maximum flow

4.10 EMD Results

As previously mentioned, seven cohesive soil and sediment samples were tested to determine erodibility and geotechnical parameters. The main goal of using the EMD was to determine the two parameters from the excess shear stress equation to estimate riverbank erosion: soil critical shear stress and soil erodibility coefficient. During the EMD test procedure, the values of shear stress were found by using Equation 3.1.

Shear stresses versus erosion rate curves were generated for all soil samples. Figure 4.19 through 4.23 present the rate of erosion versus applied shear stress as well as the linear fits to the data for samples MN3 to MN7. Although the erosion rate of samples at higher shear stress values were investigated, the range of hydraulic shear stresses which are typically occur in the Red were selected to obtain erodibility parameters (τ_c and k_d). Each sample's linear fit was utilized to determine τ_c and k_d . The slope of the best fit line is defined as the soil erodibility coefficient and the value of shear stress where the best fit line intersects x-axis is considered the critical shear stress. The results of the EMD tests are shown in Table 4.15.

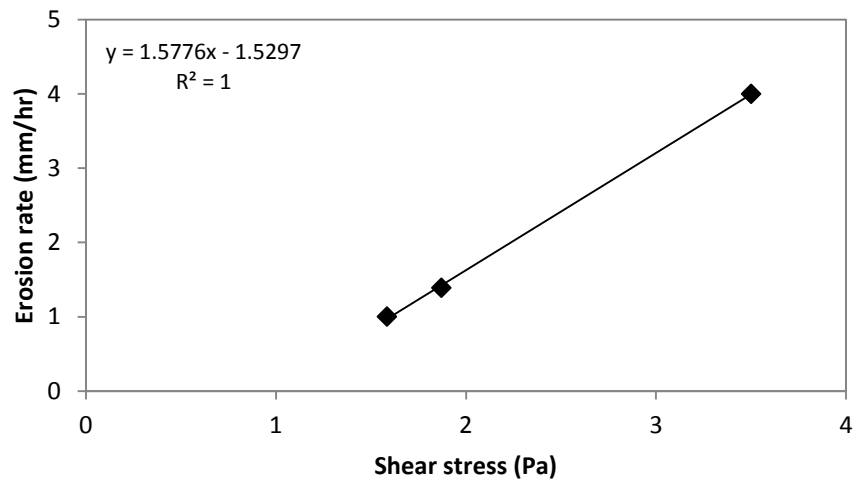


Figure 4.19: EMD test results for sample MN3

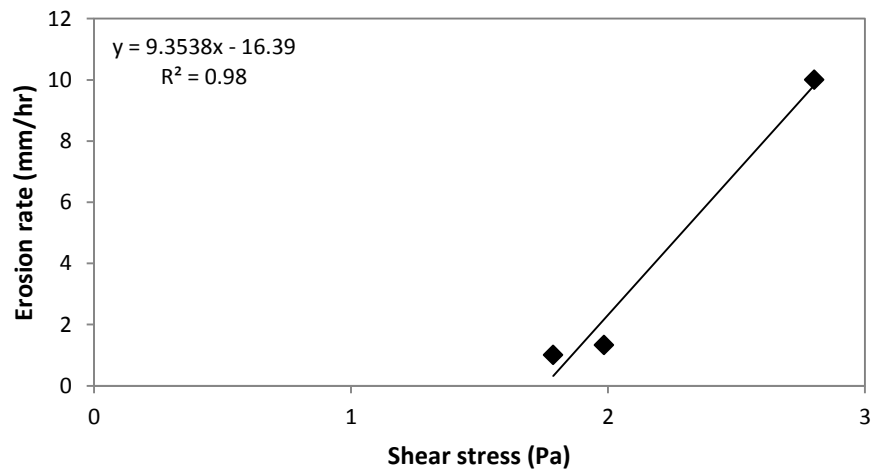


Figure 4.20: EMD test results for sample MN4

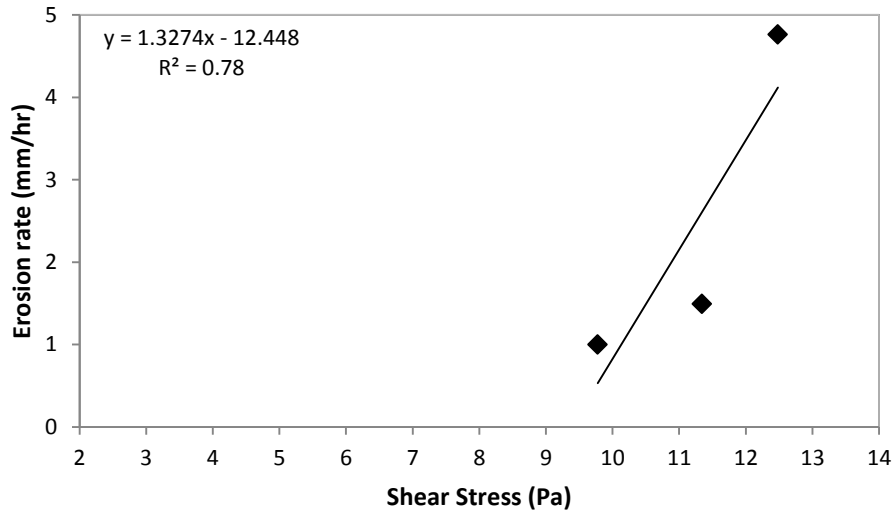


Figure 4.21: EMD test results for sample MN5

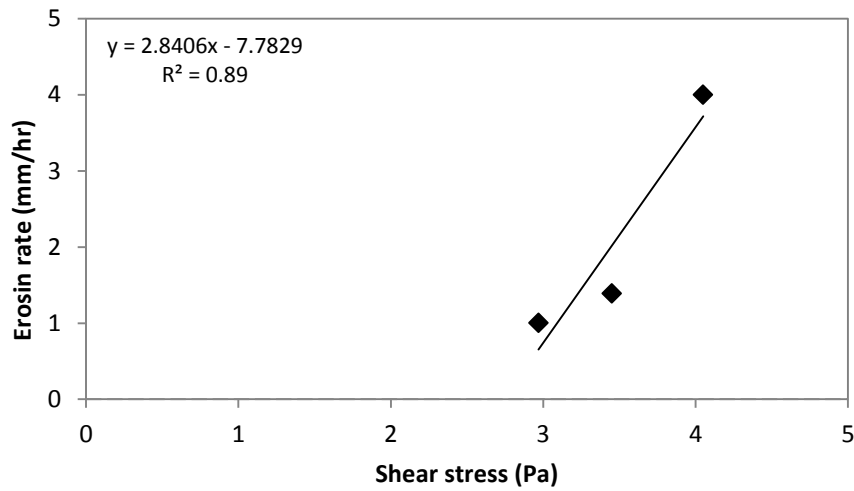


Figure 4.22: EMD test results for sample MN6

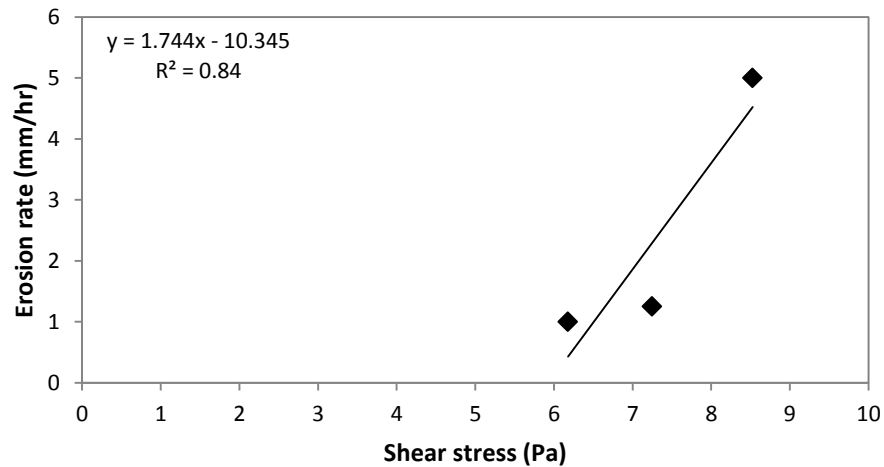


Figure 4.23: EMD test results for sample MN7

Table 4.15: EMD test results for all sites

Site location	Critical shear stress (Pa)	Erodibility coefficient
MN1	9.50	1.45
MN2	1.95	0.80
MN3	1.00	1.58
MN4	1.80	9.35
MN5	9.40	1.32
MN6	2.70	2.80
MN7	5.90	1.74

Predicted cumulative bank erosion due to applied shear stress can be determined using the excess shear stress model. The applied shear stress, soil critical shear stress, soil erodibility, and the time where the critical shear stresses of the banks were less than the applied shear stresses are the controlling factors of the erosion of cohesive soils and sediment. Results indicated that between 2012 and 2013, 187 days of river flow without

ice cover were observed. Based on the results of the frequency analysis of water surface elevation (Figure 4.3), the number of days with specific discharges were obtained.

The average applied shear stress at each flow condition is estimated using MIKE 21 in order to predict the erosion on the riverbank (Table 4.16). MIKE 21 results indicate that the average hydraulic force exerted by the flowing water at the bank surface varied between 0.1 Pa and 2.25 Pa. It should be notified that soil samples were considered representative of the bank material throughout the study site and in this computation, the effect of subaerial processes were not considered. Most of the time the applied shear stress was less than the soil's critical shear stress for all sites and therefore instead of bank erosion, the amount of deposition which may occur due to suspended load could be significant (Kimiaghalam et al., 2015b).

Table 4.16: Duration of discharge and average applied shear stress on the Red River bank

Number of days	Discharge range (m ³ /s)	Average applied shear stress on the riverbanks (Pa)
47	100	0.10
29	200	0.40
17	300	0.70
17	400	0.95
10	500	1.15
11	600	1.55
7	700	1.75
4	800	1.90
6	900	1.95
8	1000	2.05
7	1100	2.15
6	1200	2.25

The discharge frequency and erosion parameters can determine the erosion rate for each location. Based on Table 4.15 and Table 4.16, no erosion is predicted for MN1, MN5, MN6, and MN7 since critical shear stresses are greater than any applied shear stress on the riverbank. The annual erosion rate for MN2 was negligible (0.7 mm) (Kimiaghalam et al., 2015b). Annual erosion loss from the EMD test results for MN3 and MN4 are shown in Table 4.17. The net fluvial erosion was estimated without considering the amount of deposition for each site. However, in reality the ability of the Red to transport and deposit sediment should also be considered.

Table 4.17: Results of cumulative erosion rate for MN3 and MN4 locations

Site location	Critical shear stress (Pa)	Erodibility coefficient	Cumulative erosion rate (m)
MN3	1.0	1.58	1.70
MN4	1.8	9.35	1.80

4.11 Soil Part Results

For the soil samples, basic geotechnical laboratory tests were performed to study the soil properties. The samples in locations of the study reach were very similar and had close to the same chemical and physical properties. Figures 4.24, 4.25 and 4.26 show the grain size distribution for samples MN1, MN3, and MN7. More than 10 percent of the soil from all samples passed the number 200 sieve and had high plasticity index values (greater than 10) and therefore classified in the silt and clay family. Table 4.18 shows the measured properties for all samples including: median size of particles (d_{50}), percentage of clay, silt, and sand particles.

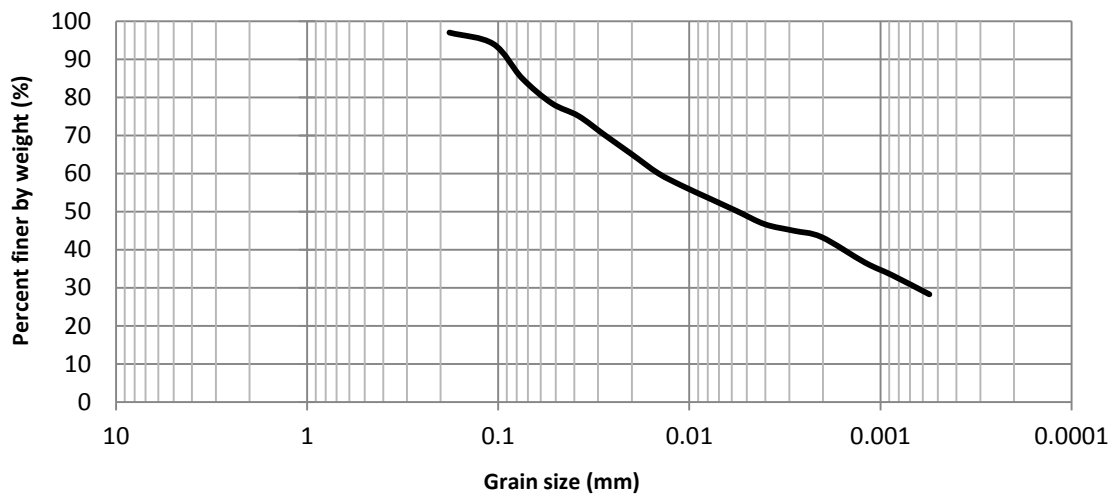


Figure 4.24: Grain size analysis of MN1

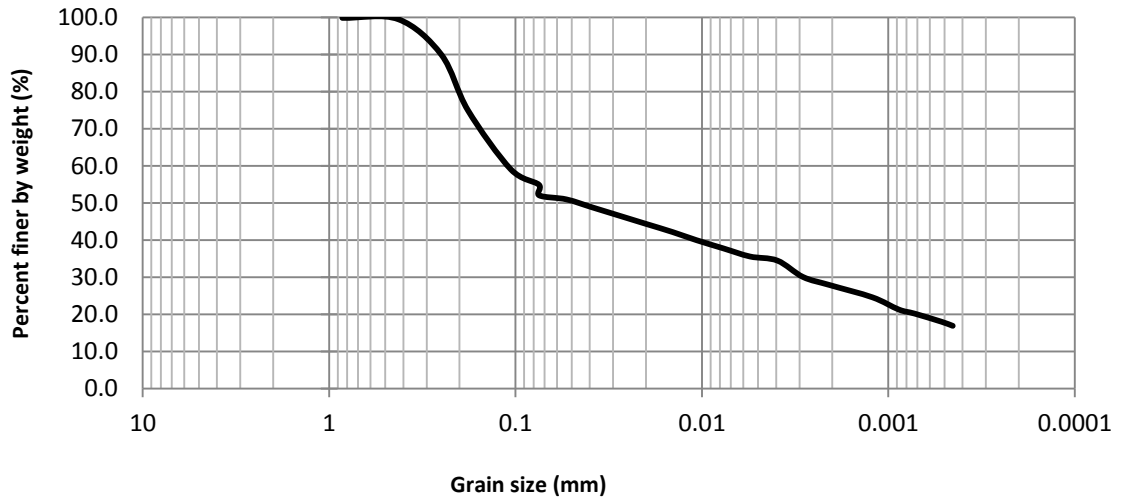


Figure 4.25: Grain size analysis of MN3

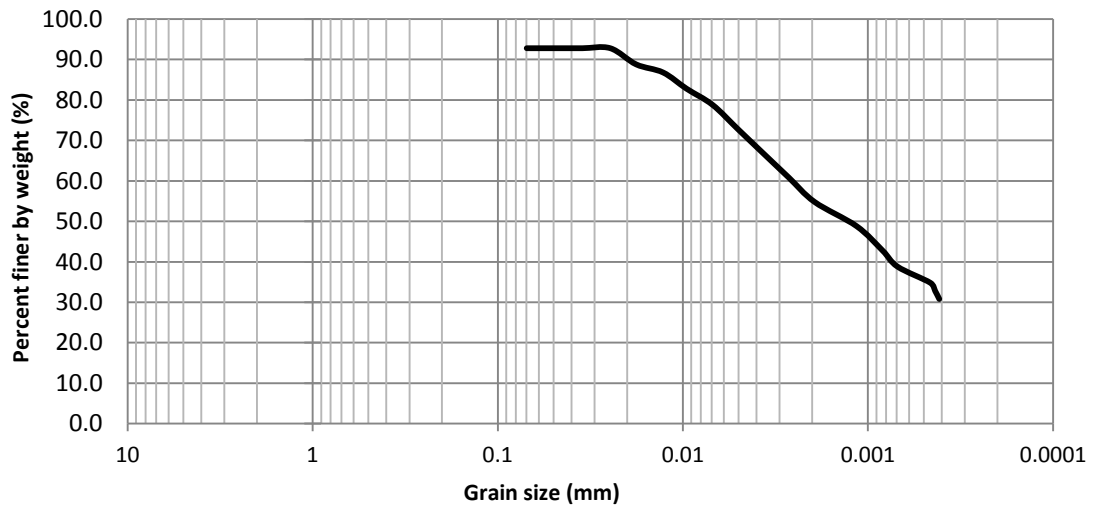


Figure 4.26: Grain size analysis of MN7

Table 4.18: Soil properties of the Red River bank

Sample ID	d ₅₀ (mm)	Clay %	Silt %	Sand %	W %	CEC (meq/100g)	EC (dS/cm)	OM (%)	SAR	PI %	ρ _{dry} (kg/m ³)
MN1	0.0056	45	40	15	44	31.29	0.855	9	0.92	34	1209
MN2	0.0081	40	35	25	54	30.28	0.888	6.6	1.16	40	1133
MN3	0.052	22	33	45	29	17.2	0.352	1	0.89	12	1415
MN4	0.0013	45	50	5	45	28.7	0.674	2.9	0.88	30	1180
MN5	0.0016	45	51	4	39	30.7	0.72	2.2	0.992	29	1312
MN6	.0017	40	55	5	40	26.6	0.764	3	0.832	25	1250
MN7	0.0013	45	47	8	35	30.3	0.726	3.3	0.893	27	1235

The empirical estimate of critical shear stress based on physical, mechanical, and electrochemical properties of cohesive soils for the Red River was discussed in Kimiaghalam et al. (2015a). They combined the basic geotechnical test results with the EMD test results to determine relations that can predict the erodibility parameters. In their study, stepwise regression analysis was used to relate geotechnical properties and soil erosion parameters. They found that among different physical, mechanical, and electrochemical soil properties, soil cohesion was the best predictor of critical shear stress and sodium adsorption ratio (SAR) had a large effect on erosion rate.

4.12 Studying Red River Erosion and Deposition Mechanisms

Using the Characterization of Particles in Suspension

The literature shows that bank erosion may have a significant contribution towards the sediment load of a river (Rinaldi and Darby, 2008). Any type of bank widening (subaerial processes, fluvial erosion, and bank failure) may be able to provide a mechanism to increase total suspended solids along the river. For a better understanding of bank erosion, different aspects of suspended sediment were investigated such as: the rates and patterns of TSS at depth and laterally along the Red, and also its grain size distributions (GSD).

In this study, a water sampling program was undertaken to determine the suspended sediment behavior. In addition, the suspended sediment transport pattern was used as a means to estimate the associated erosion and deposition amount over time in the reach. All water-sediment sampling and lab testing activities related to these samples are shown in Figure 4.27. This data collection will produce a basis for future studies and modeling sediment transport to assess the erosional and depositional patterns of soil and sediments in the Red.

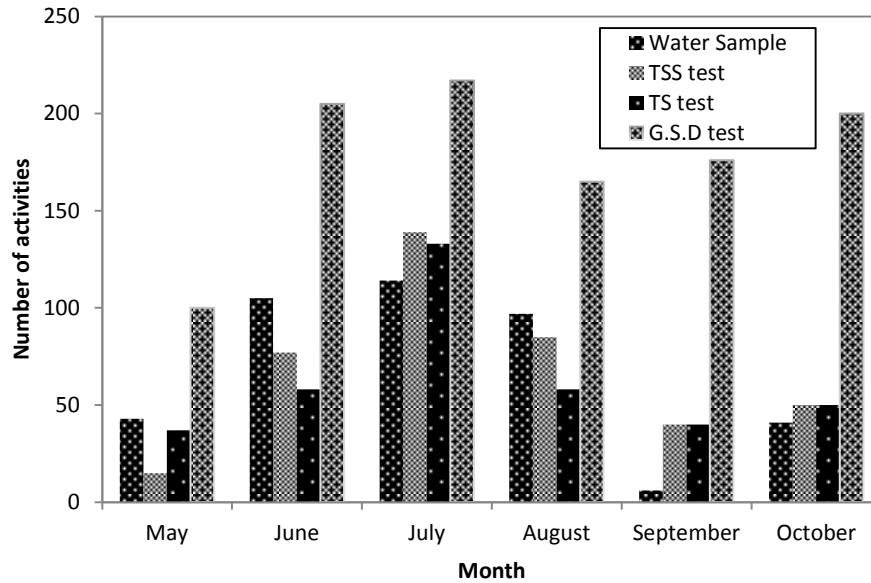
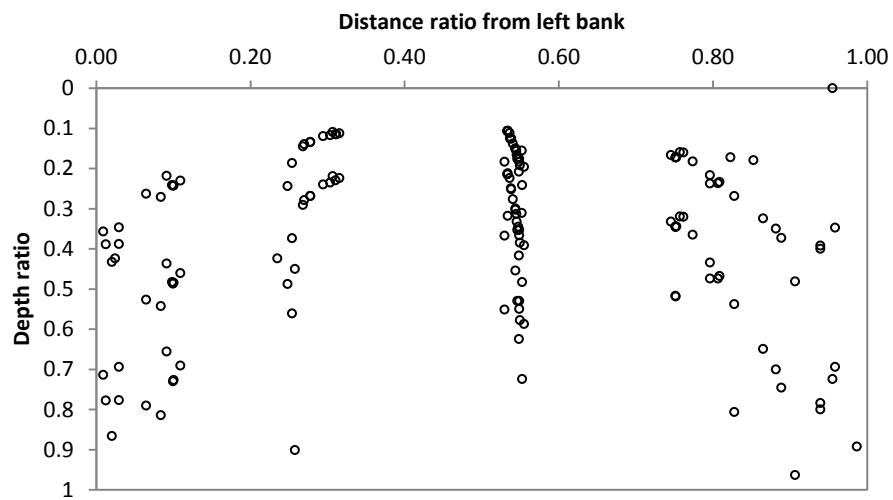


Figure 4.27: Number of different activities related to water-sediment study over time, monthly basis

4.12.1 TSS Distribution in the Red River

Water samples were collected more frequently at the reach extents during the study period. Figure 4.28 shows the water-sediment sample locations for the entire study duration at the SPB and FGB. The x axis indicates the sample distance ratio from left bank looking downstream, and the y axis presents the sample depth ratio from the water surface for that specific location. The vertical stations along the test cross sections were chosen to capture the variation of TSS in the water column and spanwise direction. In each vertical sampling location, the average TSS taken at different depths was considered as the average TSS at that sampling location. TSS averages were then averaged over all locations across the test cross section to obtain an average TSS for each cross section.

(a)



(b)

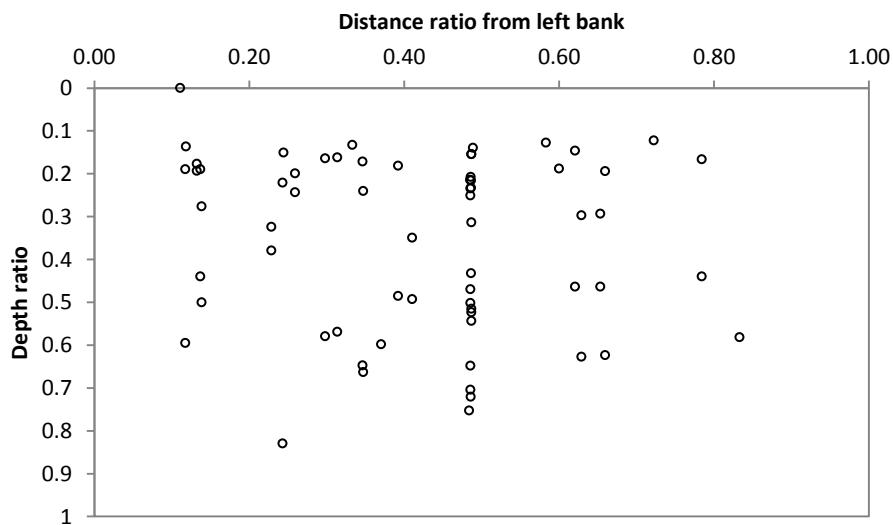


Figure 4.28: Water sampling locations at (a) SPB and (b) FGB

The mean total suspended sediment distribution in the spanwise direction at the SPB before July 5th, 2013, is presented in Figure 4.29. This figure indicates that in one particular day there was no significant variation in the mean suspended sediment load in the lateral direction. In other words, TSS was the same in the water body at the SPB, and the TSS amount was not different from one point to another. Therefore, in order to explain the spanwise TSS distribution, selecting one vertical profile (preferably middle of the river) would be sufficient. After July 3rd, samples were collected just from the middle of the Red due to this conclusion.

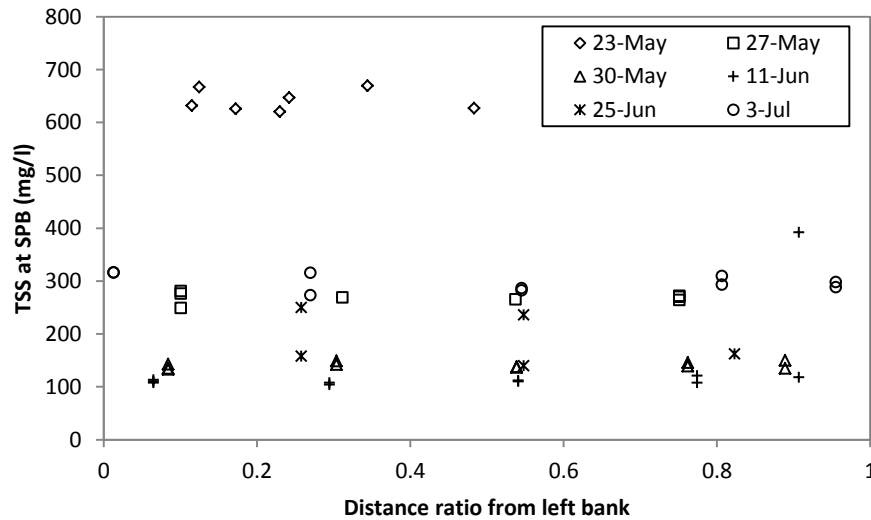


Figure 4.29: Lateral total suspended sediment distribution at SPB

The measured TSS data from the upstream and downstream reach extents, along with the corresponding discharge at each time interval throughout the study period were used to develop a suspended sediment flux rating curve. The incoming and outgoing total suspended solid load and associated discharge values for the reach are plotted

versus time in Figure 4.30. Three different zones are distinguishable in this figure. Comparing the sediment fluxes at these two locations reveals that the magnitude of suspended sediment fluxes at the SPB and FGB are relatively similar for discharges between $1000 \text{ m}^3/\text{s}$ and $300 \text{ m}^3/\text{s}$. It appears that an approximate threshold for significant deposition in the reach may be $300 \text{ m}^3/\text{s}$. An approximate steady state suspended sediment flux was reached again when discharge was $50 \text{ m}^3/\text{s}$ and again a condition of equilibrium in suspended sediment transport for the Red River could be observed.

At discharge values between $1000 \text{ m}^3/\text{s}$ and $300 \text{ m}^3/\text{s}$, probably turbulence caused the particles to have a tendency to stay in suspension and we observed the same TSS at both sites. This could indicate that in this period, the net erosion transformed by the flow is almost equal to the net deposition of sediment, in other words this phase shows the dynamic equilibrium conditions along the reach. However, during the first phase with lower discharges (between $300 \text{ m}^3/\text{s}$ and $50 \text{ m}^3/\text{s}$) the TSS at the F.G.B cross section was lower than the SPB. In this case, due to the discharge getting lower, sediment transported downstream comes out of suspension at low energy conditions and accumulates on the bed and banks. Since the water body's ability to transport suspended sediment along the river decreased, it can be concluded that the net erosion is likely less than the net deposition.

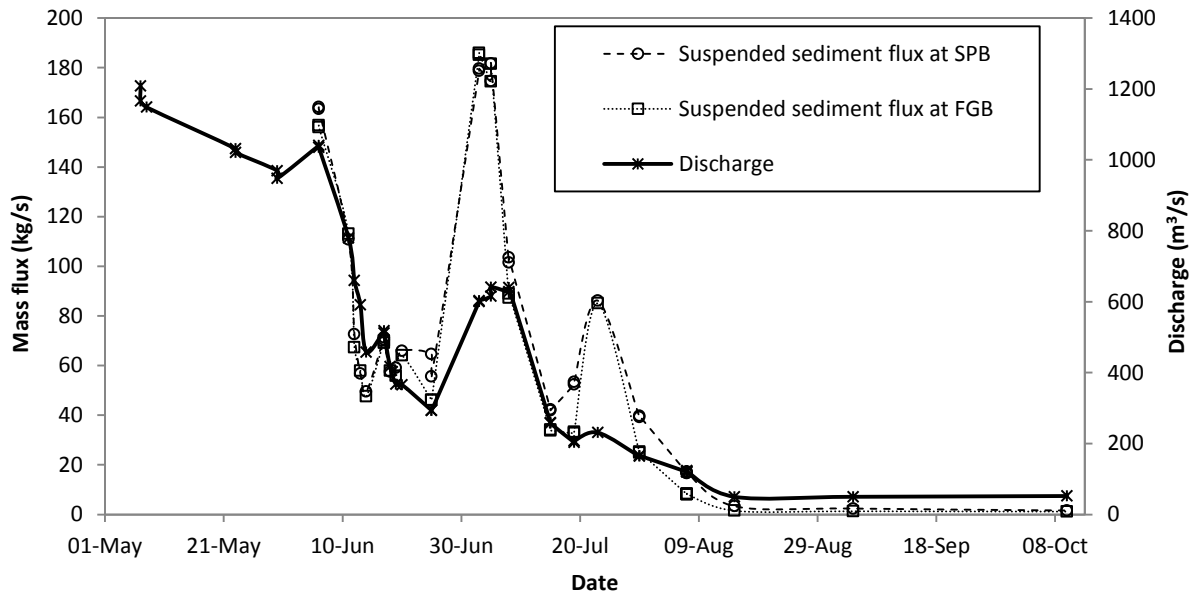


Figure 4.30: Total suspended sediment flux rating curve

In the second phase of the low flow ($Q < 50 \text{ m}^3/\text{s}$), TSS concentration does not vary between the reach extents and the less suspended availability is the result of this dynamic equilibrium. In this case, perhaps the likelihood of erosion and deposition is negligible.

To further examine erosional and depositional patterns along the Red, on June 12th, Aug 15th and, Oct 10th, 2013, the variation of TSS with distance towards the downstream was determined at 1 km intervals over a total length of 20 km which is explained in detail in section 3.2.5. The reference point is given as the first sample location, which is located at the Winnipeg floodway. TSS profiles for the middle of the river for each location were obtained by taking at least two samples from 1 meter below the water surface and as

close as possible to the bed based on ADCP depth measurements. The values of vertical TSS for each location were approximated by taking an average of the samples.

The longitudinal variations of TSS versus distance ratio for these three days (June 12th, Aug 15th, and Oct 10th, 2013) for 20 km along the Red River are plotted in Figure 4.31. Distances are positive in the downstream direction. The main difference between these groups of TSS results is the trend of TSS distribution with distance.

On Aug 15th ($Q = 100 \text{ m}^3/\text{s}$) flow could not transport all of the suspension materials along the river and it is suspected that the suspended solids were gradually deposited before the flow reached downstream. On the other hand on June 12th, and October 10th, the gradient of suspended sediment along the river was not proportional to the distance between water sample locations and TSS distribution was approximately uniform. On June 12th ($Q = 780 \text{ m}^3/\text{s}$) the hydraulic shear stresses on the river generally stayed below the level required for erosion, and the net of erosion and deposition was almost equal.

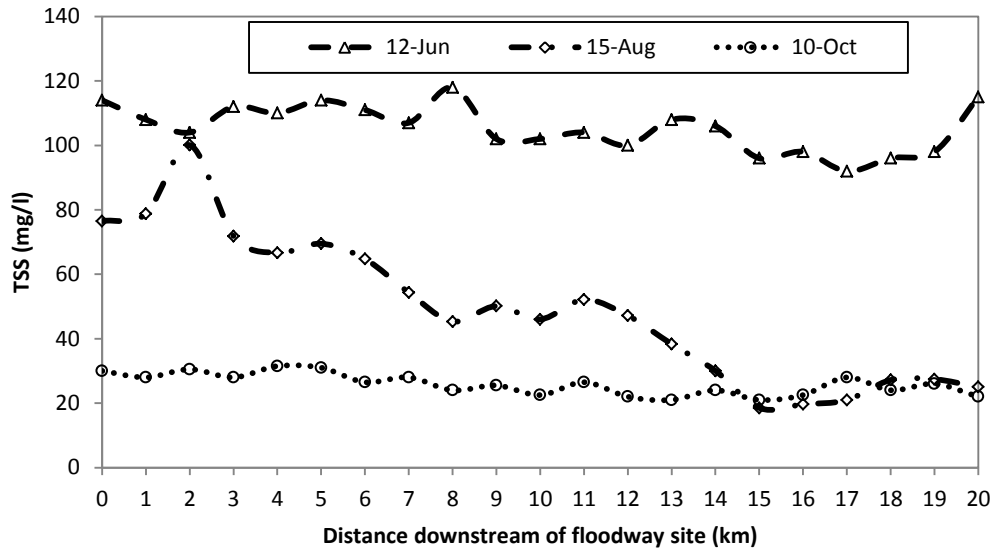


Figure 4.31: Longitudinal variation of TSS versus distance ratio along 20 km of the Red

4.12.2 Grain Size Distribution (GSD)

Grain size distribution of water-sediment can give insight to the energy of flow, dominant mode of sediment transport, and in-stream source of sediment along rivers. As previously indicated, the determination of particle sizes in suspension for all water-sediment samples was carried out by using a Malvern Mastersizer 2000 particle size analyzer.

The results of the suspended sediment size distribution test at the SPB indicated that the lateral and the vertical grain sizes of suspended solid was uniform and consisted of clay and silt ranging from 1.1 to 6.2 μm with a median grain size of 2 μm ($\sigma = 0.15 \mu\text{m}$) (Figure 4.32). Since the fall velocity for clay and silt is extremely small, turbulence will cause the particles to have a tendency to stay in suspension.

The suspended sediment size distributions at the two bridges were compared and are shown in Figure 4.33. This figure shows that the suspended sediment grain size at these two bridges does not significantly change and the GSD at the FGB over the study time was also uniform.

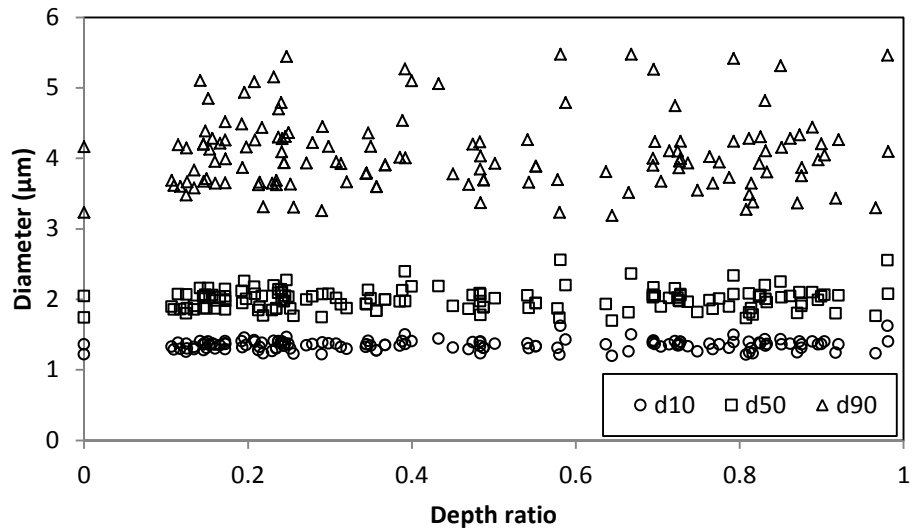


figure 4.32: d_{10} , d_{50} , and d_{90} grain sizes for SPB water samples

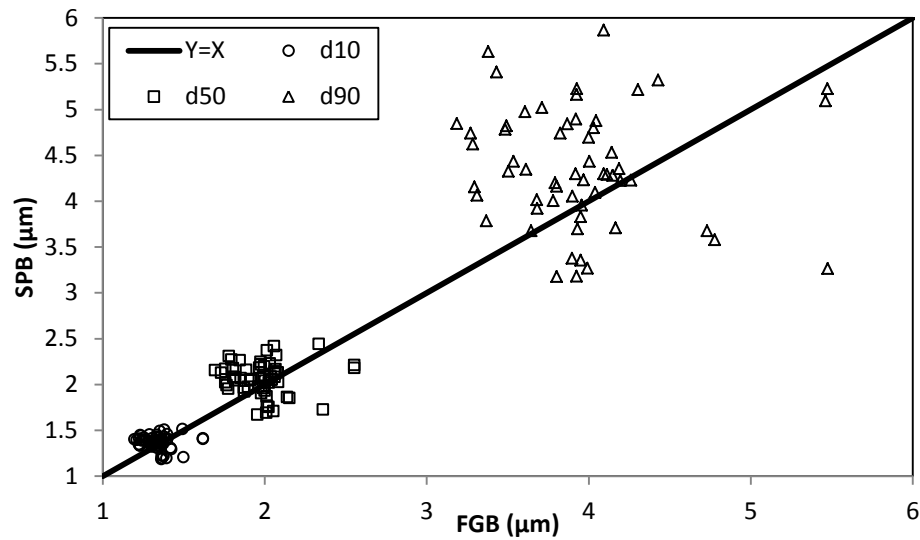


Figure 4.33: Comparing d_{10} , d_{50} , and d_{90} grain sizes at SPB Vs. FGB

The grain size distribution results of suspended solids along the 20 km of the Red River were studied separately. The reach-representative suspended sediment size distribution for 20 km of the Red also did not significantly change in space and time ($\mu = 2 \mu\text{m}$; $\sigma = 0.1 \mu\text{m}$) (Figure 4.34).

Figure 4.35 indicates the mean of d_{10} , d_{50} , and d_{90} for each discharge measurement during the study period. Therefore, it can be concluded that the suspended sediment grain size did not vary with time, discharge, depth, laterally or longitudinal location.

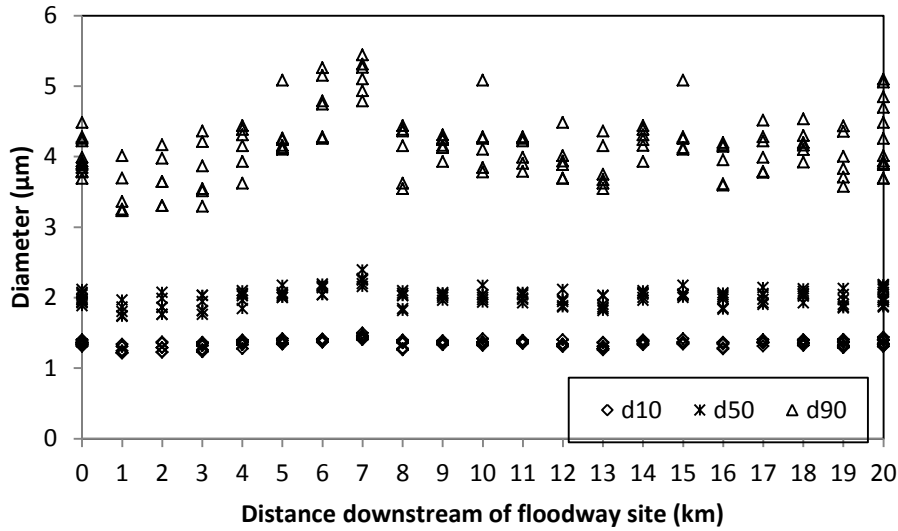


Figure 4.34: d_{10} , d_{50} , and d_{90} grain sizes for 20 km of water samples

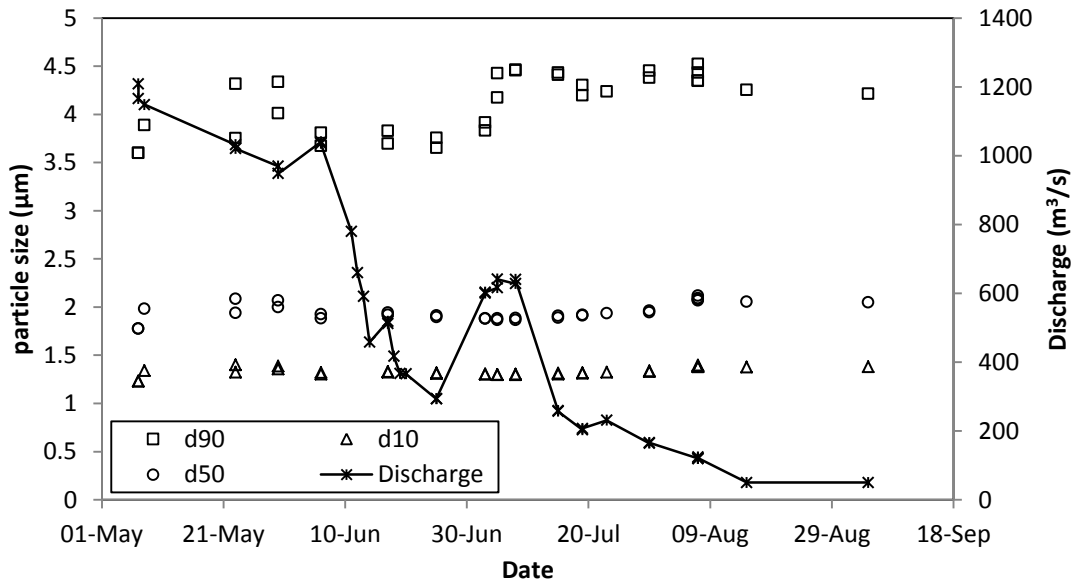


Figure 4.35: Relationship between GSD and discharge measurements

More than 100 freshly deposited sediment samples were acquired along the Red River banks. Most of the deposited sediment was collected at the boat launch at Maple Grove Park in different deposited sediment layers from top to bottom. It was found that there

was no significant variation in the grain size distribution of the sediment with depth. Also, testing freshly deposited materials from the banks showed an agreement between the deposited grain size and suspended sediment distribution. Figure 4.36 illustrates deposited and suspended solid grain size distributions using the Masterseizer 2000.

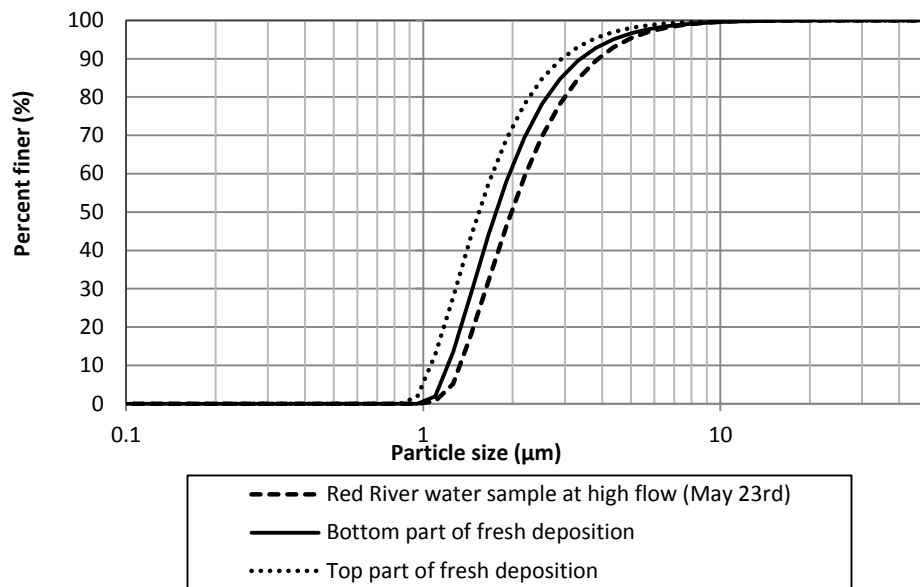


Figure 4.36: Comparing GSD of water sample and freshly deposited sediments

One reason for doing water-sediment grain size distribution tests was to determine the dominant mode of sediment transport. The magnitude of shear velocity influences sediment grain size and the mode of the transport for that particular grain. In other words, the type of sediment movement for each particle requires specific flow properties and each particle has its own preference to stay on the river bed or bank. The Rouse number ($R_o = \frac{w_s}{k*u_*}$) (w_s = particle settling velocity (m/s)) is a non-dimensional number in open channel flow which is used to define how sediment will be transported

in a river. Figure 4.37 shows how one particle will be transported in suspension under different Rouse numbers. Shah-Fairbank (2011) presented a classification to determine the dominant mode of sediment transport which is summarized in Table 4.19.

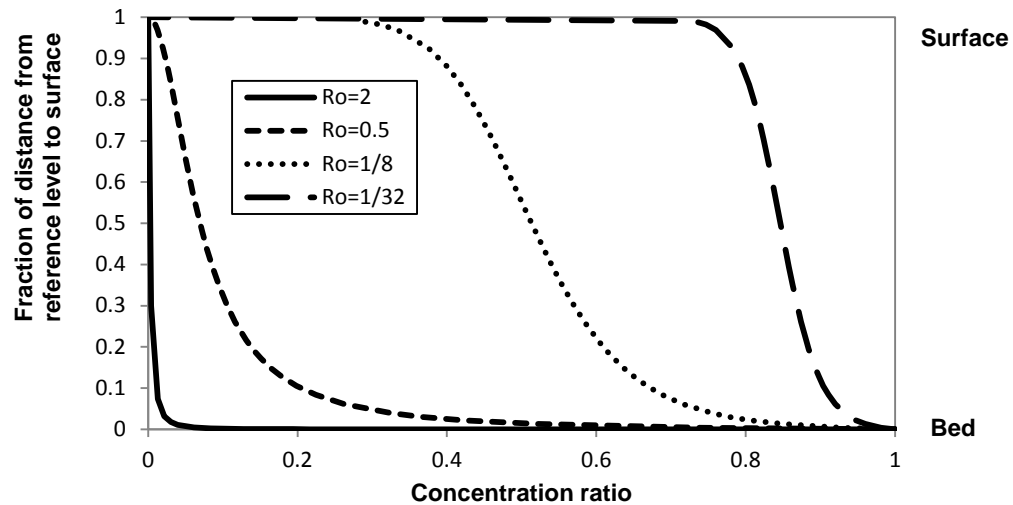


Figure 4.37: Specific particle size class concentration distribution on the basis of its Rouse number value

Table 4.19: Primary mode of sediment transport on the basis of Rouse number

$\frac{u_*}{w_s}$	R_o	Dominant mode of transport
<0.2	>12.5	No sediment transport
0.2-0.5	5-12.5	Bed load
0.5-2	1.25-5	Mixed load
2<	0.5-1.25	Suspended load

In order to determine the dominant mode of sediment transport on the Red using Table 4.19, the shear velocity on the basis of average shear stress was calculated under varying flow conditions. In addition, the maximum particle size potential in bed

transport and fully suspended transport corresponding to each shear velocity was computed (Table 4.20).

Although the river has the capacity to transport larger particle sizes (larger than clay and silt) as suspended sediment, the measured suspended sediment size distribution is much finer than the maximum particle size potential for each flow condition. Sand was never present in the suspended load, even at higher flows. Therefore the uniformity of particle size distribution in the clay range indicates that the majority of in-stream source of sediment is clay and the dominant mode of sediment transport is suspended sediment transport and not bed load. In other words, although electrochemical interactions between fine soils bond them together and increase the resistance to flow-induced erosion compared to non-cohesive soils, once the cohesive soil is eroded, it will be transported in suspension mode.

The studies of Blanchard et al. (2011) and Galloway et al. (2011) which were conducted 100 km upstream of the reach study also indicated that the dominant mode of sediment transport in the Red River was suspended mode. Blanchard et al. expressed that just 1% of total sediment load was bed load.

Table 4.20: Maximum particle size potential in bed and suspended transport mode

Discharge (m ³ /s)	Avg. shear on SPB (Pa)	Shear velocity (m/s)	Maximum size potential in bed (mm)	Maximum size potential in suspended (mm)
1200	3.65	0.06	5.36	0.13
997	3	0.05	5.13	0.12
780	2.2	0.05	3.75	0.11
660	2.1	0.05	3.75	0.11
518	1.6	0.04	2.86	0.1
458	1.4	0.04	2.59	0.1
417	1.3	0.04	2.34	0.1
367	1.1	0.03	2.1	0.1
294	0.9	0.03	1.67	0.09
164	0.5	0.02	0.98	0.07
50	0.3	0.02	0.7	0.06

4.13 River Geomorphic Change over Time

The role of flow-induced erosion, subaerial processes, and bank failure as well as the interaction between these processes has been documented as key controlling influences on bank widening (Rinaldi and Darby, 2008). While considerable effort has been directed toward understanding these mechanisms, the nature of the interaction between them has largely been ignored. In addition to this limitation, the paucity of measured field data particularly in cohesive rivers is another highlighted gap in the literature.

Bank monitoring is essential to assessing the erosion rates and locations susceptible to erosion and the periods during which these processes are likely to occur. Field validation is also required to assess modeling procedures and different erosion measurement tools. Bank erosion monitoring is important since it can give insight to the sedimentation flux along the river and provides practical information for the City and residents for improving bank protection program.

One method used to measure riverbank erosion is by determining changes in bathymetry over time. This method can measure bed erosion and also demonstrate the relative interaction between the bank erosion mechanisms. Data analysis results of resurveying which were conducted as part of this work can be used to verify the excess shear stress equation. One of the objectives of this study was to quantify and specify erosion and deposition locations along the reach, and highlight the areas where

elevation changes would be unrealistically high over time (bank failure). Another main objective of this research was to gain better knowledge on erosional and depositional processes over time under different hydraulic conditions. Four major high spatial resolution bathymetry surveys were taken in the study reach at different time intervals with different hydraulic conditions (July 2012; June 2013; September 2013; August 2014).

Erosion and deposition induced changes of river geometry were determined by comparing the change in bathymetry surveyed over three different years: 2012, 2013 and 2014. All survey data sets were converted to the same datum (NAD 83) and projection (UTM 14N). The initial elevation was considered for the 2012 data set, so that for the subsequent surveys on June or September 2013, and 2014 the new elevations could be extracted and the difference would indicate the erosion (or deposition) that occurred with reference to successive bathymetry. MATLAB and MIKE 21 were used to measure the depth of material removed or deposited, and their distribution along the Red. For each pairing of successive surveys, erosion is indicated by a negative value and deposition is presented by a positive one.

Data analysis for the first time period (July 2012 to June 2013) after a high flow ($Q = 1200 \text{ m}^3/\text{s}$ in May 2013) indicates that 90% of points were eroded between the 2012 and 2013 data set. The observed erosion for the bank and the bed ranged from -5 to -13 cm ($\mu = -10 \text{ cm}$; $\sigma = -2.5 \text{ cm}$) and -8 to -20 cm ($\mu = -14 \text{ cm}$; $\sigma = -4 \text{ cm}$) during the first time

period. Erosion is likely the result of increasing energy in the river system between two years.

The June 2013 to September 2013 time period shows a relatively moderate and low flow ($50 \text{ m}^3/\text{s} < Q < 700 \text{ m}^3/\text{s}$) and the bathymetry data analysis indicated that the elevations of points in the river in September were higher than in June except for the bank elevations (221-224 m). The results suggest that sediment deposition occurred on the bed with reference to June 2013. In other words, in this period, 60% of points had deposition and only 40% had erosion which was mostly on the banks. The average erosion for the banks and average deposition on the bed were -8 cm and 25 cm, respectively. Even though in this time period the applied shear stresses within the Red River were lower than the critical shear stresses at each test site (Table 4.16), the Red River experienced bank erosion.

The results during this period (June 2013 to September 2013) were compared to the first time period (2012 to June 2013) and suggested that if suspended sediment is available, as the discharge became lower, the flow gradually loses the capacity to transport sediment and therefore deposition occurs. The suspended sediment flux at the SPB and FGB in this period (Figure 4.30) indicates that the Red River was either in dynamic equilibrium or in a depositional phase, which agrees with the bed bathymetry analysis. However, bank erosion can likely be explained by the role of subaerial processes as an effective assistance to flow-induced erosion.

A small portion of the study reach was measured on July 19th, 2012, as well as August 3rd, 2012. Since 2012 was a year where the WSE was relatively steady (Figure 4.1), the flow condition between these two months and days was assumed similar and low. The bathymetry analyses showed that the same pattern and deposition were observed on the bed ($\mu = 3$ cm). Although the applied shear stresses in the banks were lower than applied shear stress in the bed as well as the soil critical shear stresses, in that small reach, the bank experienced erosion phenomena ($\mu = -6.5$ cm).

Therefore, this part of the study found that just considering the concept of the excess shear stress equation cannot adequately describe the pattern, rates, and locations of cohesive bank erosion. In fact, climate-related processes independently affect soils and are the controlling factor for the erosion of cohesive soils and sediment on the Red River's banks. In addition, it impacts soil structures in a way that even low flows may be able to erode and transport bank materials.

Results have indicated that between 2013 and 2014, an average of 2 cm and 30 cm of erosion occurred in the bed and bank, respectively. In other words, the cumulative erosion on the bank is about 15 times more than the bed. The range of shear stresses using MIKE 21 results at the maximum discharge is presented in Figure 4.38. This figure shows that even though the applied shear stress at the upper river elevations is less than the lower, the cumulative erosion depths in these areas are greater than at lower elevations. Therefore it can be concluded that subaerial processes and especially freeze-

thaw cycling were more responsible than flow for Red River bank erosion (Kimiaghalam et al., 2015a).

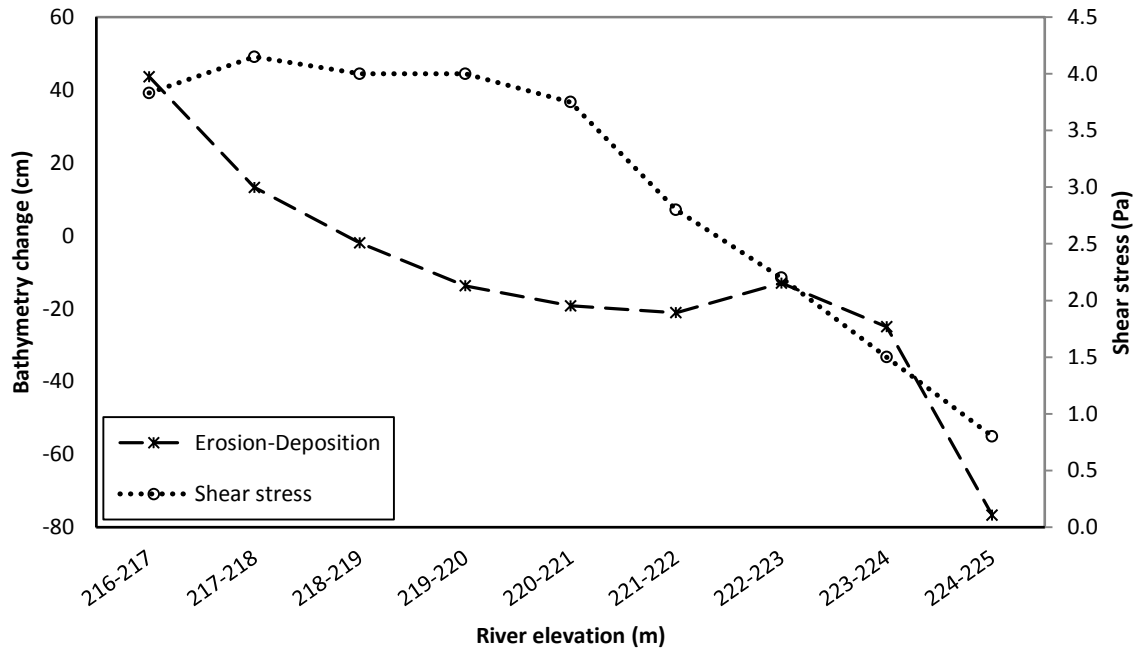


Figure 4.38: Measured cumulative erosion and deposition rate between 2013 and 2014 as well as maximum simulated applied shear stress ($Q= 1200 \text{ m}^3/\text{s}$) for different elevations of the Red

5.1 Conclusions

The excess shear stress equation indicates that the effect of applied shear stress on the Red River bank erosion is not significant. Due to the low bank applied shear stress values produced in the Red, differences between the soil critical shear stress and applied shear stress is not meaningful most of the time. But monitoring shows different bank behaviour. Repeated surveying showed that the erosion rate increases upward along the bank, even though the applied shear stress decreases.

Suspended sediment monitoring showed that during some of the monitoring period, the river reach was in dynamic equilibrium, and for the rest, experienced deposition and no erosion. This activity began when the discharge of the Red River was less than 1000 m³/s. One reason for the differences between surveying and suspended flux analysis would be that all bank erosion occurred while discharge was higher than 1000 m³/s.

Repeated surveying at low flow indicated that the bed increases in elevation due to the deposition of available suspended sediment, while the bank erodes. Therefore the hypothesis that significant bank erosion occurs only at high flow is rejected.

Field inspection showed that bank failure occurs locally along the riverbank. However, in low flow, the energy of the river water was not sufficient to carry these materials downstream. Therefore, increases in TSS were not detected along the reach. Most of the time, erosion does not occur due to the energy condition and velocity head of the Red River.

Another mechanism of bank widening during low flow was through subaerial processes, which impacted TSS. This occurs because the flow shear stress required to transport freeze/thaw soils is less than the applied shear stress needed to cause the erosion of non-frozen (original) cohesive soils. While the bed elevation increases during low flow, the banks experience fluvial erosion. The hydraulic shear stress is less than the critical shear stress of the original soil.

The duration of high flow was not sufficient enough to affect these materials or the higher value of critical shear stress just used to reduce resistance force between particles of these sediments or soils. Also, it is possible that during the high flow soil was still frozen, and the critical shear stress of frozen soil was higher than the applied shear stress. By the time high flow had ended and the soils had thawed, the critical shear stress dropped below the applied shear stress value and fluvial erosion occurred. Since bed deposition and bank erosion rates were similar in magnitude, the suspended sediment flux along the reach was not able to detect bank erosion.

From these conclusions, it follows that the typical approximation of predicting bank erosion does not apply in the Red River. By only considering fluvial erosion process, and assuming spatially and temporally constant critical shear stress, estimates of bank widening would not account for bank failure, subaerial process (freeze/thaw cycling). In fact this study found the excess shear stress equation cannot adequately describe the pattern of cohesive sediment erosion. Many improvements in understanding the processes of cohesive soil erosion have been made in the past decades. Nevertheless, due to the complex nature of these materials and their influences by many factors, this field still needs more research to be conducted. Complex behaviour, high uncertainty, and great variability in results have been found to influence the estimation of cohesive sediment erosion. Subaerial processes on the Red could be a major mechanism of bank widening (at the top of the bank) or be an agent of flow-induced erosion by increasing bank erodibility.

References

Abernathy, D., and I. D. Rutherford. 1998. Where along a river's length will vegetation most effectively stabilize stream banks. *Geomorphology*. 23: 55-75.

Ardiclioglu, M., S. Atabay, and M. Omran. 2007. Estimation of Discharge and Shear Stress Distribution in Natural Channels Based on Entropy Concept. 32nd IAHR Congress, Venice, Italy.

Ariathurai, R., and K. Arulanandan. 1978. Erosion rates of cohesive soils. *Journal of the Hydraulics Division of the ASCE*. 104: 279-283.

Arulanandan, K., E. Gillogley, and R. Tully. 1980. Development of a quantitative method to predict critical shear stress and rate of erosion of natural undisturbed cohesive soils. Technical Report GL-80-5. Vicksburg, MS: U.S. Army Corps of Engineers.

ASCE. 1998. River width adjustment. I: Processes and mechanisms. *Journal of Hydraulic Engineering*. 124 (9): 881-902.

ASTM. 2005. Standard test methods for liquid limit, plastic limit, and plasticity index of soils, No. D4318-05. West Conshohocken, PA: American Society for Testing and Materials.

ASTM. 2007c. Standard test method for particle-size analysis of soils, No. D422-63(2007). West Conshohocken, PA: American Society for Testing and Materials.

ASTM. 2007d. Standard test methods for determining sediment concentration in water samples, No. D3977-97(2007). West Conshohocken, PA: American Society for Testing and Materials.

ASTM. 2013. Standard test methods form moisture, ash, and organic matter of peat and other organic soils, No. D2974-13. West Conshohocken, PA: American Society for Testing and Materials.

Baptist, M. J., V. Babovic, J. R. Uthurburu, M. Keijzer, R. E. Uittenbogaard, A. Mynett, and A. Verwey. 2007. On Inducing Equations for Vegetation Resistance. *Journal of Hydraulic Research*. 45 (4): 435–450.

Blanchard, R. A., C.A. Ellison, J. M. Galloway, and D. A. Evans. 2011. Sediment concentrations, loads, and particle-Size distributions in the Red River of the North and

selected tributaries near Fargo, North Dakota, during the 2010 spring high-flow event. *U. S. Geological Survey Report 2011-5134*, 36 p.

Briaud, J. L., F. C. K. Ting, H. C. Chen, R. Gudavalli, S. Peregu, and G. Wei. 1999. SRICOS: Prediction of Scour Rate in Cohesive Soils at Bridge Piers. *Journal of Geotechnical and Geoenvironmental Engineering*. 125 (4): 237-246.

Briaud, J. L., F. C. K. Ting, H. C. Chen, Y. Cao, S. W. Han, and K. W. Kwak. 2001a. Erosion Function Apparatus for Scour Rate Predictions. *Journal of Geotechnical and Geoenvironmental Engineering*. 127 (2): 105-113.

Briaud, J. L., H. C. Chen, K. W. Kwak, S. W. Han, and F. C. K. Ting. 2001b. Multiflood and Multilayer Method for Scour Rate Prediction at Bridge Piers. *Journal of Geotechnical and Geoenvironmental Engineering*. 127 (2): 114-125.

Briaud, J. L., H. C. Chen, Y. Li, P. Nurtjahyo, and J. Wang. 2004. Pier and Contraction Scour in Cohesive Soils. NCHRP Report 516, Transportation Research Board, Washington, D.C.

Casagli, N., M. Rinaldi, A. Gargini, and A. Curini. 1999. Pore water pressure and streambank stability: Results from a monitoring site on the Sieve River, Italy. *Earth Surf. Processes Landforms*. 24:1095-1114

Chang, H.H. 1988. Fluvial processes in river engineering. New York: John Wiley and Sons, Ltd.

Chen, C.L. 1991. Unified Theory on Power Laws for Flow Resistance. *Journal of Hydraulic Engineering*. 117 (3): 371–389.

Chiu, C.L. 1991. Application of Entropy Concept in Open Channel Flow Study. *Journal of Hydraulic Engineering*. 117 (5): 615–627.

Chiu, C. L., and C. A. Said. 1995. Modeling of Maximum Velocity in Open-channel. *Journal of Hydraulic Engineering*. 121(1): 26-35.

Chow, V. T. 1959. Open-channel hydraulics. New York, NY, USA: McGraw-Hill.

Clark, E. H. 1985. The off-site costs of soil erosion. *Journal of Soil and Water Conservation*. 40 (1): 19-22.

Clark, L. A., and T. M. Wynn. 2007. Methods for determining streambank critical shear stress and soil erodibility: Implications for erosion rate predictions. *Transactions of the ASABE*. 50 (1): 95-106.

Couper, P. R. and I. P. Maddock. 2001. Subaerial river bank erosion processes and their

interaction with other bank erosion mechanisms on the River Arrow. *Earth Surface Processes and Landforms*. 26: 631-646.

Debnath, K., V. Nikora, J. Aberle, B. Westrich, and M. Muste. 2007. Erosion of cohesive sediments: Resuspension, bed load, and erosion patterns from field experiments. *Journal of Hydraulic Engineering*. 133 (5): 508-520.

DHI, 2012. MIKE 21 & 3 FLOW model FM sand transport module scientific documentation. DHI Group.

Dunn, I. 1959. Tractive resistance of cohesive channels. *Journal of the Soil Mechanics and Foundations Division, ASCE*. 85 (SM 3): 1-24.

Galloway, J.M., Blanchard, R.A. Blanchard, and C. A. Ellison. 2011, Sediment concentrations, loads, and particle-size distributions in the Red River of the North and selected tributaries near Fargo, North Dakota, during the 2011 spring high-flow event. *U.S. Geological Survey Scientific Investigations Report 2011–5134*, 30 p.

Green, T. R., S. G. Beavis, C. R. Dietrich, and A. J. Jakeman, 1999. Relating stream-bank erosion to in-stream transport of suspended sediment. *Hydrologic Processes*. 13: 777-787.

Grissinger, E. H. 1982. Bank erosion of cohesive materials. In *Gravel-bed Rivers: fluvial processes, engineering, and management*, ed. R. D. Hey, J. C. Bathurst, and C. R. Thorne. New York: John Wiley and Sons, Ltd.

Hanson, G. J. 1989. Channel erosion study of two compacted soils. *Transactions of the ASAE*. 32 (2): 485-490.

Hanson, G. J. 1990. Surface erodibility of earthen channels at high stresses. Part I – Open channel testing. *Transactions of the ASAE*. 33 (1): 127-131.

Hanson, G. J., and A. Simon. 2001. Erodibility of cohesive streambeds in the loess area of the mid-western USA. *Hydrological Processes*. 15: 23-38.

Heinzen, R. T. 1976. Erodibility Criteria for Soil. MS thesis. University of CA, Davis.

Huang, J., R. C. Hildale, and B. P. Greinmann. 2006. Chapter 4: Cohesive Sediment Transport. In: *Erosion and Sedimentation Manual*. United States Department of the Interior Bureau of Reclamation, Denver, CO.

HydroSurveyor S5/M9 System Manual. 2013. SonTek, a Division of YSI Inc. San Diego, CA, USA.

Julian, J. P., and R. Torres. 2006. Hydraulic erosion of cohesive riverbanks. *Geomorphology*. 76 (1-2): 193-206.

Keulegan, G.H. 1938. Laws of turbulent flow in open channels. *Journal of Research of the national Bureau of Standards J. Nat. Bur. Stand.* 21 (1): 707–741.

Khodashenas, S. R., K. E. K. Abderrezzak, and A. Paquier. 2008. Boundary shear stress in open channel flow: A comparison among six methods. *Journal of Hydraulic Research*. 46 (5): 598-609.

Kimiaghalam, N., S. Clark, and H. Ahmari. 2015a. An experimental study on the effects of physical, mechanical, and electrochemical properties of natural cohesive soils on critical shear stress and erosion rate. *International Journal of Sediment Research*. In press.

Kimiaghalam, N., M. Goharrokhi, and S. Clark, and H. Ahmari. 2015b. A comprehensive fluvial geomorphology study of riverbank erosion on the Red River in Winnipeg, Manitoba, Canada. *Journal of Hydrology*. In press.

Knapen, A., J. Poesen, G. Govers, G. Gyssels, and J. Nachtergaele. 2007. Resistance of soils to concentrated flow erosion: A review. *Earth-Science Reviews*. 80 (1-2): 75-109.

Knighton, D. 1998. *Fluvial Forms and Processes: A New Perspective*. New York: Oxford

University Press, Inc.

Lane, E. W. 1955. Design of stable channels. *Transaction of the ASCE*. 120 (2776): 1234 – 1279.

Lawler, D. M. 1993. Needle ice processes and sediment mobilization on river banks: The River Ilston. *Journal of Hydrology*. 150: 81-114.

Lawler, D. M. 1995. The impact of scale on the processes of channel-side sediment supply: a conceptual model. In *Effects of Scale on Interpretation and Management of Sediment and Water Quality*. IAHS Pub. 226. Wallingford, U.K.: International Association of Hydrological Sciences.

Lawler, D. M., C. R. Thorne, and J. M. Hooke. 1997. Chapter 6: Bank erosion and instability. In *Applied Fluvial Geomorphology for River Engineering and Management*, ed. C. R. Thorne, R. D. Hey and M. D. Newson. New York: John Wiley and Sons.

Lick, W., and J. McNeil. 2001. Effects of sediment bulk properties on erosion rates. *Science of the Total Environment* 266: 41-48.

Ludweig, H., and W. Tillman. 1950. Investigations of the Wall-shearing Stress in Turbulent Boundary Layers. Technical Memorandum 1285, National Advisory Committee for Aeronautics, May.

Malvern Instruments Ltd. 1999. Malvern Mastersizer 2000, Operators Guide. Worcestershire, England.

Moody, J. A., J. D. Smith, and B. W. Ragan. 2005. Critical shear stress for erosion of cohesive soils subjected to temperatures typical of wildfires. *Journal of Geophysical Research-Earth Surface*. 110 (F1): 13.

Montes, S. 1998. Hydraulics of Open Channel Flow. *ASCE*. 125: 127-142.

Moramarco, T., C. Saltalippi, and V. P. Singh. 2004. Estimation of Mean Velocity in Natural Channels Based on Chiu's Velocity Distribution Equation. *Journal of Hydrologic Engineering*. 9 (1): 42-50.

Munson, B. R., T. H. Okiishi, W. H. Wade, and A. P. Rothmayer. 2012. Fundamentals of Fluid Mechanics. New York: John Wiley and Sons, Ltd.

Osman, A. M., and C. R. Thorne. 1988. Riverbank stability analysis I: Theory. *Journal of Hydraulic Engineering*. 114: 134-150.

Owoputi, L. O., and W. J. Stolte. 1995. Soil detachment in the physically based soil erosion process: A review. *Transactions of the ASAE*. 38 (4): 1099-1110.

Partheniades, E. 1965. Erosion and deposition of cohesive soils. *Journal of the Hydraulics Division of the ASCE*. 91 (HY1): 105-139.

Prosser, I. P., A. O. Hughes, and I. D. Rutherford. 2000. Bank Erosion of an upland channel by subaerial processes. *Earth Surface Processes and Landforms*. 25 (10): 1085-1101.

Rinaldi, M., and S. E. Darby. 2008. Modelling river-bank-erosion processes and mass failure mechanisms: progress towards fully coupled simulations. In: Gravel-Bed Rivers 6 – From Process understanding to River Restoration. *Series Developments in Earth Surface Processes*. 11: 213-239.

RiverSurveyor S5/M9 System Manual Firmware Version 1.50. 2009. SonTek, a Division of YSI Inc. San Diego, CA, USA.

Roberts, J., R. Jepsen, D. Gotthard, and W. Lick. 1998. Effects of Particle Size and Bulk Density on Erosion of Quartz Particles. *Journal of Hydraulic Engineering, ASCE*. 124 (12): 1261-1267.

Shah-Fairbank, S.C., P. Y. Julien, and D. C. Baird. 2011. Total Sediment Load from SEMEP Using Depth-Integrated Concentration Measurements. *Journal of Hydraulic Engineering*, ASCE. 1606-1614.

Simon, A., A. Curini, S. E. Darby, and E. J. Langendoen. 2000. Bank and near-bank processes in an incised channel. *Geomorphology*. 35 (3-4): 193-217.

Smerdon, E. T. 1964. Effect of rainfall on critical tractive forces in channels with shallow flow. *Transactions of the ASAE*. 7: 287-290.

Smerdon, E. T., and R. P. Beasley. 1961. Critical tractive forces in cohesive soils. *Agricultural Engineering Research*. 42 (1): 26-29.

Soulsby, R.L. 1983. The bottom boundary layer of shelf seas. In: Johns, B. (Ed.), *Physical Oceanography of Coastal and Shelf Seas*. Elsevier Oceanography Series. 35: 189-262.

Sturm, T. W. 2001. *Open Channel Hydraulics*. 2nd edition. New York: McGraw-Hill Companies, Inc.

Thorne, C. R. 1982. Processes and mechanisms of river bank erosion. In *Gravel-bed Rivers*, ed. R. D. Hey, J. C. Bathurst and C. R. Thorne. New York: John Wiley and Sons, Ltd.

Thorne, C. R., 1990. Effects of vegetation on riverbank erosion and stability. In: Thornes, J. B., ed.: *Vegetation and Erosion: Processes and Environments*. Chichester: John Wiley and Sons, Ltd.

Trimble, S.W. 1997. Contribution of Stream Channel Erosion to Sediment Yield from an Urbanizing Watershed. *Science*, 278(5342): 1442-1444.

USEPA. 2002. National Water Quality Inventory. 2002. Washington, D.C.

Van Klaveren, R., and D. McCool. 1998. Erodibility and critical shear of a previously frozen soil. *Transactions of the ASAE*. 41 (5): 1315-1321.

Wallbrink, P. J., A. S. Murray, J. M. Olley, and L. J. Olive. 1998. Determining sources and transit times of suspended sediment in the Murrumbidgee River, New South Wales, Australia, using fallout ¹³⁷Cs and ²¹⁰Pb. *Water Resources Research*. 34: 879-887.

Walling, D. E., and C. M. Amos. 1999. Source, storage and mobilisation of fine sediment in a chalk stream system. *Hydrological Processes* 13: 323-340.

Weiss, A. 2012. The Use of Acoustic Doppler Current Profiler Technology to Quantify Total Suspended Solids under Ice. M.Sc. thesis. University of Manitoba, Canada.

Winnipeg Free Press Article: The River's Toll. 2005.

Wolman, M.G. 1959. Factors influencing erosion of a cohesive river bank. *American Journal of Science*, 257:204-216.

Wynn, T. M., M. B. Henderson, and D. H. Vaughan. 2008. Changes in streambank erodibility and critical shear stress due to subaerial processes along a headwater stream, southwestern Virginia, USA. *Geomorphology*. 97 (3-4): 260-273.

Wynn, T. M., and S. Mostaghimi. 2006. The effects of vegetation and soil type on streambank erosion, Southwestern Virginia, USA *Journal of the American Water Resources Association*. 42 (1): 69-82.